



저작자표시-비영리-동일조건변경허락 2.0 대한민국

이용자는 아래의 조건을 따르는 경우에 한하여 자유롭게

- 이 저작물을 복제, 배포, 전송, 전시, 공연 및 방송할 수 있습니다.
- 이차적 저작물을 작성할 수 있습니다.

다음과 같은 조건을 따라야 합니다:



저작자표시. 귀하는 원저작자를 표시하여야 합니다.



비영리. 귀하는 이 저작물을 영리 목적으로 이용할 수 없습니다.



동일조건변경허락. 귀하가 이 저작물을 개작, 변형 또는 가공했을 경우에는, 이 저작물과 동일한 이용허락조건하에서만 배포할 수 있습니다.

- 귀하는, 이 저작물의 재이용이나 배포의 경우, 이 저작물에 적용된 이용허락조건을 명확하게 나타내어야 합니다.
- 저작권자로부터 별도의 허가를 받으면 이러한 조건들은 적용되지 않습니다.

저작권법에 따른 이용자의 권리는 위의 내용에 의하여 영향을 받지 않습니다.

이것은 [이용허락규약\(Legal Code\)](#)을 이해하기 쉽게 요약한 것입니다.

[Disclaimer](#)

공학박사 학위논문

# **Multiparameter Estimation in Acoustic Full Waveform Inversion**

음향파 완전 파형 역산을 이용한  
다변수 추출 기법

2014년 2월

서울대학교 대학원

공과대학 에너지시스템공학부

정 우 돈

# Multiparameter Estimation in Acoustic Full Waveform Inversion

음향파 완전 파형 역산을 이용한 다변수 추출 기법

지도교수 민 동 주

이 논문을 공학박사 학위논문으로 제출함  
2013년 12월

서울대학교 대학원  
공과대학 에너지시스템공학부  
정 우 돈

정우돈의 박사 학위논문을 인준함  
2014년 1월

위 원 장 \_\_\_\_\_ (인)

부위원장 \_\_\_\_\_ (인)

위 원 \_\_\_\_\_ (인)

위 원 \_\_\_\_\_ (인)

위 원 \_\_\_\_\_ (인)

## **Abstract**

# **Multiparameter Estimation in Acoustic Full Waveform Inversion**

Woodon Jeong

Department of Energy Systems Engineering

The Graduate School

Seoul National University

With remarkable development in seismic data processing, the full waveform inversion (FWI) accomplishes an extraordinary feat that plays a key role in inferring material properties and direct approach for delineating subsurface structures. Recently, one of interesting topics in the FWI is estimation of the multiparameter such as velocity, density, anisotropic parameters and so on. Among the various parameters, I focus on reconstruction of the velocity and density by using the acoustic FWI, especially to achieve the enhancement of a result of the density inversion. It has already been known that velocity can be retrieved by the acoustic FWI while density is regarded as the parameter which is hard to recover in FWI technique. To overcome this limitation, I

propose a hierarchical inversion strategy, which consists of two stages. Each stage places emphasize on each parameter: velocity inversion at the first stage and density inversion at the second stage. Through the sensitivity analyses, which compare the mathematical formulae and radiation patterns for each parameterization, bulk modulus-density parameterization is chosen as an optimal parameterization for the first stage. For density inversion in the second stage, impedance-velocity parameterization is chosen, because it is more independent in a range of the scattered angle than the other parameterizations. In this case, density is obtained by using the relationship between the inverted impedance and velocity. To investigate the feasibility of the hierarchical FWI, several numerical examples of both synthetic and real field data sets are employed. Numerical examples give the reasonable results for velocity and density, and show the possibility of the proposed method in the multiparameter inversion.

**Keywords: Acoustic, Full waveform inversion, Frequency-domain, Hierarchical inversion, Multiparameter**

**Student Number: 2011-30996**

# Contents

Abstract .....	1
Contents.....	3
List of Figures.....	6
List of Tables .....	12
Chapter 1 Introduction .....	13
1.1 Motivation .....	13
1.2 Research objective .....	17
1.3 Outline.....	18
Chapter 2 Review of Forward and Inverse Problems .....	19
2.1 Acoustic wave propagation modeling.....	19
2.1.1 Acoustic wave equations with multiparameter.....	20
2.1.2 Modeling using finite element method .....	22
2.1.3 PML boundary condition .....	25
2.2 Inverse theory .....	29
2.2.1 Review of inverse theory .....	30
2.2.2 Verification of algorithm.....	33
2.2.3 Simultaneous-source method.....	39

2.2.4	Preconditioning and weighting.....	45
2.2.5	Source wavelet estimation.....	48
Chapter 3	Multiparameter inversion.....	50
3.1	Sensitivity analysis.....	50
3.1.1	Comparison of mathematical formulae.....	51
3.1.2	Comparison of radiation patterns.....	53
3.1.3	Comparison of conventional FWI results.....	70
3.2	Hierarchical approach .....	80
3.2.1	1 <sup>st</sup> stage: Velocity inversion.....	81
3.2.2	2 <sup>nd</sup> stage: Density inversion.....	87
Chapter 4	Numerical examples.....	93
4.1	Inversion set-up.....	93
4.2	Synthetic data examples .....	94
4.2.1	SEG/EAGE salt model.....	94
4.2.2	Marmousi-2 model.....	100
4.3	Real data example .....	112
4.3.1	Gulf of Mexico data set (ION/GXT) .....	112
Chapter 5	Conclusions .....	131

Bibliography .....	135
초록 .....	141

## List of Figures

**Figure 2.1.1** (a) Schematic diagram of model space and perfectly matched layers. (b) An Illustration of damping function  $\zeta_x$ . The damping function (i.e., damping coefficient) is zero in a range of model space, but gradually increases at the additional layers. .... 28

**Figure 2.2.1** Comparison of time traces for partial derivative wavefields with respect to (a) velocity and (b) density of velocity–density parameterization. The black solid line and dot indicate numerically (back-propagation) and analytically (finite-difference) computed partial derivative wavefields. .... 35

**Figure 2.2.2** Comparison of time traces for partial derivative wavefields with respect to (a) bulk modulus and (b) density of bulk modulus–density parameterization. The black solid line and dot indicate numerically (back-propagation) and analytically (finite-difference) computed partial derivative wavefields. .... 36

**Figure 2.2.3** Comparison of time traces for partial derivative wavefields with respect to (a) impedance and (b) density of impedance–density parameterization. The black solid line and dot indicate numerically (back-propagation) and analytically (finite-difference) computed partial derivative wavefields. .... 37

**Figure 2.2.4** Comparison of time traces for partial derivative wavefields with respect to (a) impedance and (b) velocity of impedance–velocity parameterization. The black solid line and dot indicate numerically (back-propagation) and analytically (finite-difference) computed partial derivative wavefields. .... 38

**Figure 2.2.5** The expectation of the coefficient for (a) standard gradient term and (b) crosstalk term on the right-hand side of equation (2.2.16). .... 43

**Figure 2.2.6** SNR curves of the simultaneous-source method (solid line) and predicted one (dashed line). .... 44

**Figure 3.1.1** Radiation pattern of the velocity in velocity–density parameterization

as a representative example. Seismic source is located on the surface at a distance of 0.5 km. Perturbed cell which is employed as a virtual source is located at the center of the model. .... 59

**Figure 3.1.2** Schematic diagram of a method of interpolation. The value on the same distance from the center of a circle where the virtual source is excited is interpolated as a function of angle  $\theta$  (upper figure). Source position is required to be interpolated to maintain the symmetry in element-based scheme (lower figure). The grey rectangular indicates the cell which is used for virtual source by perturbation. .... 60

**Figure 3.1.3** Radiation pattern interpolated as a function of the angle for (a) velocity–density, (b) bulk modulus–density, (c) impedance–density and (d) impedance–velocity parameterizations. .... 61

**Figure 3.1.4** Schematic diagram of the relationship between maximum offset and penetrating depth for velocity inversion in impedance–velocity parameterization. A and B shows the radiation pattern of the parameters located at depths of  $h_1$  and  $h_2$ . ... 63

**Figure 3.1.5** Schematic diagram of the behavior of the radiation pattern of velocity in impedance–velocity parameterization. The grey part is the limitation of the coverage of the velocity information from the reflection, which is approximated very roughly. Considering a number of sources in FWI, (b) shows the expected coverage of the velocity information in this parameterization. .... 64

**Figure 3.1.6** The (a) true and (b) initial velocity models used in numerical tests. Because density is assumed to be homogeneous as 2 g/cc, impedance has the same tendency with the velocity. .... 65

**Figure 3.1.7** The gradient direction at the first iteration for impedance: The maximum offset is the number of (a) 4<sup>th</sup> layer, (b) 3<sup>rd</sup> layer, (c) 2<sup>nd</sup> layer and (d) 1<sup>st</sup> layers, respectively. .... 66

**Figure 3.1.8** The gradient direction at the first iteration for velocity: The maximum offset is the number of (a) 4<sup>th</sup> layer, (b) 3<sup>rd</sup> layer, (c) 2<sup>nd</sup> layer and (d) 1<sup>st</sup> layers, respectively. .... 68

**Figure 3.1.9** A modified version of the AA’ line of the SEG/EAGE salt model: (a) velocity and (b) density. .... 73

<b>Figure 3.1.10</b> Initial models used for FWI: (a) velocity and (b) density.....	74
<b>Figure 3.1.11</b> Reconstructed velocity model inverted by using (a) velocity–density, (b) bulk modulus–density, (c) impedance–density and (d) impedance–velocity parameterizations, respectively.....	75
<b>Figure 3.1.12</b> Reconstructed density model inverted by using (a) velocity–density, (b) bulk modulus–density, (c) impedance–density and (d) impedance–velocity parameterizations, respectively.....	77
<b>Figure 3.2.1</b> Reconstructed velocity model inverted by using velocity–density parameterization with a pseudo-density which is (a) 1.5, (b) 2 and (c) 2.5 g cm <sup>-3</sup> , respectively. ....	84
<b>Figure 3.2.2</b> Reconstructed velocity model inverted by using bulk modulus–density parameterization with a pseudo-density which is (a) 1.5, (b) 2 and (c) 2.5 g cm <sup>-3</sup> , respectively. ....	85
<b>Figure 3.2.3</b> Reconstructed velocity model inverted by using impedance–density parameterization with a pseudo-density which is (a) 1.5, (b) 2 and (c) 2.5 g cm <sup>-3</sup> , respectively. ....	86
<b>Figure 3.2.4</b> Reconstructed density model inverted by using (a) velocity–density and (b) impedance–velocity parameterizations with true velocity, respectively. ....	90
<b>Figure 3.2.5</b> Model misfit error between the inverted and true density model. The black solid and dashed lines denote the model misfit error of velocity–density and impedance–velocity parameterizations, respectively. ....	91
<b>Figure 3.2.6</b> Model misfit error between the inverted and true density model for (a) background area and (b) main salt body. The black solid and dashed lines denote the model misfit error of velocity–density and impedance–velocity parameterizations, respectively. ....	92
<b>Figure 4.2.1</b> Reconstructed velocity model for SEG/EAGE salt model inverted at the 1 <sup>st</sup> stage of the hierarchical inversion by using bulk modulus–density parameterization with pseudo-bulk modulus and fixed density as 2 g cm <sup>-3</sup> . ....	96
<b>Figure 4.2.2</b> (a) The true and (b) inverted pseudo bulk modulus for SEG/EAGE salt model. For an accurate comparison, the maximum and minimum values of the	

legend are fixed at the same level.....	97
<b>Figure 4.2.3</b> Reconstructed models for (a) velocity and (b) density of SEG/EAGE salt model in the 2 <sup>nd</sup> stage.....	98
<b>Figure 4.2.4</b> Reconstructed models for (a) velocity and (b) density of SEG/EAGE salt model obtained by using the recently-announced hierarchical method (Prioux <i>et al.</i> 2013).....	99
<b>Figure 4.2.5</b> True models for (a) velocity and (b) density of elastic Marmousi-2 model.....	102
<b>Figure 4.2.6</b> Initial models for (a) velocity and (b) density of elastic Marmousi-2 model.....	103
<b>Figure 4.2.7</b> Conventional FWI results for Initial models for velocity and density of elastic Marmousi-2 model obtained by using (a,b) velocity–density, (c, d) bulk modulus–density, (e, f) impedance–density and (g, h) impedance–velocity parameterizations, respectively. For each couple of figures, velocity is a figure expressed by unit of km s <sup>-1</sup> (upper) and density is g cm <sup>-3</sup> (lower). .....	104
<b>Figure 4.2.8</b> Reconstructed velocity model for elastic Marmousi-2 model inverted at the 1 <sup>st</sup> stage of the hierarchical inversion by using bulk modulus–density parameterization with pseudo-bulk modulus and fixed density as 2 g cm <sup>-3</sup> . .....	108
<b>Figure 4.2.9</b> (a) The true and (b) inverted pseudo bulk modulus for elastic Marmousi-2 model. For an accurate comparison, the maximum and minimum values of the legend are fixed at the same level. ....	109
<b>Figure 4.2.10</b> Reconstructed models for (a) velocity and (b) density of elastic Marmousi-2 model in the 2 <sup>nd</sup> stage.....	110
<b>Figure 4.2.11</b> Reconstructed models for (a) velocity and (b) density of elastic Marmousi-2 model obtained by using the recently-announced hierarchical method (Prioux <i>et al.</i> 2013). .....	111
<b>Figure 4.3.1</b> A representative shot gather at a distance of 10.45 km from the left side of the model and its frequency spectrum. ....	118
<b>Figure 4.3.2</b> Initial models for (a) <i>P</i> -wave velocity and (b) density of Gulf of Mexico data set. ....	119

**Figure 4.3.3** Reconstructed model for *P*-wave velocity at the first stage of the hierarchical FWI for Gulf of Mexico data set. The pseudo-density is fixed at a constant as  $2 \text{ g cm}^{-3}$  except for the water layer. .... 120

**Figure 4.3.4** Reconstructed models for (a) *P*-wave velocity and (b) density at the second stage of the hierarchical FWI for Gulf of Mexico data set. RMS errors for the 1<sup>st</sup> and 2<sup>nd</sup> stage are plotted in (c). .... 121

**Figure 4.3.5** Examples of the (a) original shot gather and (b) modeled shot gather obtained by using the inverted velocity and density at the second stage. Time traces extracted at an offset of (c) 0.5 km and (d) 1.18 km. The dashed grey line indicates the time trace extracted from the original shot gather. The light grey dashed line and black solid line represent the time traces extracted from the modeled shot gather obtained by using the inverted velocity and pseudo-density at the first stage and the inverted velocity and density at the second stage, respectively. .... 122

**Figure 4.3.6** (a) The number of folds for each CMP. Maximum fold is 102. (b) RMS velocity model computed by the velocity model obtained in the second stage of the hierarchical FWI. SU command VELCONV is used for the conversion. .... 124

**Figure 4.3.7** Representative CMP gathers for the CMP number (a) from 10221 to 10241 and (b) from 12001 to 12021. And its NMO corrected CMP gathers are shown in (c) and (d). .... 126

**Figure 4.3.8** (a) Stacked section of the CMP gathers for the original data set. The Black arrow indicates the dominant reflection chosen for the comparison. The three panels at the right-hand side are the comparison of the dominant reflection for the original data set (top), stacked sections using the modeled data obtained in the first stage (center) and the second stage (bottom) in the relative value. The black dotted lines indicate the location where the time traces are extracted. (b) Amplitudes for each stacked section in (a). The grey solid line represents the profile of the original data set, and black solid and dashed lines denote that of the first and the second stages, respectively. .... 127

**Figure 4.3.9** RTM images obtained by the back-propagation of the virtual source of (a) velocity and (b) density in velocity–density parameterization, respectively, and

(c) velocity and (d) impedance in impedance–velocity parameterization, respectively. ....128

**Figure 4.3.10** ADCIGs for (a) velocity and (b) density at a distance of 3, 5, 7 and 9 km from the left side of the model. The angle is ranging from 0 ° to 45 ° in each panel. ....130

## List of Tables

<b>Table 3.1.1</b> Summary of the conventional FWI results. ....	80
<b>Table 3.2.1</b> Known and unknown parameters when the velocity is given in the first stage of the hierarchical inversion. $v$ , $K$ , $I$ and $\rho$ denote the velocity, bulk modulus, impedance and density, respectively. ....	90

# Chapter 1. Introduction

## 1.1 Motivation

Since the full waveform inversion (FWI) has started to receive attention in the society of geophysicists, the technology has advanced rapidly for a few decades. Because the FWI can be operated automatically and without any human interferences, seismic FWI has been regarded as a promising method that can delineate and inferring information of the subsurface structures and properties of the subsurface materials.

In the vortex of overflowing studies, many of them endeavor to improve accuracy and computational efficiency of the FWI in a broad sense. By using frequency-marching methods (Bunks *et al.* 1995; Sirgue and Pratt 2004; Kim *et al.* 2011), scaling/weighting method (Pratt *et al.* 1998; Shin *et al.* 2001; Plessix and Mulder 2004; Oh and Min 2013) and building good initial models (Shin and Cha 2008, 2009), FWI can reduce non-linearity and probability of becoming caught on local minima. Hereby, FWI has been able to qualify as a reliable tool for seismic data processing and to attract public attention, and we become to anticipate more stable and accurate FWI results. In addition, because FWI usually suffers from heavy computational time and cost, many studies focus on enhancement of the computational efficiency. Among them, as a big issue, simultaneous-source methods have been widely used and discussed. Beginning from pre-stack depth migration, simultaneous-source method has been applied to waveform inversion and achieved a remarkable

computational speed-up (Krebs *et al.* 2009; Ben-Hadj-Ali *et al.* 2011, Jeong *et al.* 2013).

As an up-to-the-minute issue, recent researches are concentrating on the multiparameter of the subsurface media:  $P$ - and  $S$ -wave velocity, density, anisotropic parameters and attenuation (Q-factor). In the early stages of the FWI, the most of classical studies only considered compressional wave speed with the acoustic wave equation (Lailly 1983; Tarantola 1984; Kolb *et al.* 1986; Gauthier *et al.* 1986; Pratt *et al.* 1998). With the development of equipments and techniques, obtaining multicomponent data has become common in recent year so that the FWI based on the elastic wave equation come to the fore, which strives for the reconstruction of multiparameter (Mora 1987; Choi *et al.* 2008a; Brossier *et al.* 2009; Jeong *et al.* 2012). Furthermore, as the importance of anisotropy has been taken into account in seismic data processing, there are numerous studies of FWI considering anisotropy, particularly a transverse isotropic material with a vertical axis of symmetry (VTI) (Lee *et al.* 2010; Plessix and Cao 2011; Jeong *et al.* 2011; Gholami *et al.* 2013a, 2013b). Among those parameters, density has been regarded as a parameter of the greatest difficulty to reconstruct through FWI. Recognizing the significant role of density in amplitude-versus-offset (AVO) and amplitude-versus-angle (AVA) analyses, many studies have made efforts to recover the velocity and density simultaneously using FWI. Although the information of density can be extracted in field exploration such a well logging, there is a spatial limitation in the interpretation unless extremely dense logging is performed. To compensate this limitation, Mora (1987) and

Choi *et al.* (2008a, 2008b) attempted to invert the velocity and density in elastic and fluid-solid coupled FWI. Additionally, Köhn *et al.* (2012) and Jeong *et al.* (2012) suggested a parameterization study for the elastic FWI and a hierarchical FWI strategy, respectively.

However, considering the data that have more huge and dense volume such as 3D problems and real field data, proposed methods (elastic and fluid-solid coupled FWIs) may not be practical tools under the current computing systems. Thus, the acoustic FWI has usually been used in a practical point of view in spite of a latent limitation that real earth media are approximated as acoustic media, which only provide the  $P$ -wave propagation. Considering the acoustic wave equation, although several studies take variable density into account in the acoustic FWI, they only consider the velocity in FWI which is accomplished retrieving the density using empirical formula or assumption of homogeneous density for whole model (Pica *et al.* 1990; Przebindowska *et al.* 2012; Mulder and Plessix 2008). Recently, Prieux *et al.* (2013) have suggested a hierarchical inversion that is based on a parameterization of  $P$ -wave velocity and density. They have shown quite good results for the synthetic and real field data examples. However, in their examples, assumed model as a true model of density has a consistent tendency with velocity structure. That is, where the velocity has a high value, the density shows a high value likewise. Thus, considering cases of complex or salt-dominant structures, the parameterization of  $P$ -wave velocity and density may not be a suitable parameterization for every case. Additionally, in a preceding study, which is co-written by Virieux and Operto (2009) as a very meaningful footprint of

FWI, they have mentioned a parameterization of  $P$ -wave velocity and  $P$ -wave impedance for a suitable parameterization of multiparameter imaging. In contrast, Jeong and Min (2012) have presented a research about the hierarchical inversion for density estimation using parameterizations of bulk modulus and density for the first stage and  $P$ -wave velocity and density for the second stage. Like this, there are numerous and various researches with the object of multiparameter inversion based on the acoustic FWI, but their results are still insufficient to use and not satisfactory for real data application.

## 1.2 Research objective

In this thesis, I propose a hierarchical FWI method for multiparameter estimation, particularly density estimation. To do so, I discuss the various parameterizations for acoustic FWI to examine which parameterization is suitable for each stage:  $P$ -wave velocity and density, bulk modulus and density,  $P$ -wave impedance and density,  $P$ -wave velocity and  $P$ -wave impedance. With the purpose of suggestion for hierarchical inversion method, we need to compare characteristics of each parameterization through qualitative and quantitative analyses. Additionally, differences are discussed between the conventional hierarchical inversion and the new one, which occur when we apply both method not only to the model that shows similar geological feature for velocity and density but also to the complex or salt-dominant structures that show a reversal tendencies for the velocity and density. Thus, the final objective of this thesis becomes designing hierarchical inversion through suitable parameterizations for multiparameter estimation.

### **1.3 Outline**

In the following chapters, basic theories about frequency-domain wave propagation modeling and waveform inversion are explained. I only consider isotropic and non-viscous acoustic media for modeling and inversion. Next, mathematical formulae and radiation patterns of each parameterization are depicted and compared. Through these comparisons, I make a decision of optimal parameterization for the hierarchical inversion and show successive estimation of the multiparameter such as velocity and density. Proposed method is demonstrated to the synthetic models and real field data sets. For verifying properties of it, FWI results obtained in a modified version of the SEG/EAGE salt model are shown. To examine generality of the method, Marmousi-2 model is used that is regarded as relatively easy to invert the parameters. After the application to the synthetic data sets, the real field data gathered in the Gulf of Mexico is employed to evaluate the proposed algorithm.

## Chapter 2. Review of Forward and Inverse Problems

### 2.1 Acoustic wave propagation modeling

Generally, seismic data processing such as seismic waveform inversion and seismic migration has been performed based on acoustic wave equation even though there are intrinsic characteristics in which the acoustic wave equation approximates the real earth media to acoustic media. Likewise, this dissertation only focuses on the acoustic FWI for multiparameter estimation. To perform FWI, first of all, acoustic wave propagation should be simulated accurately as a forward problem. In the following chapters, basic theories about frequency-domain wave propagation modeling and waveform inversion are explored. I only consider isotropic and non-viscous acoustic media for modeling and inversion. In general, many of studies have assumed homogeneous density as  $1 \text{ g cm}^{-3}$  so that the density term is not considered in wave propagation modeling and waveform inversion. Recently, however, the use of variable density becomes to be common which helps FWI researchers pay attention to the multiparameter reconstruction. Being based on the needs of density estimation, classifying several parameterizations with the various parameter and numerical analyses by using the finite-element method of wave equations for each parameterization will be described over three chapters.

### 2.1.1 Acoustic wave equations with multiparameter

In the frequency domain, the acoustic wave equation can be written as

$$\left[ -\frac{\omega^2}{\rho(\mathbf{r})v(\mathbf{r})^2} - \nabla \cdot \left( \frac{1}{\rho(\mathbf{r})} \nabla \right) \right] \tilde{p}(\mathbf{r}, \omega) = \tilde{f}(\mathbf{r}_s, \omega), \quad (2.1.1)$$

where  $\mathbf{r}$  is the position vector, and  $\omega$  is the angular frequency. The subscript  $s$  indicates a position of the source. Variables  $\rho$ ,  $v$ ,  $p$  and  $f$  are the density,  $P$ -wave velocity, pressure and source function, respectively. Tilde denotes Fourier transform of the variable so that

$$\tilde{p}(\mathbf{r}, \omega) = \int_{-\infty}^{\infty} p(\mathbf{r}, t) e^{-i\omega t} dt \quad \text{and} \quad \tilde{f}(\mathbf{r}, \omega) = \int_{-\infty}^{\infty} f(\mathbf{r}, t) e^{-i\omega t} dt. \quad (2.1.2)$$

The acoustic wave equation can be parameterized not only by the velocity–density but also the bulk modulus–density and impedance–density. Although there might be the other parameterizations, in this thesis, I only focus on the parameterizations that take the density into account explicitly. Acoustic wave equations, which are parameterized by the bulk modulus–density and impedance–density, can be expressed by

$$\left[ -\frac{\omega^2}{K(\mathbf{r})} - \nabla \cdot \left( \frac{1}{\rho(\mathbf{r})} \nabla \right) \right] \tilde{p}(\mathbf{r}, \omega) = \tilde{f}(\mathbf{r}_s, \omega) \quad (2.1.3)$$

and

$$\left[ -\frac{\rho(\mathbf{r})\omega^2}{I(\mathbf{r})} - \nabla \cdot \left( \frac{1}{\rho(\mathbf{r})} \nabla \right) \right] \tilde{p}(\mathbf{r}, \omega) = \tilde{f}(\mathbf{r}_s, \omega), \quad (2.1.4)$$

respectively.  $K$  indicates the bulk modulus and  $I$  denotes the  $P$ -wave impedance. To avoid confusion in meaning, and for convenience, each

parameterization will be classified by omission of word ‘ $P$ ’ as velocity–density (equation 2.1.1), bulk modulus–density (equation 2.1.3) and impedance–density (equation 2.1.4).

Furthermore, there is a parameterization that is assigned as a judicious parameterization (Virieux and Operto 2009) for multiparameter FWI, which is not mentioned in previous paragraph: impedance–velocity. Aforementioned parameterizations invert the density directly; in contrast, the density is extracted by a relationship between impedance and velocity in this parameterization. Acoustic wave equation parameterized by impedance–velocity is formulated as

$$\left[ -\frac{\omega^2}{I(\mathbf{r})v(\mathbf{r})} - \nabla \cdot \left( \frac{v(\mathbf{r})}{I(\mathbf{r})} \nabla \right) \right] \tilde{p}(\mathbf{r}, \omega) = \tilde{f}(\mathbf{r}_s, \omega). \quad (2.1.5)$$

## 2.1.2 Modeling using finite element method

To solve the acoustic wave equation as a forward problem, the finite-element method is employed. Among four parameterizations, velocity–density is used for a representative example to expand numerical formulae. Assuming two dimensions and omitting the notation of the vector for only one element domain, equation (2.1.1) can be rewritten as

$$-\frac{\omega^2}{\rho v^2} \tilde{p} = \frac{\partial}{\partial x} \left( \frac{1}{\rho} \frac{\partial \tilde{p}}{\partial x} \right) + \frac{\partial}{\partial z} \left( \frac{1}{\rho} \frac{\partial \tilde{p}}{\partial z} \right) + \tilde{f}. \quad (2.1.6)$$

Then the weighted residual approach is applied to equation (2.1.6) as

$$r = -\frac{\omega^2}{\rho v^2} \tilde{p} - \frac{\partial}{\partial x} \left( \frac{1}{\rho} \frac{\partial \tilde{p}}{\partial x} \right) - \frac{\partial}{\partial z} \left( \frac{1}{\rho} \frac{\partial \tilde{p}}{\partial z} \right) - \tilde{f}, \quad (2.1.7)$$

where  $r$  indicates the residual. Because the weighted average of equation (2.1.7) goes to zero in the domain  $\Omega$ , by multiplying equation (2.1.7) by an arbitrary weighting function  $W_j$ , equation (2.1.7) can be expressed as follows:

$$\iint_{\Omega} W_j \left\{ -\frac{\omega^2}{\rho v^2} \tilde{p} - \frac{\partial}{\partial x} \left( \frac{1}{\rho} \frac{\partial \tilde{p}}{\partial x} \right) - \frac{\partial}{\partial z} \left( \frac{1}{\rho} \frac{\partial \tilde{p}}{\partial z} \right) - \tilde{f} \right\} d\Omega = 0, \quad (2.1.8)$$

where  $j$  indicates the  $j$ th node of an element. By the integration by parts, equation (2.1.8) becomes

$$\iint_{\Omega} \left\{ W_j \left( -\frac{\omega^2}{\rho v^2} \tilde{p} - \tilde{f} \right) - \frac{\partial W_j}{\partial x} \left( \frac{1}{\rho} \frac{\partial \tilde{p}}{\partial x} \right) - \frac{\partial W_j}{\partial z} \left( \frac{1}{\rho} \frac{\partial \tilde{p}}{\partial z} \right) \right\} d\Omega = 0, \quad (2.1.9)$$

which contains lower order of derivative than the original form, so called weak formulation. To solve equation (2.1.9), the integrals can be approximated to the summation of functions. The bilinear functions as a shape

function are applied to the approximation of the solution for equation (2.1.9)

as

$$\tilde{p} \approx \sum_{k=1}^N \tilde{p}_k \phi_k, \quad (2.1.10)$$

where  $\tilde{p}_k$  means the pressure at the  $k$ th nodal point of an element. By Galerkin's method, being let  $W_j = \phi_j$  and substituting equation (2.1.10) into equation (2.1.9) gives a linear algebraic system:

$$\sum_{k=1}^N \tilde{p}_k \iint_{\Omega} \left( -\phi_j \frac{\omega^2}{\rho v^2} \phi_k - \tilde{f} \phi_j + \frac{\partial \phi_j}{\partial x} \frac{1}{\rho} \frac{\partial \phi_k}{\partial x} + \frac{\partial \phi_j}{\partial z} \frac{1}{\rho} \frac{\partial \phi_k}{\partial z} \right) d\Omega = 0, \quad (2.1.11)$$

for  $j = 1, 2, \dots, N$ . Equation (2.1.11) can be rewritten by using a form of mass and stiffness matrices by

$$\sum_{k=1}^N (S_{jk} - \omega^2 M_{jk}) \tilde{p}_k = \tilde{f}_j, \quad (2.1.12)$$

which are

$$M_{jk} = \iint_{\Omega} \frac{1}{\rho v^2} \phi_j \phi_k d\Omega, \quad (2.1.13)$$

$$S_{jk} = \iint_{\Omega} \frac{1}{\rho} \left( \frac{\partial \phi_j}{\partial x} \frac{\partial \phi_k}{\partial x} + \frac{\partial \phi_j}{\partial z} \frac{\partial \phi_k}{\partial z} \right) d\Omega \quad (2.1.14)$$

and

$$f_j = \iint_{\Omega} \tilde{f} \phi_j d\Omega, \quad j = 1, 2, \dots, N, \quad (2.1.15)$$

respectively. Assembling the linear algebraic system for each element into the global system, equation (2.1.12) can be written in matrix-vector form (Marfurt 1984):

$$\mathbf{L}\tilde{\mathbf{p}} = \tilde{\mathbf{f}} \quad (2.1.16)$$

or

$$(\mathbf{S} - \omega^2 \mathbf{M})\tilde{\mathbf{p}} = \tilde{\mathbf{f}}, \quad (2.1.17)$$

where  $\mathbf{L}$  is a modeling operator matrix, and  $\mathbf{S}$  and  $\mathbf{M}$  indicate the stiffness and mass matrices, respectively. Hence, when the finite-element method is applied to equations (2.1.1), (2.1.3), (2.1.4) and (2.1.5), the modeling operator matrices for each parameterization can be written as

$$\mathbf{L}_e^{\text{V-D}} = -\frac{\omega^2}{\rho v^2} \mathbf{M}_e + \frac{1}{\rho} \mathbf{S}_e, \quad (2.1.18)$$

$$\mathbf{L}_e^{\text{B-D}} = -\frac{\omega^2}{K} \mathbf{M}_e + \frac{1}{\rho} \mathbf{S}_e, \quad (2.1.19)$$

$$\mathbf{L}_e^{\text{I-D}} = -\frac{\rho \omega^2}{I^2} \mathbf{M}_e + \frac{1}{\rho} \mathbf{S}_e \quad (2.1.20)$$

and

$$\mathbf{L}_e^{\text{I-V}} = -\frac{\omega^2}{Iv} \mathbf{M}_e + \frac{v}{I} \mathbf{S}_e, \quad (2.1.21)$$

where the superscripts indicate each parameterization and the subscript  $e$  denotes the matrices for an element. Although the matrix  $\mathbf{L}$  is comprised of different parameters for each parameterization, their numerical values for all four parameterization are the same so that the modeling results are the same as well.

### 2.1.3 PML boundary condition

When the wave propagation is simulated by using the finite-difference method or the finite-element method, there must be artifacts arise from the artificial boundary, which can severely disturb the numerical analyses of a seismic data such as seismic migration and FWI. To suppress the reflected waves generated by artificial boundary, various kinds of boundary conditions are suggested and applied (Reynolds 1979, Clayton and Engquist 1977, Higdon 1986, Berenger 1994, Cohen 2002). Among them, the boundary condition by using perfectly matched layer (PML) suggested by Cohen (2002) is applied in this study. The basic concept of the PML boundary condition is adding the absorbing layers that can attenuate the reflected waves within their propagation in the additional layers as shown in Figure 2.1.1(a). In order to take PML boundary condition into account to the wave equation, first of all, a damping function can be defined as

$$\zeta_x = \begin{cases} 0 & x \in \text{model space} \\ \frac{3c_0}{2x_{pml}} \log(R) \left( \frac{x'}{x_{pml}} \right)^2 & x \in \text{PML} \end{cases} \quad (2.1.22)$$

and

$$\zeta_z = \begin{cases} 0 & z \in \text{model space} \\ \frac{3c_0}{2z_{pml}} \log(R) \left( \frac{z'}{z_{pml}} \right)^2 & z \in \text{PML} \end{cases}, \quad (2.1.23)$$

where the subscript *pml* denotes the thickness of additional layers (PML), *prime* means a distance from the edge of model space and  $c_0$  is the velocity of

PML. For  $R$ , 1000 is generally used. In Figure 2.1.1(b), it is observed the damping function is zero in the model space whereas it gradually increases in a range of PML. To apply the PML damping function to the wave equation, coordinate system should be redefined by using a damping function as

$$\hat{x} = \begin{cases} x & x \in \text{model space} \\ x + \frac{i}{\omega} \int_0^x \zeta_x(p) dp & x \in \text{PML} \end{cases} \quad (2.1.24)$$

and

$$\hat{z} = \begin{cases} z & z \in \text{model space} \\ z + \frac{i}{\omega} \int_0^z \zeta_z(p) dp & z \in \text{PML} \end{cases}, \quad (2.1.25)$$

where  $i = \sqrt{-1}$ , and  $\omega$  is the angular frequency. Thus, because the damping function is non-zero only at a range of PML, following equations are given:

$$d\hat{x} = \begin{cases} dx & x \in \text{model space} \\ dx + \frac{i}{\omega} \zeta_x dx & x \in \text{PML} \end{cases} \quad (2.1.26)$$

and

$$d\hat{z} = \begin{cases} dz & z \in \text{model space} \\ dz + \frac{i}{\omega} \zeta_z dz & z \in \text{PML} \end{cases}. \quad (2.1.27)$$

From equations (2.1.26) and (2.1.27), with the allowance that the damping function is zero in model space, a relationship between original coordinate and new coordinate systems is obtained by

$$\frac{\partial}{\partial \hat{x}} = \frac{1}{1 + i\zeta_x / \omega} \frac{\partial}{\partial x} = \frac{1}{A_1} \frac{\partial}{\partial x} \quad \text{for all } x \quad (2.1.28)$$

and

$$\frac{\partial}{\partial \hat{z}} = \frac{1}{1 + i\zeta_z / \omega} \frac{\partial}{\partial z} = \frac{1}{A_2} \frac{\partial}{\partial z} \quad \text{for all } z. \quad (2.1.29)$$

Hence, substituting equations (2.1.28) and (2.1.29) to the wave equation gives converted form of mass and stiffness matrices that are slightly distinct from equations (2.1.13) and (2.1.14) as

$$M_{jk} = \iint_{\Omega} \frac{1}{\rho v^2} A_1 A_2 \phi_j \phi_k d\Omega \quad (2.1.30)$$

and

$$S_{jk} = \iint_{\Omega} \frac{1}{\rho} \left( \frac{A_2}{A_1} \frac{\partial \phi_j}{\partial x} \frac{\partial \phi_k}{\partial x} + \frac{A_1}{A_2} \frac{\partial \phi_j}{\partial z} \frac{\partial \phi_k}{\partial z} \right) d\Omega, \quad (2.1.31)$$

respectively. By applying PML boundary condition to the wave equation, a new modeling operator is obtained, it helps eliminate the artifacts generated from the artificial boundary.

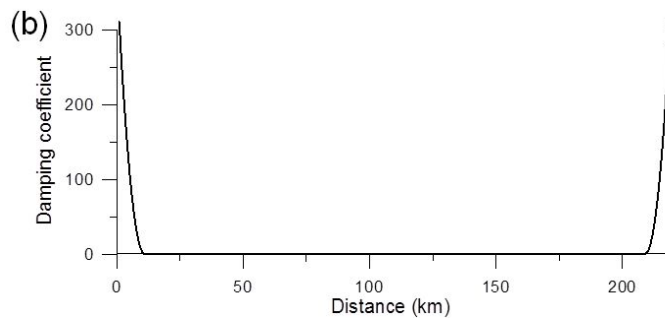
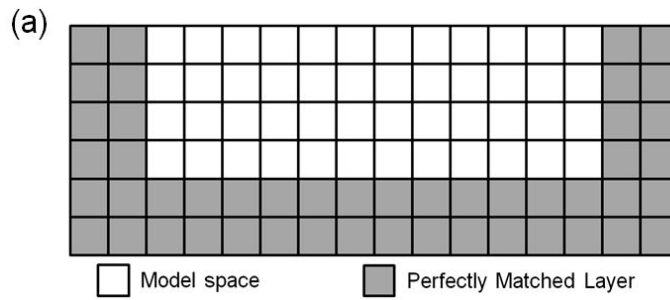


**Figure 2.1.1** (a) Schematic diagram of model space and perfectly matched layers. (b) An Illustration of damping function  $\zeta_x$ . The damping function (i.e., damping coefficient) is zero in a range of model space, but gradually increases at the additional layers.

## 2.2 Inverse theory

As a topic of this chapter, inverse theory is reviewed that is the ultimate theme of this study, which will be simulated based on the modeling algorithm described in previous section. Description of the FWI in detail starts with a minimization of the objective function. Although there are several objective functions I can use such as  $l_1$ -,  $l_2$ -,  $l_1/l_2$  hybrid- and logarithmic- norms, and others, I only use  $l_2$ -norm minimization in this study. By using  $l_2$ -norm for examining the residuals between modeled data and observed data, taking partial derivative with respect to the model parameter gives the gradient direction that is used for updating model parameters iteratively. Although there have already been many optimization methods, to avoid heavy computational costs and time, the gradient-based method is employed for computational efficiency. For efficient calculation of the gradient direction, the back-propagation algorithm is introduced. To verify the inversion algorithm, I compare the partial derivative wavefield computed by using the back-propagation algorithm with those computed by using the finite-difference method. In addition, simultaneous-source method that achieves remarkable speed-up in FWI is applied to the FWI algorithm.

### 2.2.1 Review of inverse theory

The objective function, based on the  $l_2$ -norm, that examines residuals between the modeled data and observed data for a single shot gather at a mono-frequency, can be written as

$$C(\mathbf{m}) = \frac{1}{2}(\mathbf{u} - \mathbf{d})^T \overline{(\mathbf{u} - \mathbf{d})}, \quad (2.2.1)$$

where  $\mathbf{m}$ ,  $\mathbf{u}$  and  $\mathbf{d}$  indicate the vectors comprised of the model parameter, modeled wavefield and observed wavefield, respectively. Superscript  $T$  means the transpose and the over-bar indicates the complex conjugate. To minimize the objective function, the steepest descent direction of the objective function is calculated by taking partial derivative of equation (2.2.1) with respect to the  $k$ th model parameter  $m_k$  as follows:

$$\frac{\partial C(\mathbf{m})}{\partial m_k} = \text{Re} \left[ \left( \frac{\partial \mathbf{u}}{\partial m_k} \right)^T \overline{(\mathbf{u} - \mathbf{d})} \right] \quad (2.2.2)$$

Equation (2.2.2) means the steepest ascent direction and it will be used in FWI with an opposite direction as

$$m_k^{n+1} = m_k^n - \alpha \frac{\partial C(\mathbf{m})}{\partial m_k}, \quad (2.2.3)$$

where  $n$  is the number of iterative processes, and  $\alpha$  denotes a step length.

Computation of the partial derivative of modeled wavefield with respect to the model parameter in equation (2.2.2) can become more efficient and easier when the adjoint state of the modeling operator is considered (Lailly 1983; Tarantola 1984; Pratt *et al.* 1998; Plessix 2006; Shin and Min 2006). Remember that the matrix-vector form of the wave equation. Taking partial

derivative of that equation with respect to  $m_k$  gives

$$\frac{\partial \mathbf{L}}{\partial m_k} \mathbf{u} + \mathbf{L} \frac{\partial \mathbf{u}}{\partial m_k} = 0, \quad (2.2.4)$$

where  $\mathbf{u}$  means pressure (i.e.,  $\mathbf{p}$  in equation 2.1.16). Thus, equation (2.2.4) can be written by

$$\frac{\partial \mathbf{u}}{\partial m_k} = \mathbf{L}^{-1} \left( -\frac{\partial \mathbf{L}}{\partial m_k} \mathbf{u} \right). \quad (2.2.5)$$

Consequently, substituting equation (2.2.5) into equation (2.2.2), the gradient direction can be rewritten as

$$\frac{\partial C(\mathbf{m})}{\partial m_k} = \text{Re} \left[ \left( \mathbf{f}_k^* \right)^T \left( \mathbf{L}^{-1} \right)^T \bar{\mathbf{r}} \right], \quad (2.2.6)$$

where

$$\mathbf{f}_k^* = -\frac{\partial \mathbf{L}}{\partial m_k} \mathbf{u} \quad (2.2.7)$$

is virtual (secondary) source.  $\mathbf{r}$  is the residual vector for whole model that pads zeros on every nodal points excluding the receiver-located positions.

Hence, considering the gradient direction for whole model parameters gives

$$\nabla C = \text{Re} \left[ \left( \mathbf{F}^* \right)^T \left( \mathbf{L}^{-1} \right)^T \bar{\mathbf{r}} \right], \quad (2.2.8)$$

where

$$\mathbf{F}^* = \left[ \mathbf{f}_1^* \quad \mathbf{f}_2^* \quad \cdots \quad \mathbf{f}_{np}^* \right]. \quad (2.2.9)$$

is the virtual source matrix obtained by expanding the virtual source vector for each parameter to the virtual source matrix for whole model.  $np$  means total number of parameters.

Additionally, the gradient direction in equation (2.2.8) has usually had

very large value on the top of the model where the source is excited and very small value with becoming deeper because of geometrical spreading. Thus, such a gradient direction should be scaled to update the model parameter properly. The approximate and full Hessian matrices, which are used for preconditioning the gradient direction in a manner of Gauss-Newton and full Newton method, can play an important role to the gradient direction. However, the computations of these matrices are extremely expensive so that the diagonal component of pseudo-Hessian matrix is employed in this thesis to avoid computational overburden (Shin *et al.* 2001):

$$\nabla C = \frac{\text{Re} \left[ (\mathbf{F}^*)^T (\mathbf{L}^{-1})^T \bar{\mathbf{r}} \right]}{\text{Re} \left[ \text{diag} \left\{ (\mathbf{F}^*)^T \overline{(\mathbf{F}^*)} + \lambda \mathbf{I} \right\} \right]}, \quad (2.2.10)$$

where  $\lambda$  and  $\mathbf{I}$  denote the damping constant and identity matrix in the Marquart-Levenberg regularization, respectively.

## 2.2.2 Verification of algorithm

In the previous section, the efficient calculation of the partial derivative wavefield by using the back-propagation is described. Partial derivative wavefield represents a variation, which is generated when the value of model parameters (i.e., variables) have been changed. Considering that the gradient direction is computed by the product of the partial derivative wavefield and residual wavefield, it is noted how important computation of the gradient direction is to FWI. Hence, before applying this excellent method to FWI, it is required to verify the validity of the back-propagation algorithm. Equation (2.2.5), which indicates the gradient direction, is accomplished by solving the forward problem that considers the virtual source (i.e., equation 2.2.7) as a source function. The gradient direction such a partial derivative term can be expressed by the finite-difference form as

$$\frac{\partial \mathbf{u}}{\partial m_k} \approx \lim_{\Delta m_k \rightarrow 0} \frac{\mathbf{u}(m_k + \Delta m_k) - \mathbf{u}(m_k)}{\Delta m_k}. \quad (2.2.11)$$

Hence, comparing equations (2.2.5) and (2.2.11), the back-propagation algorithm is able to be verified. For convenience, equations (2.2.5) and (2.2.11) are called numerical and analytic solutions, respectively. For a comparison, I assume a homogeneous model that has the velocity of 2 km s<sup>-1</sup> and density of 2.07 g cm<sup>-3</sup>. Receivers are located at a distance of 600 m from the source position, and perturbed cell that is going to be changed for a small value of  $\Delta m_k$ . In this study, because I focus on the four kind of parameterization, partial derivative wavefields are compared for each parameter in each parameterization. Figures 2.2.1 to 2.2.4 show traces of the

partial derivative wavefields computed numerically (i.e., back-propagation) and analytically (i.e., finite-difference). To generate those signals, frequency-domain modeling algorithm is used and their results are transformed to time-domain by using inverse Fourier transform. In Figures 2.2.3 and 2.2.4, some deviations are observed because of trade-offs between parameters. For impedance–density and impedance–velocity parameterizations, if one parameter has been changed, the counterpart parameter becomes to be affected. This affects the computation of the partial derivative wavefield by using the finite-difference method. Nevertheless, four kinds of parameterization show reasonable results for each parameter so that we can confirm the accuracy and validity of the back-propagation algorithm.

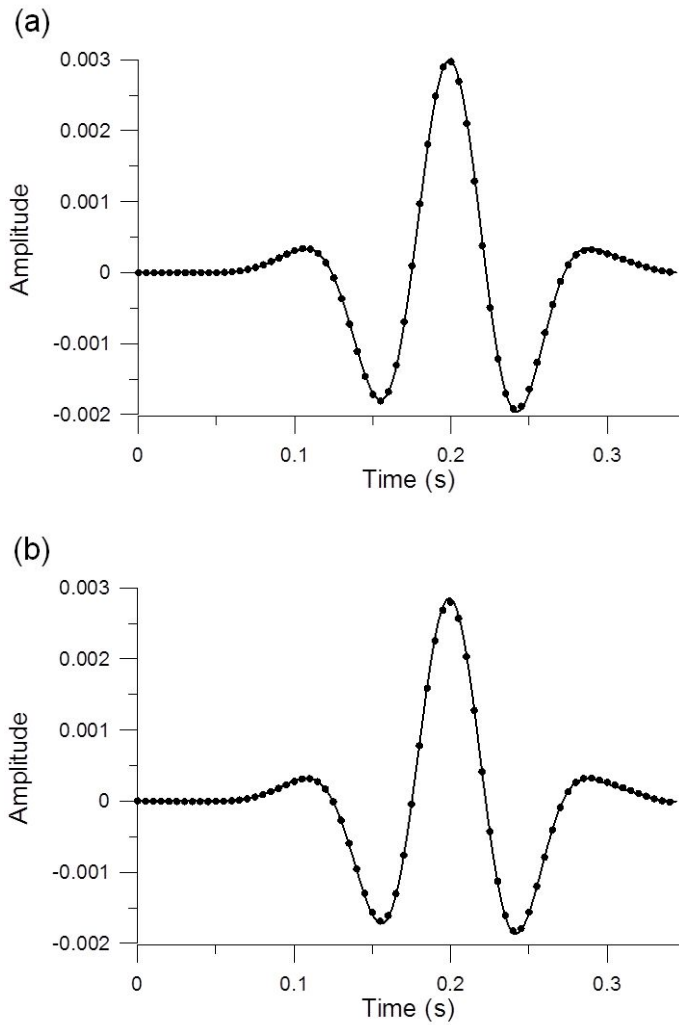


**Figure 2.2.1** Comparison of time traces for partial derivative wavefields with respect to (a) velocity and (b) density of velocity–density parameterization. The black solid line and dot indicate numerically (back-propagation) and analytically (finite-difference) computed partial derivative wavefields.

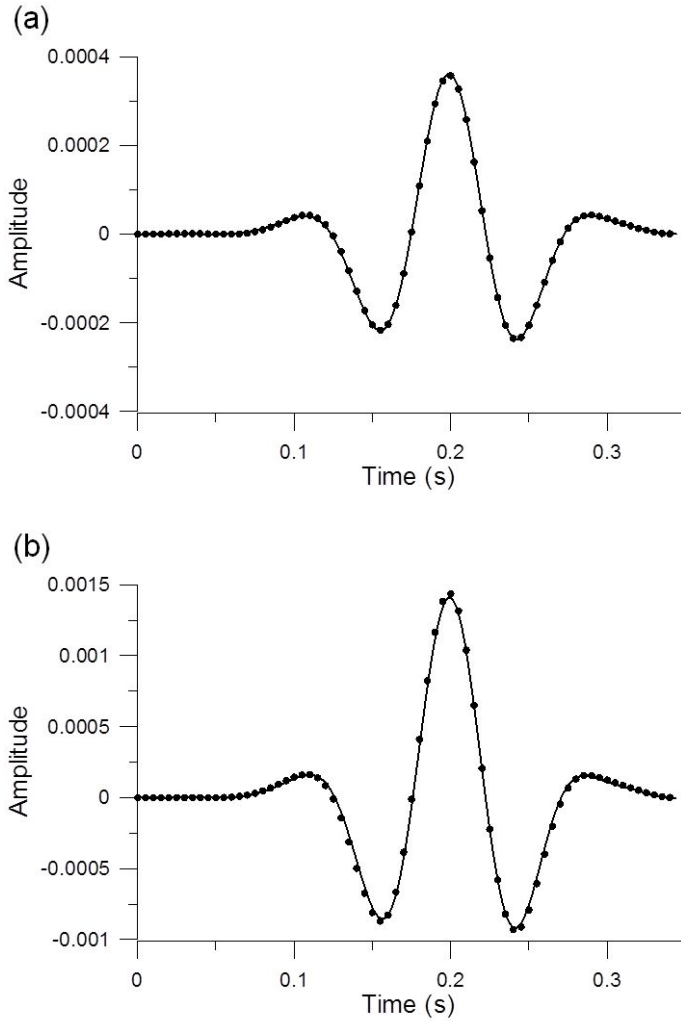


**Figure 2.2.2** Comparison of time traces for partial derivative wavefields with respect to (a) bulk modulus and (b) density of bulk modulus–density parameterization. The black solid line and dot indicate numerically (back-propagation) and analytically (finite-difference) computed partial derivative wavefields.

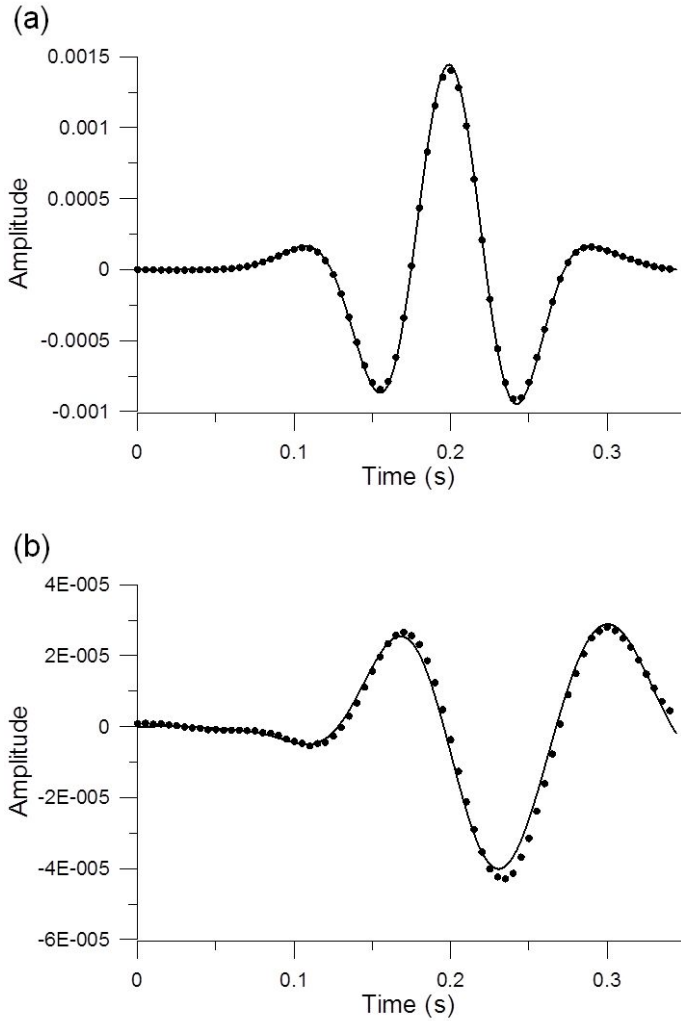


**Figure 2.2.3** Comparison of time traces for partial derivative wavefields with respect to (a) impedance and (b) density of impedance–density parameterization. The black solid line and dot indicate numerically (back-propagation) and analytically (finite-difference) computed partial derivative wavefields.

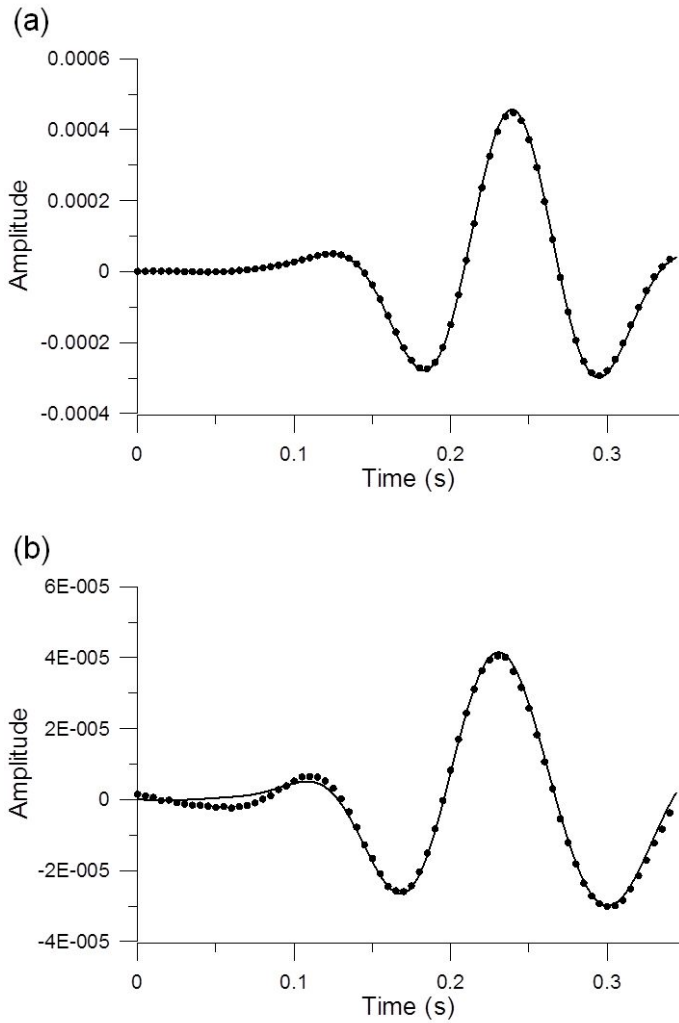


**Figure 2.2.4** Comparison of time traces for partial derivative wavefields with respect to (a) impedance and (b) velocity of impedance–velocity parameterization. The black solid line and dot indicate numerically (back-propagation) and analytically (finite-difference) computed partial derivative wavefields.

### 2.2.3 Simultaneous-source method

As the technology of seismic data acquisition and processing, the volume of the data has increased and corresponding computational burden has increased along. Hence, there have been numerous attempts to enhance the computational efficiency of FWI. Among them, the simultaneous-source method (Krebs *et al.* 2009; Ben-Hadj-Ali *et al.* 2011; Schuster *et al.* 2011; Jeong *et al.* 2013) has been received attention for years because of its great improvement in computational efficiency. When all sources are excited at the same time, there must be the crosstalk noise arises from the adjacent sources so that the crosstalk reduction has to be guaranteed to use the simultaneous-source method for FWI. If the crosstalk reduction is assured, FWI incorporating with simultaneous-source method gives remarkable computational speed-up.

The conventional  $l_2$ -norm objective function for a single frequency and for all sources and receivers, which incorporates with individual source method, is written by

$$C_{individual} = \sum_{i=1}^{ns} \sum_{j=1}^{nr} \frac{1}{2} (u_{ij} - d_{ij}) \overline{(u_{ij} - d_{ij})}, \quad (2.2.12)$$

where  $i$  and  $j$  indicate the indices of the source and receiver, respectively.

Taking partial derivative with respect to the parameter  $m$  gives

$$\frac{\partial C_{individual}}{\partial m} = \text{Re} \left[ \sum_{i=1}^{ns} \sum_{j=1}^{nr} \frac{\partial u_{ij}}{\partial m} \overline{(u_{ij} - d_{ij})} \right]. \quad (2.2.13)$$

In contrast, when we apply the simultaneous-source method to the FWI, the

objective function is expressed by

$$C_{simsrc} = \sum_{j=1}^{nr} \frac{1}{2} \left( \sum_{i=1}^{ns} e_i u_{ij} - \sum_{i=1}^{ns} e_i d_{ij} \right) \overline{\left( \sum_{i=1}^{ns} e_i u_{ij} - \sum_{i=1}^{ns} e_i d_{ij} \right)}, \quad (2.2.14)$$

and the gradient direction can be written as

$$\frac{\partial C_{simsrc}}{\partial m} = \text{Re} \left[ \sum_{j=1}^{nr} \left\{ \sum_{i=1}^{ns} \left( e_i e_i \frac{\partial u_{ij}}{\partial m} r_{ij} \right) + \sum_{i=1}^{ns} \sum_{\substack{k=1 \\ k \neq i}}^{ns} \left( e_i e_k \frac{\partial u_{ij}}{\partial m} r_{kj} \right) \right\} \right], \quad (2.2.15)$$

where

$$e_j e_k = \begin{cases} 1, & \text{for } j = k \\ \exp\{l(\theta_j - \theta_k)\}, & \text{for } j \neq k \end{cases}, \quad (2.2.16)$$

which is a product of a phase encoding function  $e$  and its complex conjugate. In the phase encoding function,  $l = \sqrt{-1}$  and  $\theta$  is a random sequence varying from 0 to  $2\pi$ . In equation (2.2.15), the former term is regarded as a standard gradient term, which is the same as the gradient direction of the individual source FWI. The latter term, the second term is considered as a crosstalk, which arises from the adjacent sources. Because of a property in equation (2.2.16), crosstalk noise can be suppressed, and the simultaneous-source FWI gives comparable results with the conventional individual-source FWI along with remarkable computational speed-up.

To verify that the simultaneous-source FWI can converge to the individual-source FWI, two things have to be ensured: suppression of the second term on right-hand side for equation (2.2.15) as a crosstalk term; whether the signal-to-noise ratio (SNR) curve follows the predicted one suggested by Schuster *et al.* (2011) or not. Above all, the expectation of

equation (2.2.15) is calculated to verify crosstalk reduction in the simultaneous-source FWI algorithm. Expectation of the gradient direction can be written by

$$E\left(\frac{\partial C_{simsrc}}{\partial m}\right) = \text{Re} \left[ \sum_{j=1}^{nr} \left\{ \sum_{i=1}^{ns} E(e_i \bar{e}_i) \left( \frac{\partial u_{ij}}{\partial m} r_{ij} \right) + \sum_{i=1}^{ns} \sum_{\substack{k=1 \\ k \neq i}}^{ns} E(e_i \bar{e}_k) \left( \frac{\partial u_{ij}}{\partial m} r_{kj} \right) \right\} \right], \quad (2.2.17)$$

where  $E(\bullet)$  is the expectation. To examine the expectations in equation (2.2.17), it is computed by using a Monte Carlo simulation. Figure 2.2.5 shows the expectation of coefficients for the first and second terms on the right-hand side of equation (2.2.17). As shown in Figure 2.2.5, because the expectation of the crosstalk noise approaches zero and that of the standard gradient term equals one, equation (2.2.17) can be approximated to equation (2.2.13). Hence, the computation of  $np \times nr \times ns$ , where  $np$ ,  $nr$  and  $ns$  indicate the number of parameter, receivers and sources, can be reduced for  $np \times nr$  by using one super-shot. This property makes the simultaneous-source FWI achieve remarkable computational speed-up. Furthermore, to ensure the suppression of the crosstalk as iteration goes on, SNR is estimated. In here, ‘signal’ and ‘noise’ mean the strength of standard gradient term and crosstalk noise term, respectively. This process is accomplished by stacking the gradient images obtained by the simultaneous-source method as Schuster *et al.* (2011) did for the iterative stacking migration. If the crosstalk noise could be attenuated as iteration proceeds, stacked gradient image would converge on the gradient direction obtained by the individual-source method. Following this procedure, SNR curve is compared to the predicted curve, which is

proportional to a square root of the number of iterations. SNR of the gradient direction is calculated by

$$\text{SNR} = \frac{\|ni \times \nabla C^{ref}\|}{\left\| \sum_{iter=1}^{ni} (\nabla C_{iter} - \nabla C^{ref}) \right\|} \quad (2.2.18)$$

with

$$\nabla C^{ref} = \frac{1}{k} \lim_{k \rightarrow \infty} \sum_{iter=1}^{ni} \nabla C_{iter} \quad (2.2.19)$$

where  $ni$  denotes a total number of the iterations. In this case, 5000 times of the iteration is used for  $k$ . Figure 2.2.6 shows SNR curves. The curve calculated by equation (2.2.18) follows well the predicted one, although there are slight discrepancies.

In summary, these results support that the simultaneous-source method can achieve great speed-up in computation and successively suppress the crosstalk noise by random phase encoding and iterative procedure.

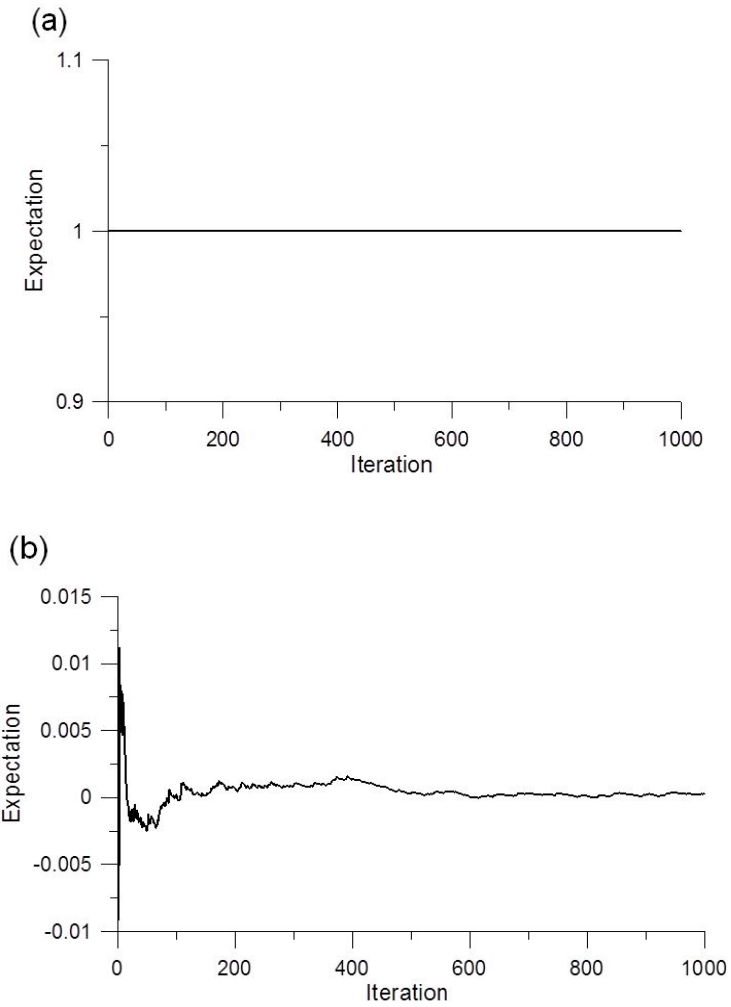


**Figure 2.2.5** The expectation of the coefficient for (a) standard gradient term and (b) crosstalk term on the right-hand side of equation (2.2.16).

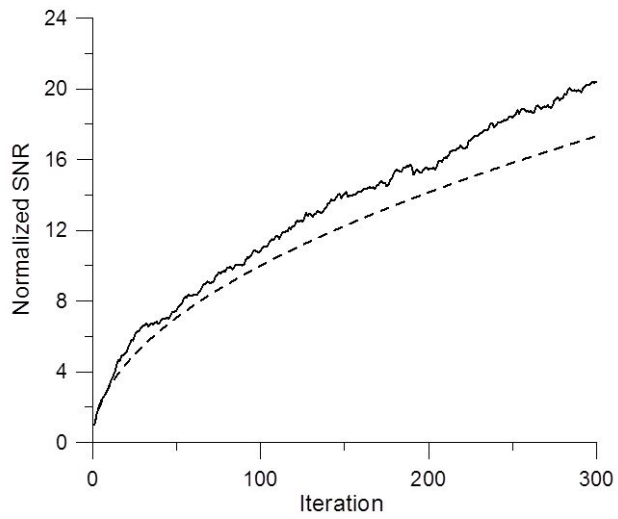


**Figure 2.2.6** SNR curves of the simultaneous-source method (solid line) and predicted one (dashed line).

## 2.2.4 Preconditioning and weighting

As widely known, FWI is a nonlinear and ill-posed problem. Frequently, it is trapped in local minima and involves cyclic skipping without proper initial guesses or low-frequency component data. There are many attempts to reduce and avoid these shortcomings such as multiscale approaches in the time or frequency domain, time windowing and Laplace-domain approaches (Bunks *et al.* 1995; Sirgue and Pratt 2004; Brenders *et al.* 2009; Shin and Cha 2008, 2009). In other way, dissimilar with mentioned methods that rule overall FWI process, preconditioning the gradient direction with locally operating term such as smoothing or local dip estimation can reduce ill-posedness of the FWI problems. In this study, I only use the latter methods for regularization of the gradient direction.

According to Guitton *et al.* (2012), the preconditioning of the gradient direction can be depicted by model reparameterization introducing the new variable  $\mathbf{n}$ :

$$\mathbf{n} = \mathbf{P}^{-1}\mathbf{m}, \quad (2.2.20)$$

where  $\mathbf{P}$  is the preconditioning operator matrix and  $\mathbf{m}$  is the model parameter vector, which generates the wavefield  $\mathbf{u}$  using the modeling operator matrix  $\mathbf{L}$ . In this thesis,  $\mathbf{P}$  is the matrix that smoothes the value with the neighboring points based on the Laplace distribution. Taking this new variable, the gradient direction can be reconstitution as

$$\nabla\tilde{C}(\mathbf{n}) = \mathbf{P}'\nabla C(\mathbf{P}\mathbf{n}) = \mathbf{P}'\nabla C(\mathbf{m}), \quad (2.2.21)$$

where prime indicates the adjoint matrix. Hence, preconditioning operator  $\mathbf{P}$

does not affect to anything in the algorithm except for the gradient direction.

From equation (2.2.21), original gradient direction which is written by

$$\nabla C = \frac{\operatorname{Re}\left[(\mathbf{F}^*)^T (\mathbf{L}^{-1})^T \bar{\mathbf{r}}\right]}{\operatorname{Re}\left[\operatorname{diag}\left\{(\mathbf{F}^*)^T \overline{(\mathbf{F}^*)} + \lambda \mathbf{I}\right\}\right]}, \quad (2.2.22)$$

can be rewritten as

$$\nabla C = \mathbf{P}' \frac{\operatorname{Re}\left[(\mathbf{F}^*)^T (\mathbf{L}^{-1})^T \bar{\mathbf{r}}\right]}{\operatorname{Re}\left[\operatorname{diag}\left\{(\mathbf{F}^*)^T \overline{(\mathbf{F}^*)} + \lambda \mathbf{I}\right\}\right]}. \quad (2.2.23)$$

However, in practice, the gradient direction is scaled to compensate the geometrical spreading so that the preconditioning operator is applied when the gradient direction computation and scaling procedure are completed. There are several schemes for the gradient weighting with respect to each frequency component. For convenience, I only use a normalizing weighting method as follows:

$$\nabla C = \mathbf{P}' \left\| \frac{\operatorname{Re}\left[(\mathbf{F}^*)^T (\mathbf{L}^{-1})^T \bar{\mathbf{r}}\right]}{\operatorname{Re}\left[\operatorname{diag}\left\{(\mathbf{F}^*)^T \overline{(\mathbf{F}^*)} + \lambda \mathbf{I}\right\}\right]} \right\|_{\infty}^{-1} \frac{\operatorname{Re}\left[(\mathbf{F}^*)^T (\mathbf{L}^{-1})^T \bar{\mathbf{r}}\right]}{\operatorname{Re}\left[\operatorname{diag}\left\{(\mathbf{F}^*)^T \overline{(\mathbf{F}^*)} + \lambda \mathbf{I}\right\}\right]}, \quad (2.2.24)$$

where  $\|\cdot\|$  denotes the supremum norm. Equation (2.2.24) is a definitive form of the gradient direction for mono-frequency component. Thus, the parameters are updated by the gradient direction that is summed over each frequency component, and proper step length. Additionally, when the smoothing is

applied to the gradient direction, the extent of smoothness can be controlled by the number of iterations.

### 2.2.5 Source wavelet estimation

For following examples, I assume that the source signature is already known and is independent of excited position for the synthetic data. However, for the real field data, I estimate the source wavelet,  $l_2$ -norm objective function and full Newton method are employed (Song *et al.* 1995; Pratt 1999; Shin and Min 2006). In the frequency domain, for mono-frequency component, modeled wavefield can be expressed by the product of the numerical Green's function  $G$  and source signature:

$$u_{jk} = \left\{ \Re G_{jk} + i \Im G_{jk} \right\} \left\{ \Re f_{\omega} + i \Im f_{\omega} \right\}, \quad (2.2.25)$$

where  $u$  and  $G$  are the modeled wavefield and the numerical Green's function, respectively. And  $f_{\omega}$  is the source signature at angular frequency  $\omega$ . Subscripts  $j$  and  $k$  indicate the source and receiver indices, and  $i = \sqrt{-1}$ . Real and imaginary parts for each variable are expressed by prefixes  $\Re$  and  $\Im$ , respectively. Let the observed data  $d_{jk} = \Re d_{jk} + i \Im d_{jk}$ , then, taking objective function gives

$$C_{src} = \frac{1}{2} \sum_{src} \sum_{rcv} \left\{ \begin{aligned} & \left( \Re G_{jk} \Re f_{\omega} - \Im G_{jk} \Im f_{\omega} - \Re d_{jk} \right)^2 \\ & + \left( \Re G_{jk} \Im f_{\omega} + \Im G_{jk} \Re f_{\omega} - \Im d_{jk} \right)^2 \end{aligned} \right\}. \quad (2.2.26)$$

By using Taylor series expansion, function  $C_{src}$  can be expanded as

$$C_{src}(\mathbf{x} + \Delta \mathbf{x}) = C_{src}(\mathbf{x}) + \Delta \mathbf{x}^T \nabla C_{src} + \frac{1}{2} \Delta \mathbf{x}^T \mathbf{H}_{src} \Delta \mathbf{x} + O(|\Delta \mathbf{x}|^3), \quad (2.2.27)$$

where  $\mathbf{x} = [\Re f_{\omega} \quad \Im f_{\omega}]^T$ ,  $\Delta \mathbf{x} = [\Delta \Re f_{\omega} \quad \Delta \Im f_{\omega}]^T$ ,  $\mathbf{H}_{src}$  is the Hessian matrix with respect to  $\Re f_{\omega}$  and  $\Im f_{\omega}$ . To figure out  $\Delta \mathbf{x}$  that minimizes the objective

function, partial derivative objective function with respect to  $\Re f_\omega$  and  $\Im f_\omega$  become to be zero, then equation (2.2.27) gives

$$\Delta \mathbf{x} = -\mathbf{H}_{src}^{-1} \nabla C_{src}. \quad (2.2.28)$$

Thus, the gradient and the Hessian can be written as

$$\nabla C_{src} = \begin{bmatrix} \frac{\partial C_{src}}{\partial \Re f_\omega} \\ \frac{\partial C_{src}}{\partial \Im f_\omega} \end{bmatrix} = \begin{bmatrix} \sum_{src} \sum_{rcv} \{ \Re f_\omega (\Re G_{jk}^2 + \Im G_{jk}^2) - (\Re d_{jk} \Re G_{jk} + \Im d_{jk} \Im G_{jk}) \} \\ \sum_{src} \sum_{rcv} \{ \Im f_\omega (\Re G_{jk}^2 + \Im G_{jk}^2) + (\Re d_{jk} \Re G_{jk} - \Im d_{jk} \Im G_{jk}) \} \end{bmatrix} \quad (2.2.29)$$

and

$$\mathbf{H}_{src} = \begin{bmatrix} \sum_{src} \sum_{rcv} \{ \Re G_{jk}^2 + \Im G_{jk}^2 \} & 0 \\ 0 & \sum_{src} \sum_{rcv} \{ \Re G_{jk}^2 + \Im G_{jk}^2 \} \end{bmatrix}. \quad (2.2.30)$$

Substituting equations (2.2.29) and (2.2.30) into equation (2.2.28) gives

$$\Delta \mathbf{p} = \begin{bmatrix} -\Re f_\omega + \frac{\sum_{src} \sum_{rcv} (\Re d_{jk} \Re G_{jk} + \Im d_{jk} \Im G_{jk})}{\sum_{src} \sum_{rcv} (\Re G_{jk}^2 + \Im G_{jk}^2)} \\ -\Im f_\omega - \frac{\sum_{src} \sum_{rcv} (\Re d_{jk} \Im G_{jk} - \Im d_{jk} \Re G_{jk})}{\sum_{src} \sum_{rcv} (\Re G_{jk}^2 + \Im G_{jk}^2)} \end{bmatrix}. \quad (2.2.31)$$

Using equation (2.2.28), full Newton method can update the source wavelet, and then it is estimated at once. However, the Green's function is calculated numerically by using the initial guess that deviates from the true value so that the source wavelet has to be obtained iteratively as the model parameter.

## Chapter 3. Multiparameter inversion

### 3.1 Sensitivity analysis

Increasing the number of parameters makes FWI to be harder and weaker, because of the increase of the non-linearity, ill-posedness and possibility of being trapped in local minima. Subsurface parameters are related to each other, and there must be an inter-dependency and trade-offs so that FWI needs to be more stable, robust and accurate. Numerous studies have devoted to solve the inverse problems with regularization to avoid strong non-linearity and to achieve the robustness of the FWI. Among them, multi-scale inversion and regularization has been applied to FWI for more accurate and stable results. However, considering multiparameter, it is not a simple problem. A hierarchical inversion has been regarded as a promising method to reconstruct the multiparameter. To design the hierarchical inversion, there should be an order that is which parameter is inverted earlier with a priority or later. Considering that each parameter behaves individually but affects each other inter-dependently, relationships among the parameters and sensitivity of each parameter are investigated before building up the hierarchical inversion strategy. Thus, as a foundation of the hierarchical inversion method, each parameterization is analyzed by various points of approaches.

### 3.1.1 Comparison of mathematical formulae

As described in the earlier section, the gradient direction is efficiently computed by using the back-propagation technique based on its adjoint state. The product of the partial derivative wavefield with respect to the model parameter and residuals can be substituted the product of the virtual source matrix and back-propagated residuals. Remember that the partial derivative wavefield and the gradient direction become to be dominantly affected by the virtual source matrix, because the back-propagated residuals are the same whichever parameterization is used for modeling (as in equations 2.2.6 and 2.2.7):

$$\frac{\partial C(\mathbf{m})}{\partial m_k} = \text{Re} \left[ (\mathbf{f}_k^*)^T (\mathbf{L}^{-1})^T \bar{\mathbf{r}} \right], \quad (3.1.1)$$

where

$$\mathbf{f}_k^* = -\frac{\partial \mathbf{L}}{\partial m_k} \mathbf{u}. \quad (3.1.2)$$

Thus, comparing the virtual source matrices, differences among each parameterization can be clarified. The virtual sources of each parameterization can be written as

$$\frac{\partial \mathbf{L}_e^{\text{V-D}}}{\partial v} = \frac{2\omega^2}{v^3 \rho} \mathbf{M}_e \quad \text{and} \quad \frac{\partial \mathbf{L}_e^{\text{V-D}}}{\partial \rho} = \frac{\omega^2}{v^2 \rho^2} \mathbf{M}_e - \frac{1}{\rho^2} \mathbf{S}_e \quad (3.1.3)$$

for velocity–density parameterization,

$$\frac{\partial \mathbf{L}_e^{\text{B-D}}}{\partial K} = \frac{\omega^2}{K^2} \mathbf{M}_e \quad \text{and} \quad \frac{\partial \mathbf{L}_e^{\text{B-D}}}{\partial \rho} = -\frac{1}{\rho^2} \mathbf{S}_e \quad (3.1.4)$$

for bulk modulus–density parameterization,

$$\frac{\partial \mathbf{L}_e^{\text{I-D}}}{\partial I} = \frac{2\rho\omega^2}{I^3} \mathbf{M}_e \quad \text{and} \quad \frac{\partial \mathbf{L}_e^{\text{I-D}}}{\partial \rho} = -\frac{\omega^2}{I^2} \mathbf{M}_e - \frac{1}{\rho^2} \mathbf{S}_e \quad (3.1.5)$$

for impedance–density parameterization,

$$\frac{\partial \mathbf{L}_e^{\text{I-V}}}{\partial v} = \frac{\omega^2}{Iv^2} \mathbf{M}_e + \frac{1}{I} \mathbf{S}_e \quad \text{and} \quad \frac{\partial \mathbf{L}_e^{\text{I-V}}}{\partial I} = \frac{\omega^2}{I^2v} \mathbf{M}_e - \frac{v}{I^2} \mathbf{S}_e \quad (3.1.6)$$

for impedance–velocity parameterization. As you can see, there are interdependencies. Except for bulk modulus–density parameterization, the virtual sources for each parameterization include the counterpart parameter. That is, the virtual sources with respect to each parameter in equations (3.1.3) to (3.1.6) affect each other and reflect the characteristics of not only its own parameter but also counterpart parameter.

### 3.1.2 Comparison of radiation patterns

In general, it is noted that calculating the partial derivative wavefield can derive the radiation patterns of parameters. This is considered in the same manner with proceeded studies about Rayleigh scattering and Born scattering in the acoustic and elastic media (Rayleigh 1945; Aki and Richard 1980; Ikelle 1996; Wu and Aki 1985; Forgues and Lambaré 1997). Taking partial derivatives to the scattered wavefields with respect to the model parameter gives the derivative terms, which are relevant to the angle for each parameter. Considering only the P-P reflection in the acoustic media, Forgues and Lambaré (1997) suggested the diffraction pattern  $\mathbf{D}$  for various kinds of parameterizations:

$$\begin{aligned}\mathbf{D}_{k,\rho} &= (-1 \quad -\cos\theta), \\ \mathbf{D}_{v,\rho} &= \left(-2 \quad -2\cos^2\frac{\theta}{2}\right), \\ \mathbf{D}_{l,\rho} &= \left(-2 \quad -2\sin^2\frac{\theta}{2}\right)\end{aligned}$$

and

$$\mathbf{D}_{l,v} = \left(-2\cos^2\frac{\theta}{2} \quad -2\sin^2\frac{\theta}{2}\right). \quad (3.1.7)$$

From the point of view of the FWI, these derivative terms indicate the radiation patterns of the partial derivative wavefields that are recognized as the radiation pattern of the virtual sources as well. Although the radiation pattern can be called as a scattering pattern or diffraction pattern, it will be called as a radiation pattern for convenience in following. The partial

derivative wavefield with respect to the model parameter is regarded as a following wavefield generated by the seismic source and scattered point (or diffracted point). Because this radiation pattern, also known as scattering pattern or diffraction pattern, comprises with a product of the partial derivative modeling operator with respect to the model parameter and the modeled wavefield, the radiation pattern completely depends the virtual source. This characteristic addresses that each parameter in each parameterization shows distinct radiation patterns. In addition, the different radiation patterns indicate how each parameter behaves in different scattering angle and is coupled or decoupled in FWI process. In this section, the radiation patterns are estimated numerically by computing the partial derivative wavefield in the finite-element modeling approach for four parameterizations suggested in the ‘Forward problem’ part: velocity–density, bulk modulus–density, impedance–density and impedance–velocity.

To show the radiation pattern for each parameterization, the synthetic homogeneous models are assumed whose velocity is  $1.5 \text{ km s}^{-1}$  and density is generated by empirical formula (Gardner *et al.* 1974). Figure 3.1.1 is an example of the radiation pattern of the velocity in velocity–density parameterization for showing how to plot the radiation patterns in this study. It is obtained by the secondary propagation of the virtual source using the modeling operator, and its variations in amplitude address the characteristics of each diffractor. To obtain more comparable images, the values are interpolated which are located at the same distance from the diffractor and plot those values on a plane as a function of the angle as in Figure 3.1.2. The value

on each angle is interpolated by using the values at adjacent four vertexes. In addition, because the finite-element method have used in this simulation, the virtual sources are located at the four vertexes of an element. Hence, to maintain the symmetry of the propagation of the virtual secondary source, source function is interpolated, too. Figure 3.1.3 shows the radiation patterns for four parameterizations. It is easily observed that the radiation patterns for both two parameters in the same parameterization are overlapped and interfered in some range of angle. Overlapping represents that inverting two parameters simultaneously can cause problems and cannot reconstruct parameters well. These overlapped radiation patterns are observed in other parameterizations (Figures 3.1.3a, 3.1.3b, 3.1.3c). For these three parameterizations, it is observed that the radiation patterns of the velocity, bulk modulus and impedance show the isotropic patterns for whole range of angle whereas those of density are deflected in some directions. From these analyses, it is expected that a parameter which has the isotropic pattern behaves dominantly and reconstructed well in FWI process while the FWI may not give us well inverted result for the density compared with the counterpart parameters for each parameterization. Meanwhile, the impedance–velocity parameterization shows the compartmental patterns for narrow and wide angles. In other words, the scattered energies for each parameter are dominant in different ranges of angles, and then the inter-dependencies or interferences are weaker than the other parameterization in the impedance–velocity parameterization. These are the reason why this parameterization has been regarded as a judicious parameterization for multiparameter estimation.

For more quantitative interpretation of this radiation pattern and to figure out the meaning of radiation pattern more clearly, the impedance–velocity parameterization is used for an example. Figure 3.1.4 shows the schematic diagram that shows the behavior of the velocity in the impedance–velocity parameterization, which shows downward radiation pattern; it is assumed that there are few or no information when the angle is smaller than  $45^\circ$ , roughly; In other words, reconstruction of the velocity requires the far offsets, which have the angle ranging over  $45^\circ$ . Because of the radiation pattern of the velocity, if FWI uses offsets ranging from the source to  $h_1$  so that the information from the shallower parts than the depth of  $h_1$  is retrieved only (theta is  $45^\circ$ ); targeted parameter is expressed by ‘A’. This is the same for the case of  $h_2$  expressed in ‘B’. If FWI employs offsets ranging from the source to  $h_2$ , there are no or few information from the parameter located at the depth of  $h_2$  that returns from the part deeper than  $h_2$ . In this case, however, the information from the parameter located in A where is shallower than B, can be received using the offset  $h_2$ . That is, FWI requires that the offsets have the length as the depth we want to consider in inversion. On the other hand, the impedance can be reconstructed by only the near offsets, because the radiation angle shows the narrow band from the source. FWI results of the impedance would be similar whichever range of offsets used. In the similar vein, the coverage we can infer is expected. In Figure 3.1.5a, it is observed that the offset we use become a depth we can see and the parts in grey color would be an area we can see using the downward radiation pattern. If the offset as the same as the depth is used, there are few or no information out of the range of

the half circle even though the very small range of the offset can receive the information. So, considering the numerous sources in FWI process, the coverage of the FWI is shown in Figure 3.1.5b.

To verify whether this properties are observed in practice or not, numerical tests are performed that is a comparison of the gradient direction at the first stage of the FWI with respect to the range of the offset. Detailed set-up of the FWI will be omitted. Figures 3.1.6 shows the true and initial models used for the numerical tests. Density is assumed to be homogeneous. Figures 3.1.7 to 3.1.8 show the gradient directions of the impedance and velocity with respect to the number of maximum offset as a quarter, two quarters and three quarters of depth and its original depth. In general, it is thought that the less number of offset is used, the less information we can obtain. However, the gradient directions of the impedance in Figure 3.1.7 show the similar results even if the FWI employs different range of the offset for each case. As aforementioned, the radiation pattern of the impedance has narrow range of the angle and it does not require the far offset information to reconstruct the impedance. Although the impedance can be retrieved well only with near offset, it is reasonable to consider the offsets as much as we can use. On the other hand, for velocity, the results considerably depend on the number of offsets. When the maximum offset is three quarters of the depth, Figure 3.1.8b shows that the penetrating depth becomes shallower three quarters than the Figure 3.1.8a. Because there is no or few information within  $45^\circ$ , we cannot recover the information below that depth. In Figure 3.1.8d, when the maximum is a quarter of the depth, the penetration depth is almost a quarter of

the depth. Thus, the imaging of the velocity needs the far offset information, and it is noted that it reflects the long wave lengths.

From these results, it is noted that velocity–density and bulk modulus–density parameterizations do not require the far range of offsets because the radiation patterns are isotropic or banded at narrow angle only for each parameter while impedance–density and impedance–velocity parameterizations need the far range of offsets for density and velocity, respectively. Particularly, to recover the sufficient information of the density in impedance–density and velocity in impedance–velocity parameterizations, FWI has to employ the offsets longer than the value of the depth.

In the next section, the characteristics of each parameterization in FWI are verified and a hierarchical FWI structure which is appropriate for the multiparameter estimation is suggested.

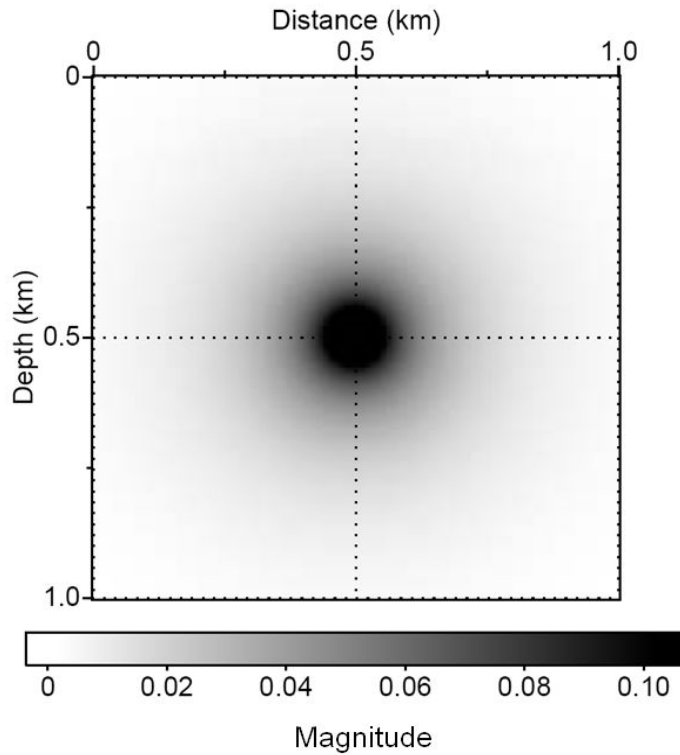


**Figure 3.1.1** Radiation pattern of the velocity in velocity–density parameterization as a representative example. Seismic source is located on the surface at a distance of 0.5 km. Perturbed cell which is employed as a virtual source is located at the center of the model.

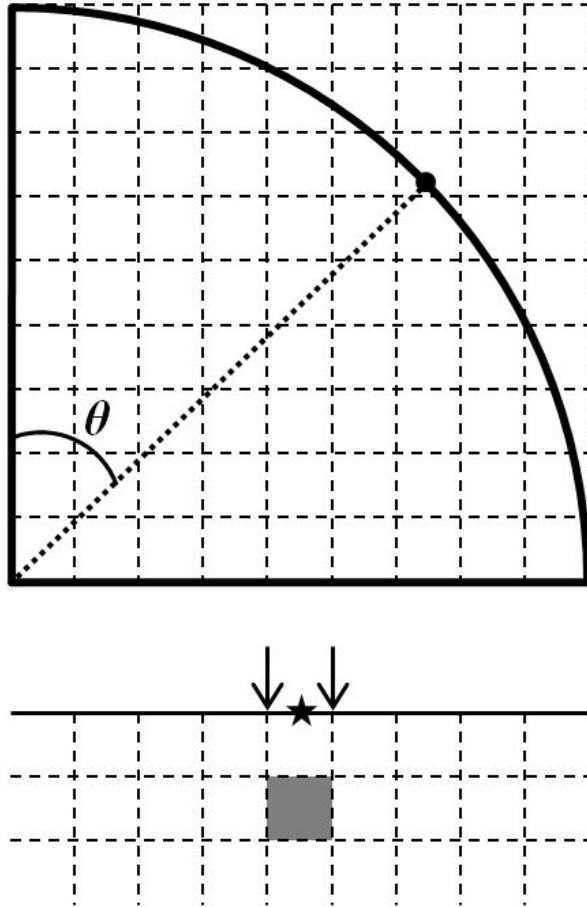


**Figure 3.1.2** Schematic diagram of a method of interpolation. The value on the same distance from the center of a circle where the virtual source is excited is interpolated as a function of angle  $\theta$  (upper figure). Source position is required to be interpolated to maintain the symmetry in element-based scheme (lower figure). The grey rectangular indicates the cell which is used for virtual source by perturbation.

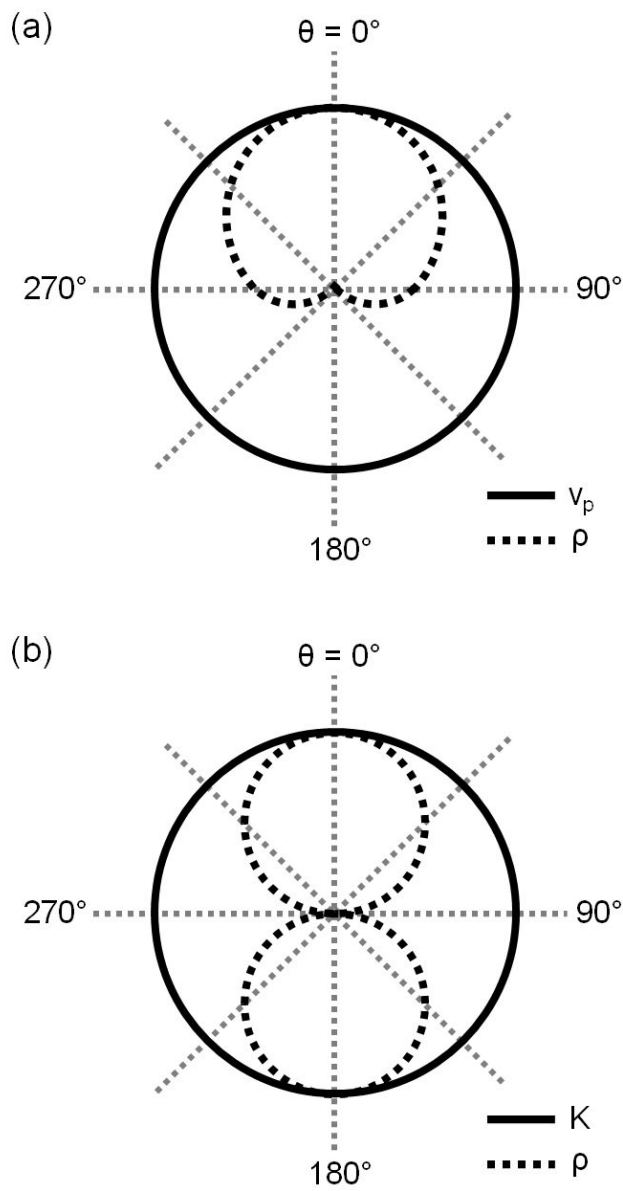


**Figure 3.1.3** Radiation pattern interpolated as a function of the angle for (a) velocity–density, (b) bulk modulus–density, (c) impedance–density and (d) impedance–velocity parameterizations.

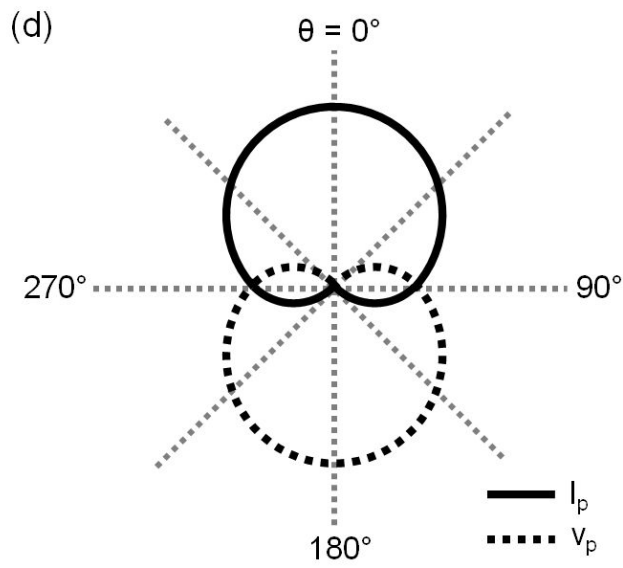
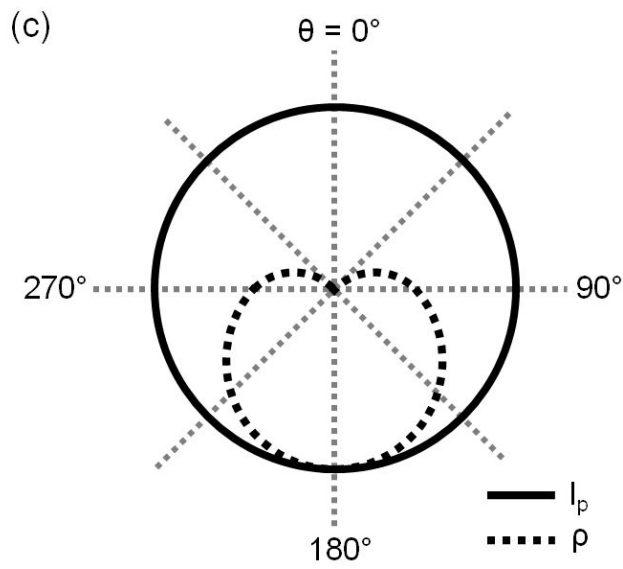


**Figure 3.1.3** (Continued)

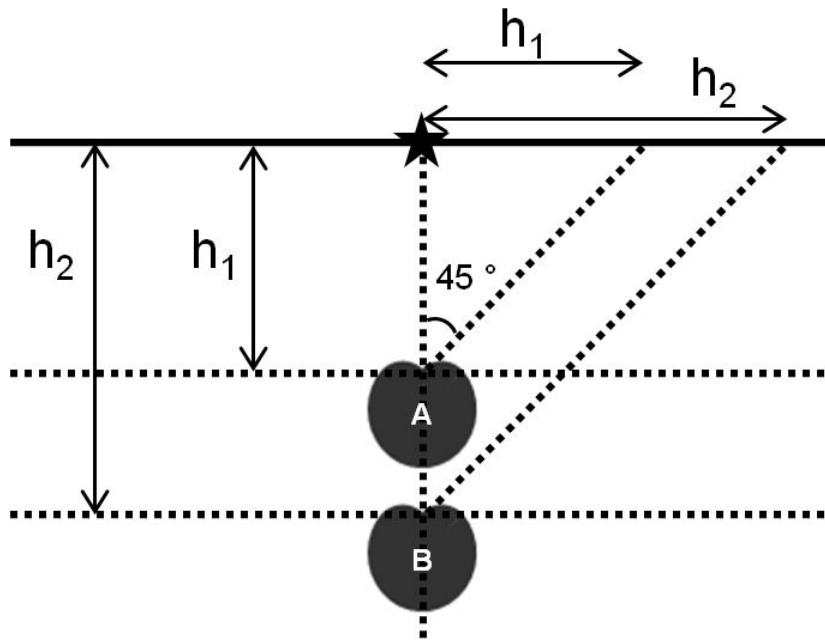


**Figure 3.1.4** Schematic diagram of the relationship between maximum offset and penetrating depth for velocity inversion in impedance–velocity parameterization. A and B show the radiation pattern of the parameters located at depths of  $h_1$  and  $h_2$ .

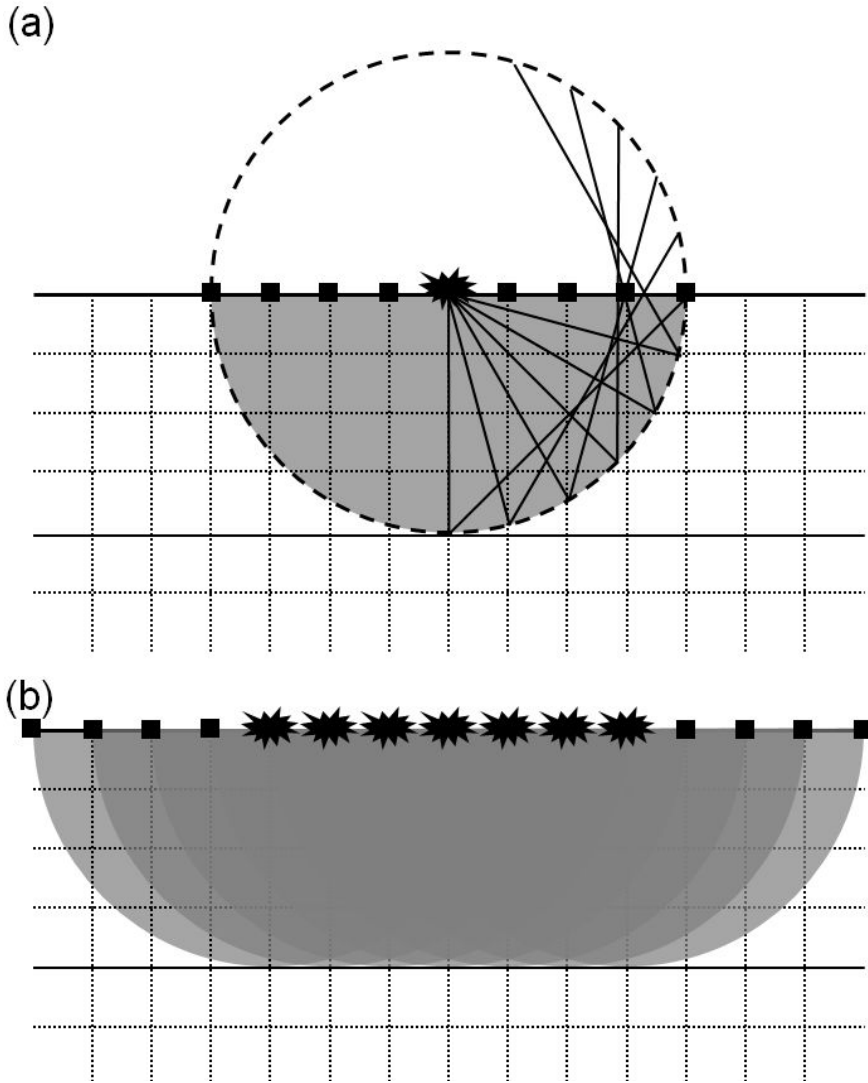


**Figure 3.1.5** Schematic diagram of the behavior of the radiation pattern of velocity in impedance–velocity parameterization. The grey part is the limitation of the recovery of the velocity information from the reflection, which is approximated very roughly. Considering a number of sources in FWI, (b) shows the expected coverage of the velocity information in this parameterization.

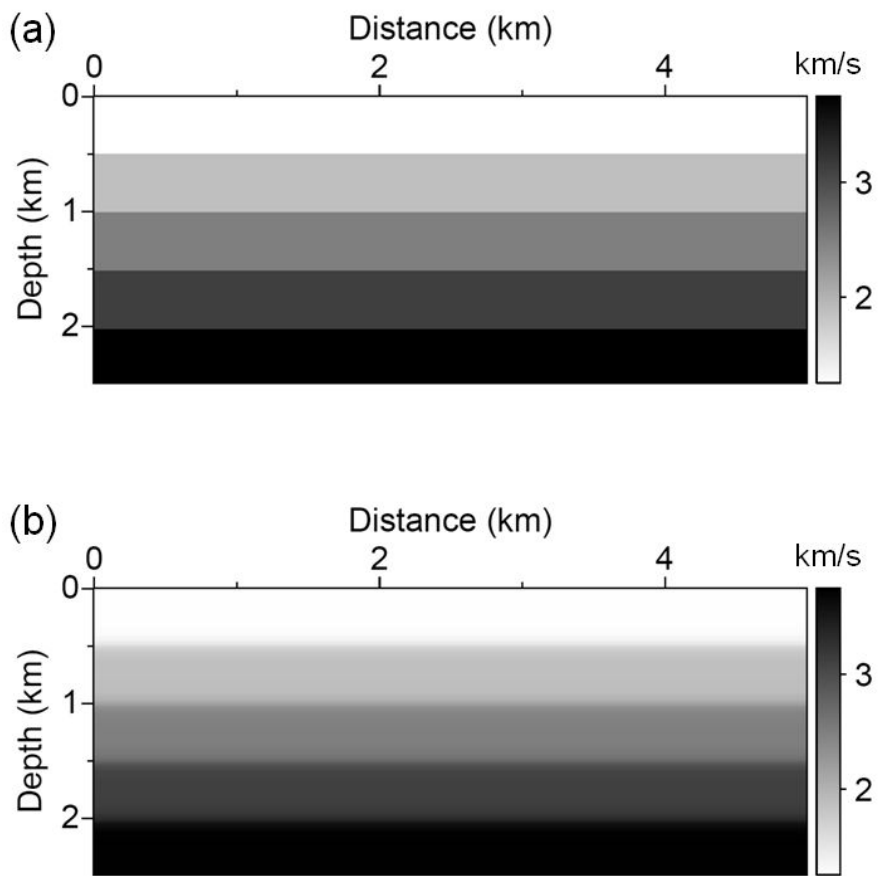


**Figure 3.1.6** The (a) true and (b) initial velocity models used in numerical tests. Because density is assumed to be homogeneous as 2 g/cc, impedance has the same tendency with the velocity.

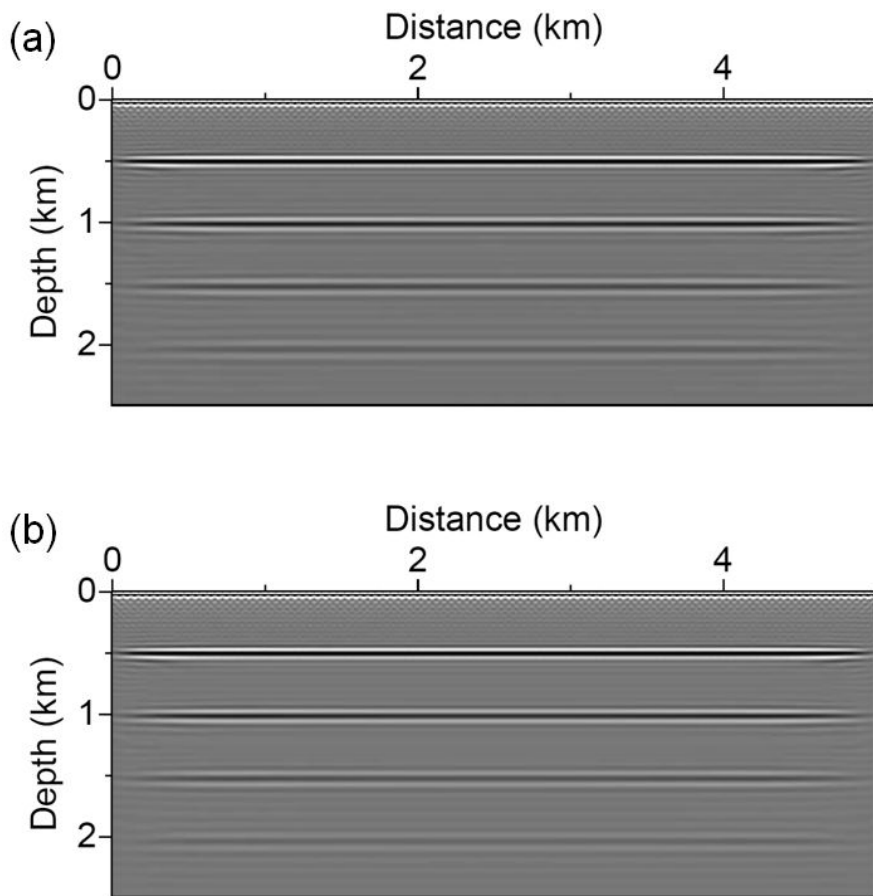


**Figure 3.1.7** The gradient direction at the first iteration for impedance: The maximum off set is the number of (a) 4<sup>th</sup> layer, (b) 3<sup>rd</sup> layer, (c) 2<sup>nd</sup> layer and (d) 1<sup>st</sup> layer, respectively.

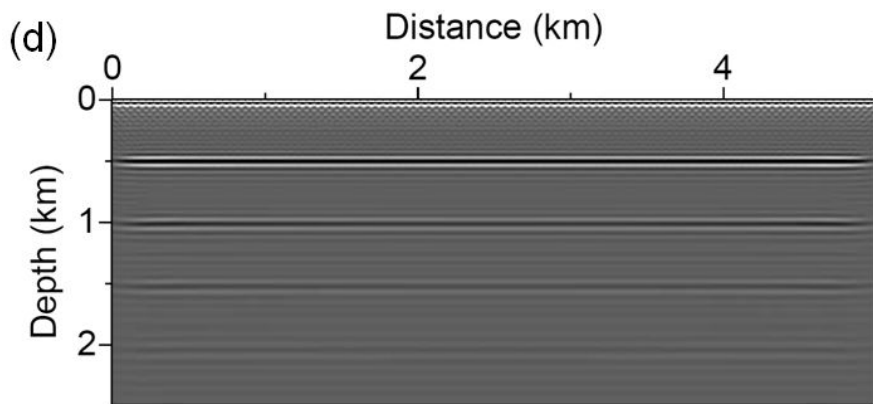
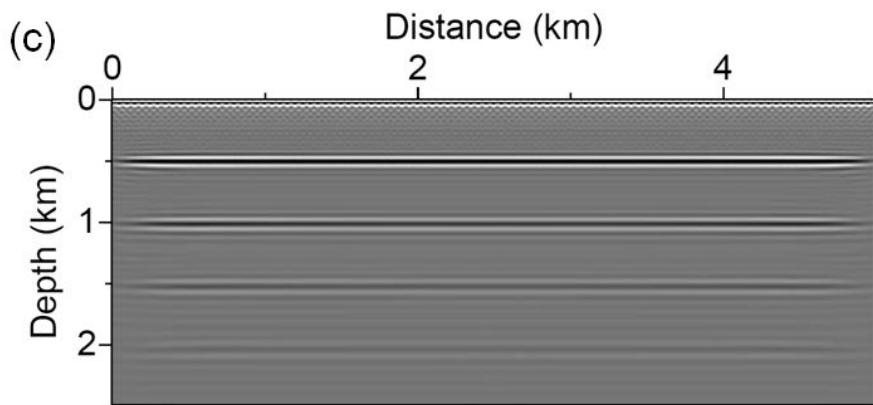
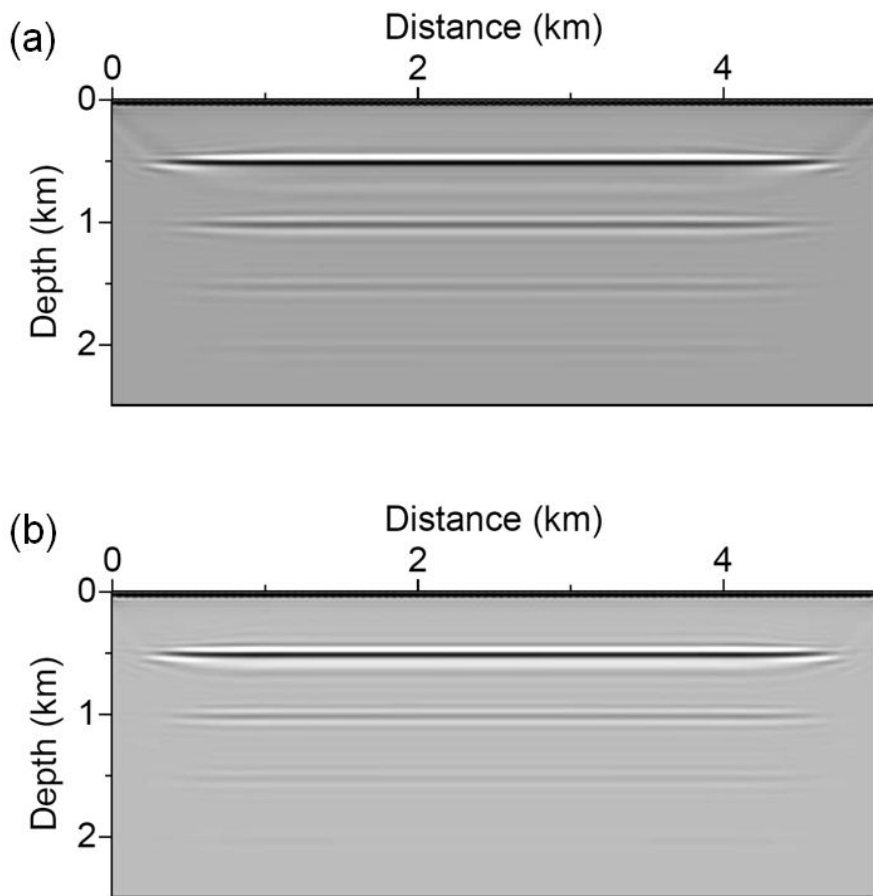


Figure 3.1.7 (Continued)



**Figure 3.1.8** The gradient direction at the first iteration for velocity: The maximum off set is the number of (a) 4<sup>th</sup> layer, (b) 3<sup>rd</sup> layer, (c) 2<sup>nd</sup> layer and (d) 1<sup>st</sup> layer, respectively.

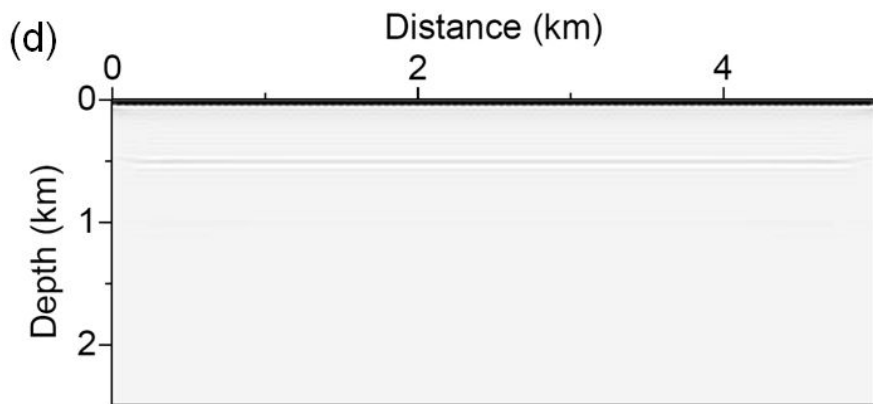
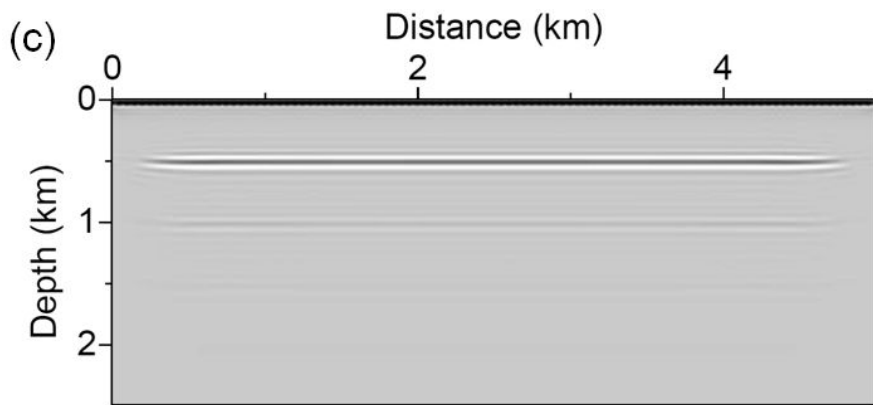


Figure 3.1.8 (Continued)

### 3.1.3 Comparison of conventional FWI results

To investigate how each parameterization behaves in FWI, I apply the conventional FWI algorithm using various parameterizations to the modified version of A'A line of the SEG/EAGE salt model (Aminzadeh *et al.* 1997). Slight modification is applied by adding a water layer to the top of the model. In addition, because the original data only provides  $P$ -wave velocity model, the density model is artificially generated by using the empirical formula suggested by Gardner *et al.* (1974). For the density of main salt body, following House *et al.* (2000), a constant density of  $2.2 \text{ g cm}^{-3}$  is assumed. Figure 3.1.10 shows the true models for velocity and density. The dimension of model is  $15.6 \text{ km} \times 4.2 \text{ km}$  with a grid interval of 20 m. To generate synthetically observed data, the first derivative of a Gaussian function with a maximum frequency of 10 Hz is used for a source signature; using 379 sources and recording over 6 seconds. Within FWI process, the simultaneous-source method is employed for computational efficiency. Because there should be sophisticated methods for simultaneous-source FWI in marine streamer acquisition (Choi and Alkhalifah 2012; Routh *et al.* 2011), it is assumed that the fixed spread acquisition as a land survey, even in offshore environment. Gradually increasing velocity and density ranging from  $1.5$  to  $3.0 \text{ km s}^{-1}$  and  $1.9$  to  $2.3 \text{ g cm}^{-3}$  are used for initial models, respectively, whereas depth, velocity and density of the water layer are assumed to be known. Figure 3.1.11 shows the initial models used for FWI.

Figures 3.1.12 and 3.1.13 show the results of the conventional FWI with

four parameterizations. As it is mentioned in the previous section, except for impedance–velocity parameterization, the velocity is reconstructed well by using the conventional FWI method due to the parameters which have an isotropic radiation pattern for whole range of angle: velocity, bulk modulus and impedance (not applicable to impedance–velocity parameterization). For these three parameterizations, the velocity is extracted directly or based on the relationships  $v = (K/\rho)^{1/2}$  and  $v = I/\rho$ . In impedance–velocity parameterization, because only the far offset information is helpful for imaging the velocity and the energies are scattered only forwardly as in the radiation pattern, the velocity is hard to be recovered well in this parameterization. In Figure 3.1.13, the inversion results of density seem to deviate from the true value for all parameterization. In the midst of spoiled images, velocity–density parameterization seems to be the most stable and accurate. This phenomenon partly reflects the mathematical formulae in equation (3.1.3). The virtual source of the density in this parameterization has a term of velocity. Thus, it can be affected by the well-inverted velocity and follows a tendency of the inverted velocity. Based on the mathematical formulae in equations (3.1.3) to (3.1.6) and the radiation patterns in Figure 3.1.3, other phenomena can be analyzed. In the cases of impedance–density and impedance–velocity parameterizations, reconstructed densities are severely distorted. For impedance–density parameterization, the virtual source of density has an impedance term in its virtual source as in velocity–density parameterization. However, looking at the radiation patterns of density in Figures 3.1.3a and 3.1.3c, the radiation patterns show the opposite directions for each other. In

this case, as the same as velocity in impedance–velocity parameterization, the energies are scattered only forward direction so that the most of energies are concentrated on the far offset range. For this reason, the density cannot be inverted well in impedance–density parameterization even if the impedance gives good agreement. Low-grade density disturbs the velocity estimation when the impedance is divided by the density. Likewise, and as aforementioned often, the velocity in impedance–velocity parameterization cannot provide rational result, and low-grade velocity disturbs the density estimation, neither.

In summary, Table 1 shows the results of the FWI for each parameterization. The three parameterizations, which have the isotropic radiation patterns for at least one parameter, show that they can retrieve the velocity information even though counterpart parameter, density is not estimated well. In impedance–velocity parameterization shows the worst results that cannot recover both parameters. Thus, in the next section, the hierarchical FWI method for multiparameter estimation will be discussed and suggested.

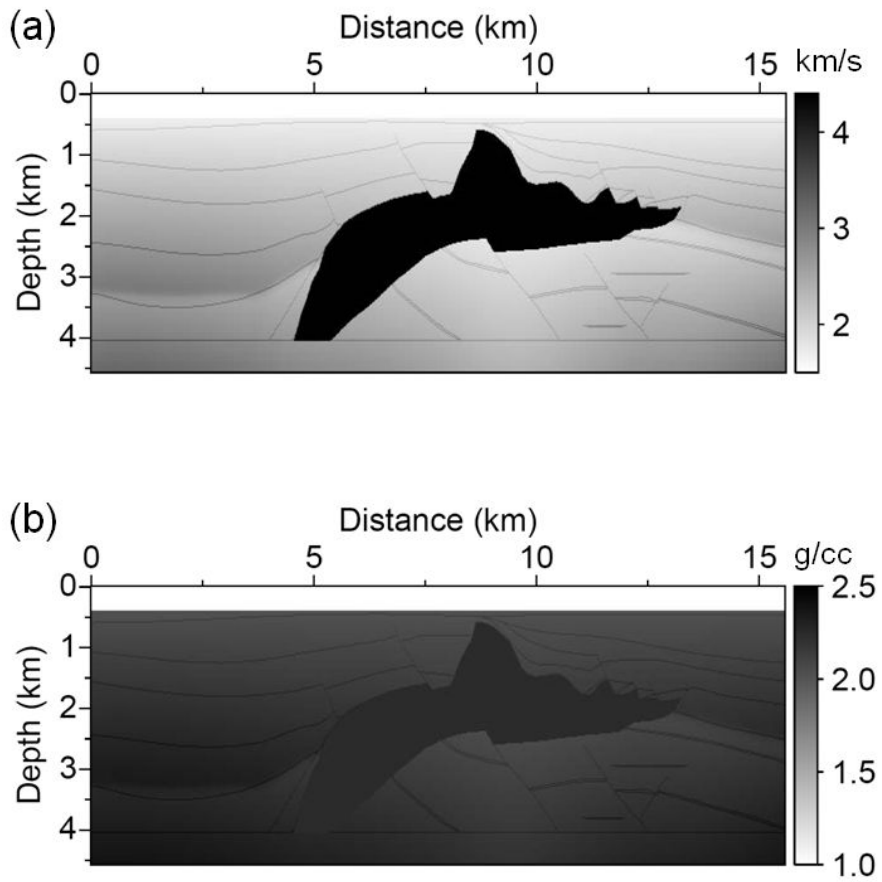


**Figure 3.1.9** A modified version of the AA' line of the SEG/EAGE salt model: (a) velocity and (b) density.

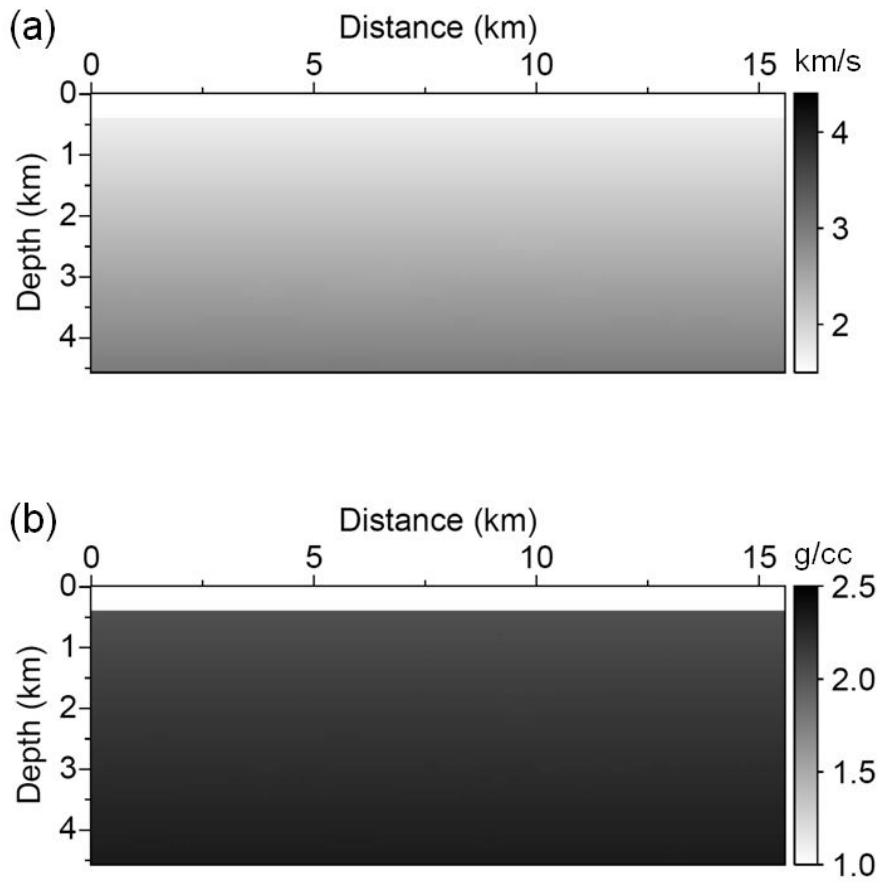


**Figure 3.1.10** Initial models used for FWI: (a) velocity and (b) density.

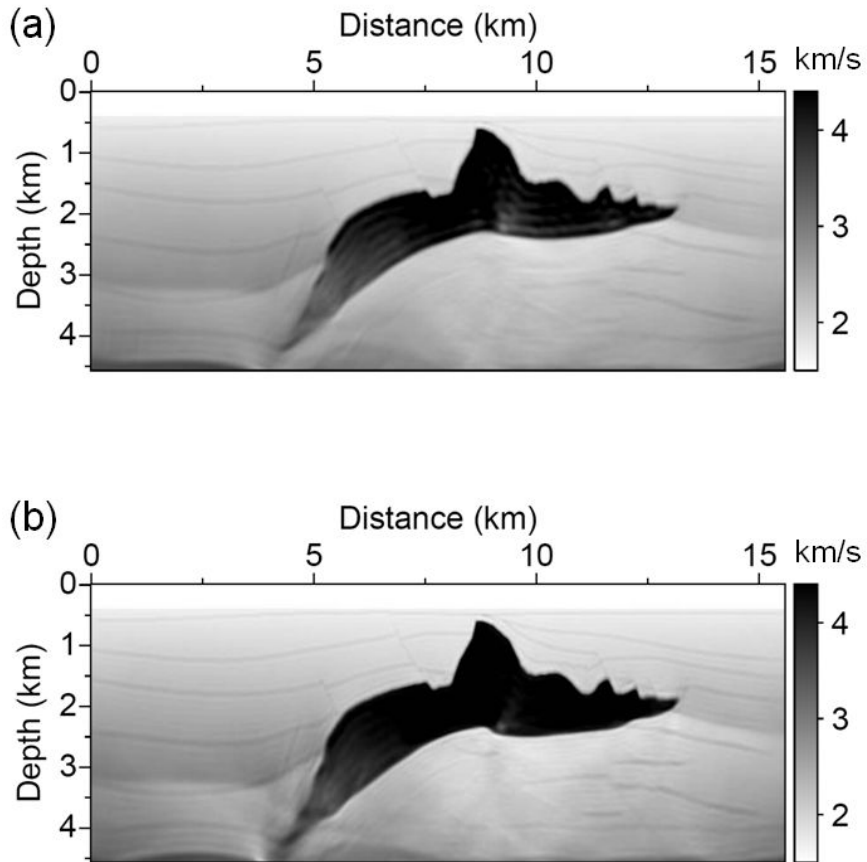


**Figure 3.1.11** Reconstructed velocity model inverted by using (a) velocity–density, (b) bulk modulus–density, (c) impedance–density and (d) impedance–velocity parameterizations, respectively.

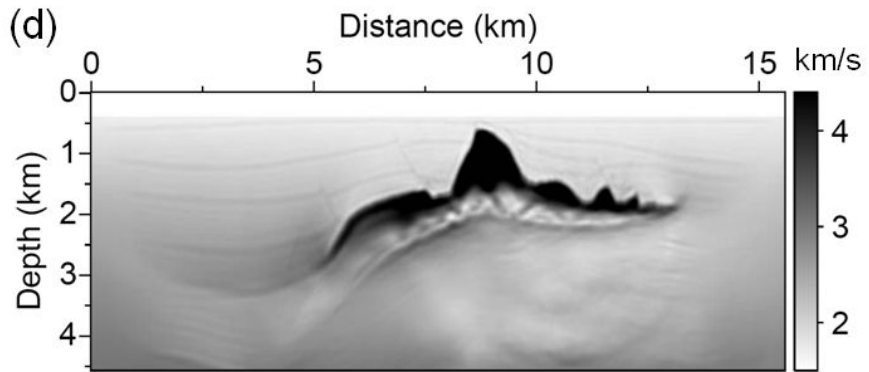
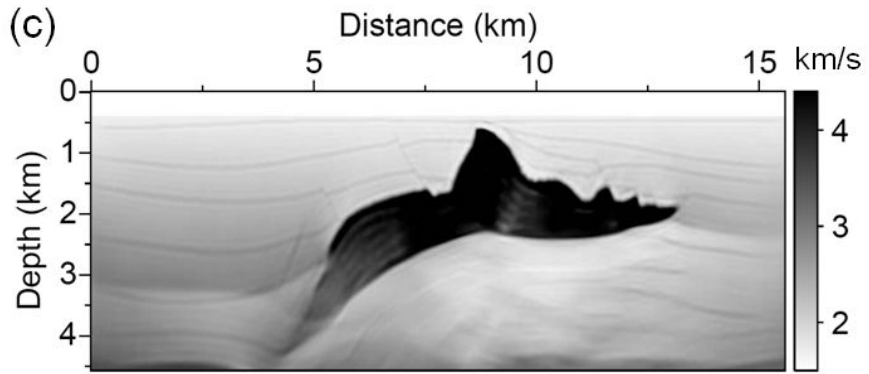
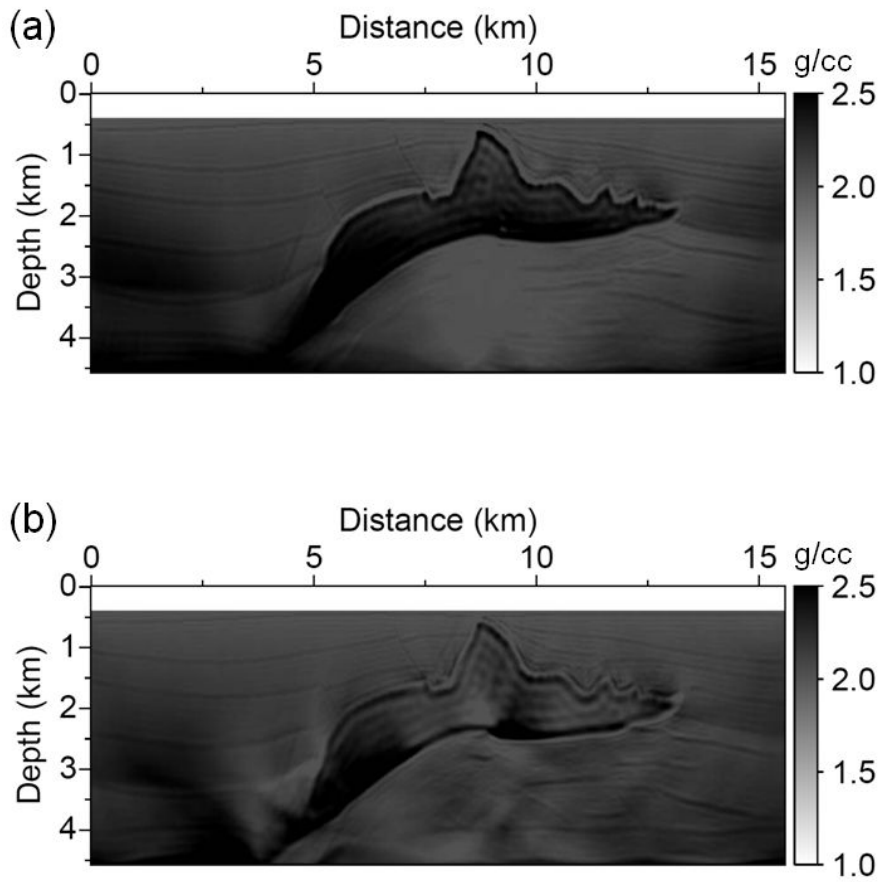


Figure 3.1.11 (Continued)



**Figure 3.1.12** Reconstructed density model inverted by using (a) velocity–density, (b) bulk modulus–density, (c) impedance–density and (d) impedance–velocity parameterizations, respectively.

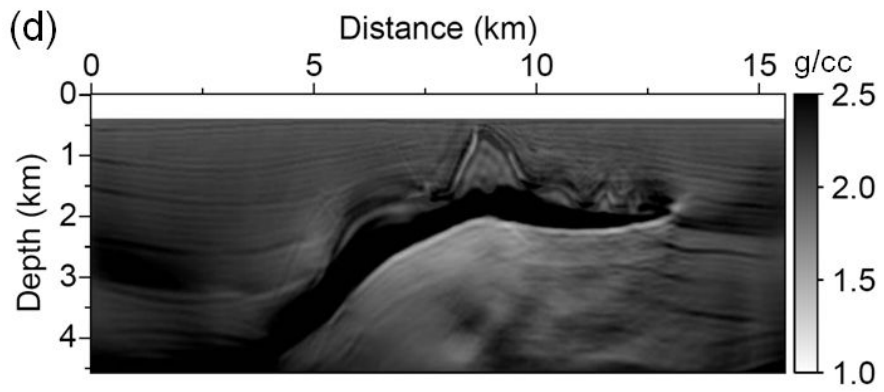
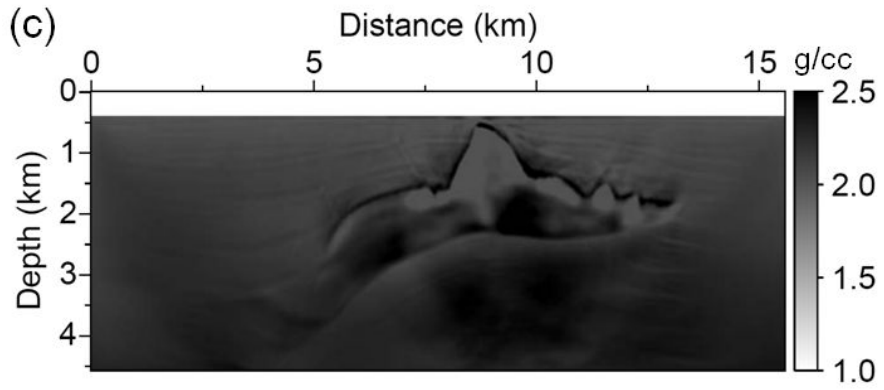


Figure 3.1.12 (Continued)

Parameterization	$K$	$v$	$\rho$	$I$	Output $v$
$(v, \rho)$	-	○	×	-	-
$(K, \rho)$	×	-	×	-	○
$(I, \rho)$	-	-	×	×	○
$(I, v)$	-	×	-	×	-

**Table 1.** Summary of the conventional FWI results.

## **3.2 Hierarchical approach**

In the previous section, it is confirmed that multiparameter inversion of two targeted parameters simultaneously is not able to provide appropriate results for both parameters: one could help to another one, vice versa. Considering the inter-dependency (or interference) and the radiation pattern, multiparameter FWI cannot help suffering from the non-linearity, local-minima and cycle skipping. A hierarchical approach may relieve these problems which consider respective parameter in each stage so that the FWI can reduce the parameter has to take into account. In following section, the hierarchical approach for multiparameter estimation will be suggested, especially about reconstruction of the velocity and density information. The hierarchical strategy for multiparameter estimation comprises two stages; the first stage concentrates to the velocity inversion and the second stage focuses on the density inversion.

### 3.2.1 Stage 1: velocity inversion

As it has already recognized that the velocity is easier to recover than density information in FWI, a hierarchical FWI is designed which focuses on the velocity inversion in the first stage. Considering the dominant parameter first, FWI can be more stable and accurate with relieving non-linearity and probability of getting stuck in local minima. Recall that only in bulk modulus–density parameterization, virtual source (or partial derivative of the modeling operator  $\mathbf{L}$  with respect to the density) of the bulk modulus which has an isotropic radiation pattern does not have density term in mathematical formula (equation 3.1.4), this parameterization can be expected to a proper parameterization for the first stage of the hierarchical inversion. Although using the velocity–density parameterization has been proposed for a hierarchical inversion by Prieux *et al.* (2013), it is questionable whether the density information can be extracted by using this parameterization when the density structure behaves differently from the velocity (specifically, the density does not show a similar tendency with the velocity in salt structure) or not. On the other hand, Jeong and Min (2012) showed that the velocity estimated by bulk modulus–density parameterization is comparable to the true one even the values of bulk modulus and density are wrongly inverted which are called pseudo-bulk modulus and pseudo-density:

$$v = \sqrt{\frac{K_p}{\rho_p}}, \quad (3.2.1)$$

where the subscript  $p$  means ‘pseudo’. That is, during the inversion, density is

fixed as a constant at an arbitrary value for whole model space (except for the water layer when the marine environment is assumed), and the pseudo-bulk modulus is inverted. Wrong values of the pseudo-bulk modulus and pseudo-density can extract the velocity in right direction. Updating pseudo-bulk modulus with a fixed density rather than simultaneous inversion for bulk modulus and density can reduce the negative effect of a wrongly estimated density and the number of unknowns which is one of the reasons for trade-offs in multiparameter inversion. According to these advantages, pseudo-bulk modulus–density parameterization is assigned as a prior inversion scheme for the hierarchical approach.

Several tests are performed to confirm whether the pseudo-density which is fixed at a constant gives reasonable result or not, and additionally, whether the bulk modulus-density parameterization is suitable for the velocity inversion or not: pseudo-density is fixed at a high ( $2.5 \text{ g cm}^{-3}$ ) or moderate ( $2.0 \text{ g cm}^{-3}$ ) or low ( $1.5 \text{ g cm}^{-3}$ ) value for each case. For a comparison, FWI with velocity–density and impedance–density parameterizations with the pseudo-density are performed, too. Impedance–velocity parameterization is excluded because it cannot be a mono-parametric FWI even with a fixed density. Figures 3.2.1 to 3.2.3 show the FWI results of velocity for each parameterization with the pseudo-density. Every parameterization yield good agreements with the true velocity model, especially bulk modulus–density parameterization gives the most consistent results for various values of density. On the other hand, for the moderate value of density, velocity–density and impedance–density parameterizations provide fairly good results whereas the

results are relatively poor for low or high value of density.

Consequently, because it is hard to obtain the reliable density information in practice, bulk modulus–density parameterization with pseudo-bulk modulus and pseudo-density is the most powerful and the least sensitive for velocity inversion. In addition, choice of the value for pseudo-density as an arbitrary constant is questionable and has to be solved. In this thesis, however, the moderate value ( $2 \text{ g cm}^{-3}$ ) is assumed for all cases in following sections because the moderate value provides rational and stable results.

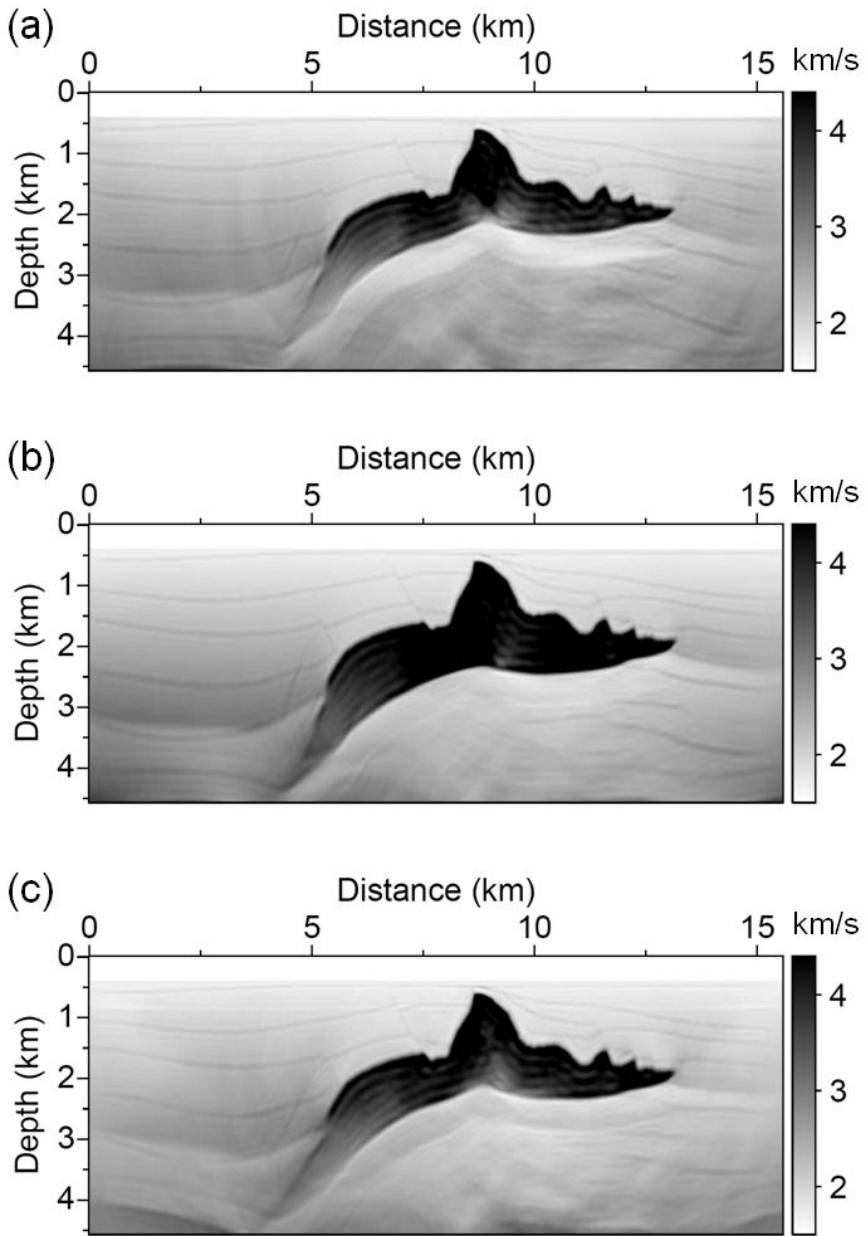


**Figure 3.2.1** Reconstructed velocity model inverted by using velocity–density parameterization with a pseudo-density which is (a) 1.5, (b) 2 and (c) 2.5 g cm<sup>-3</sup>, respectively.

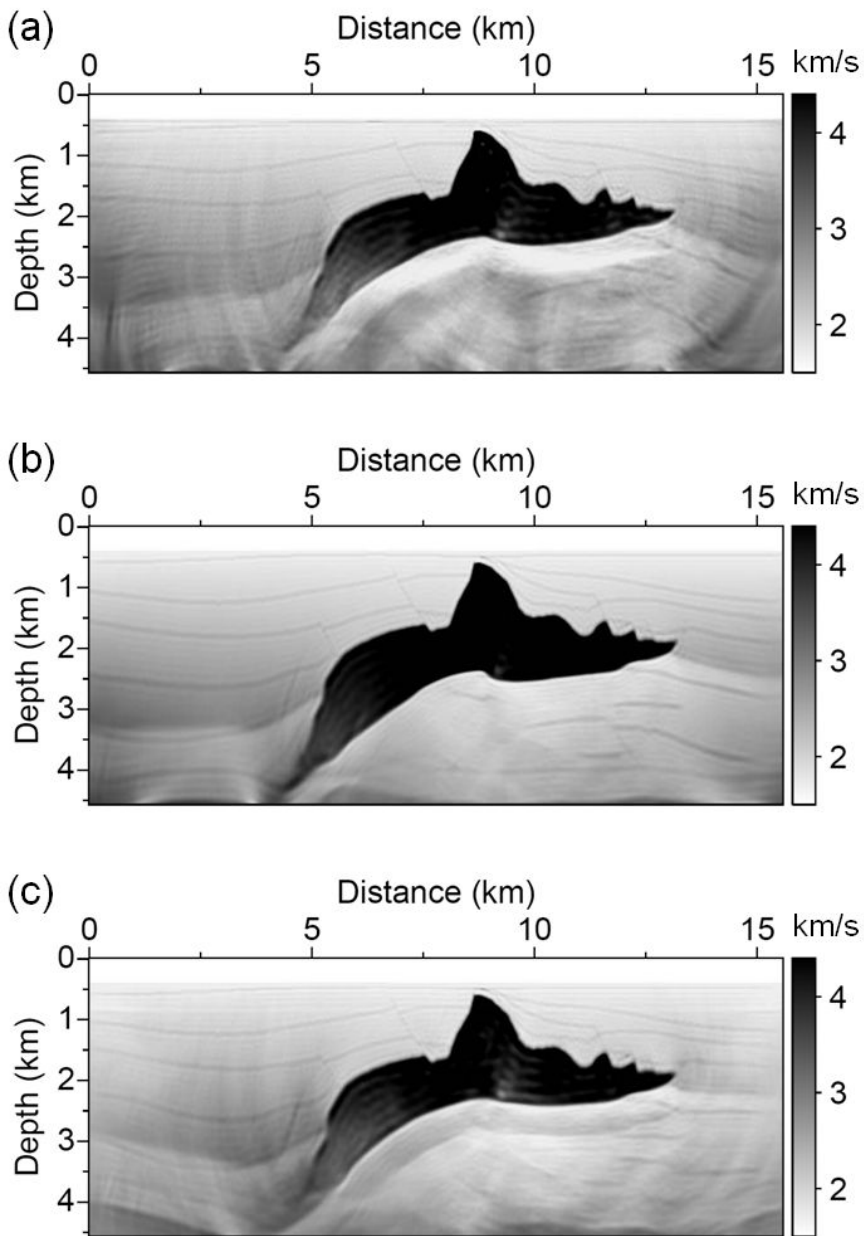


**Figure 3.2.2** Reconstructed velocity model inverted by using bulk modulus–density parameterization with a pseudo-density which is (a) 1.5, (b) 2 and (c) 2.5 g cm<sup>-3</sup>, respectively.

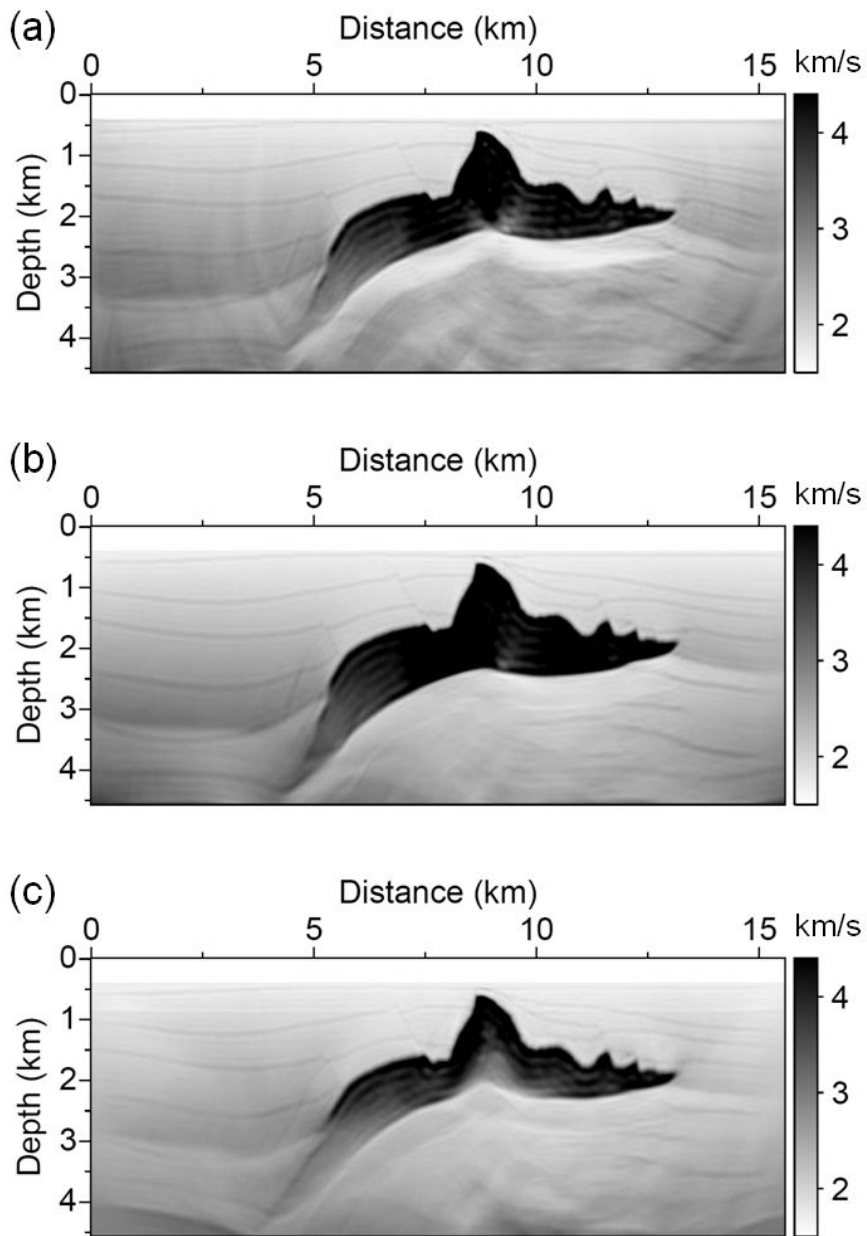


**Figure 3.2.3** Reconstructed velocity model inverted by using impedance–density parameterization with a pseudo-density which is (a) 1.5, (b) 2 and (c) 2.5 g cm<sup>-3</sup>, respectively.

### 3.2.2 Stage 2: density inversion

In the first stage, the velocity is inverted. Based on the velocity obtained, density information is estimated in the second stage. To figure out which parameterization is suitable for the second stage, density inversion using conventional FWI algorithm based on each parameterization is performed. In this case, because sufficient information of the velocity might be able to be provided in the first stage, it is supposed that the true velocity is known in order to concentrate on the density inversion with the accurate velocity; note that, in conventional simultaneous inversion for multiparameter, velocity–density parameterization gives the most reliable result for density; as aforementioned several times, impedance–velocity parameterization is regarded as relevant with confidence. Moreover, even the true velocity is assumed to be known, bulk modulus–density and impedance–density parameterizations are no longer mono-parameteric inversion because the true bulk modulus and true impedance are unknown even from the true velocity information. In Table 2, these properties are summarized. As a result, in here, velocity–density and impedance–velocity parameterizations are only considered for a comparison.

Figure 3.2.4 shows the reconstructed density model based on the velocity–density and impedance–velocity parameterizations, respectively. Both parameterizations yield good results. For more detailed comparison, model misfit is calculated by

$$\varepsilon_{\text{model}} = \frac{\|\mathbf{m}_{\text{inv}} - \mathbf{m}_{\text{true}}\|_2}{\|\mathbf{m}_{\text{true}}\|_2}, \quad (3.2.2)$$

where  $\varepsilon$  is the model misfit error,  $\mathbf{m}_{\text{inv}}$  and  $\mathbf{m}_{\text{true}}$  indicate the inverted model and true model parameter vectors, respectively. As shown in Figure 3.2.5, model misfit error is very similar. Thus, separating the section between main salt body and background media, the model misfit is estimated again in Figure 3.2.6. Because the background area occupies the majority of the model, total misfit only seems to be similar within both parameterizations whereas impedance–velocity parameterization stands out as a lower misfit error for the main salt body as shown in Figure 3.2.6b. Being similar in the background area where the density has a similar tendency with the velocity model, both parameterizations show good agreements with the true model whereas impedance–velocity parameterization shows the strength for the salt body where the density has a reversal tendency comparing to the velocity (relatively high velocity and low density). Based on Figures 3.2.4 and 3.2.6, the impedance–velocity is the most suitable among four parameterizations suggested in this study. In this scheme, there is a positive advantage that an initial guess of impedance can roughly reflect the true value even with the linearly increasing density model because of a sufficiently estimated velocity model in the first stage.

Parameterization	Known	Unknown
(velocity–density)	$v$	$\rho$
(bulk modulus–density)	$v$	$K, \rho$
(impedance–density)	$v$	$I, \rho$
(impedance–velocity)	$v$	$I$

**Table 2.** Known and unknown parameters when the velocity is given in the first stage of the hierarchical inversion.  $v$ ,  $K$ ,  $I$  and  $\rho$  denote the velocity, bulk modulus, impedance and density, respectively.

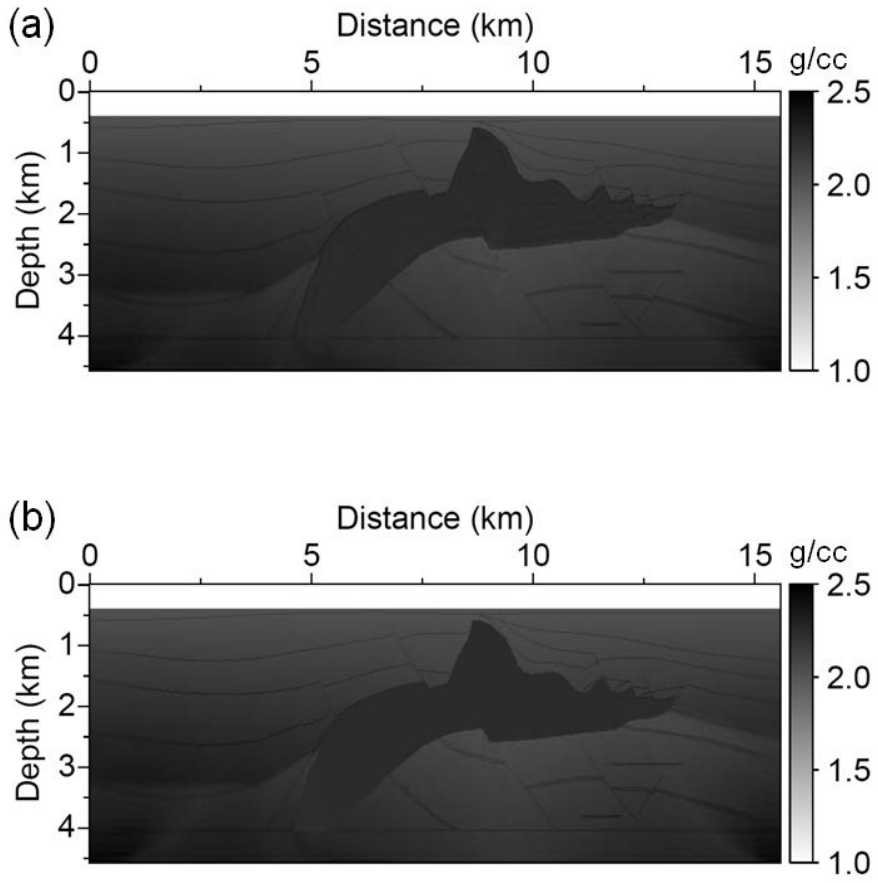


**Figure 3.2.4** Reconstructed density model inverted by using (a) velocity–density and (b) impedance–velocity parameterizations with true velocity, respectively.

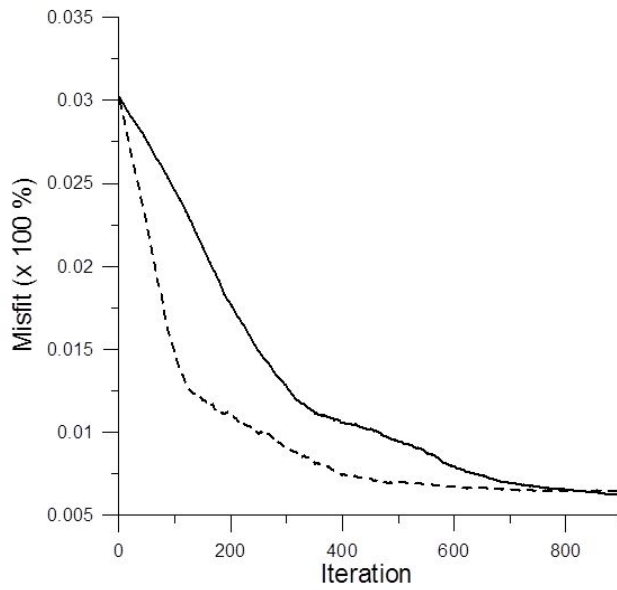


**Figure 3.2.5** Model misfit error between the inverted and true density model. The black solid and dashed lines denote the model misfit error of velocity–density and impedance–velocity parameterizations, respectively.

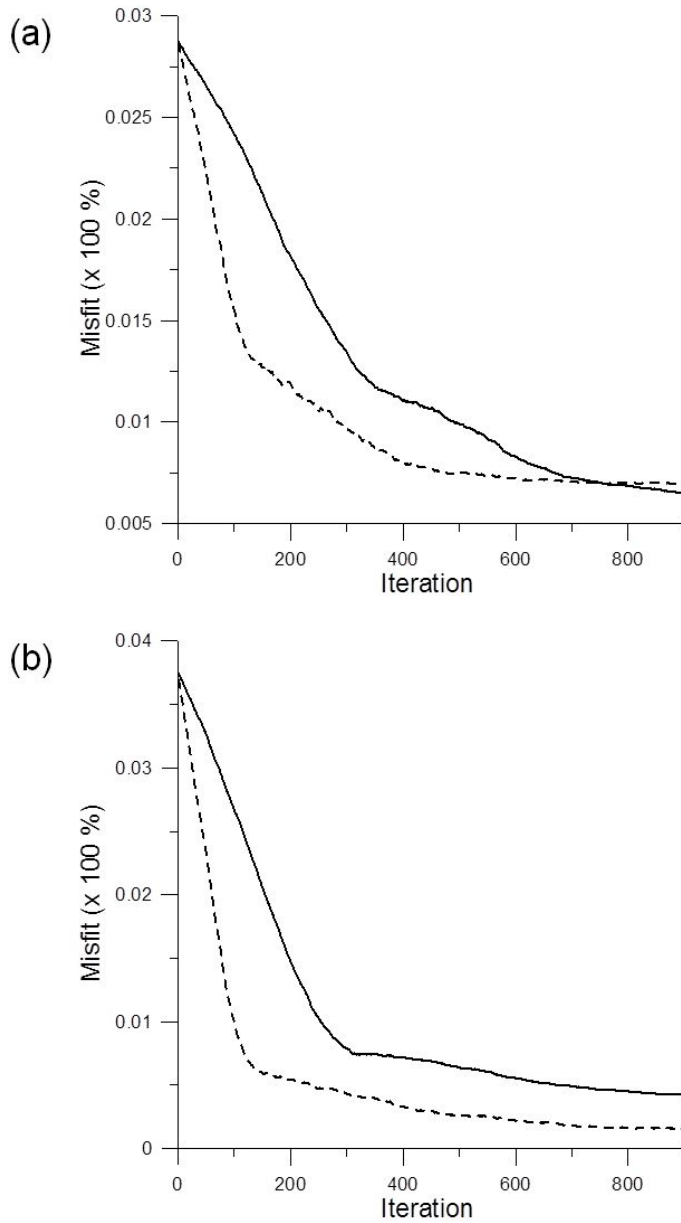


**Figure 3.2.6** Model misfit error between the inverted and true density model for (a) background area and (b) main salt body. The black solid and dashed lines denote the model misfit error of velocity–density and impedance–velocity parameterizations, respectively.

## Chapter 4. Numerical examples

### 4.1 Inversion set-up

Proposed algorithm will be demonstrated by the numerical examples. For solving forward and inverse problems, the frequency-domain finite-element method (Zienkiewicz and Taylor, 2000) is used. For the SEG/EAGE salt model and Marmousi-2 model, forward modeling data as observed data and FWI are performed by the same modeling scheme excluding the real field example. For formerly mentioned two examples, the simultaneous-source FWI is applied by using random phase encoding (Romero *et al.* 2000; Ben-Hadj-Ali *et al.* 2011) for efficiency. Because the simultaneous-source method is only valid to the fixed spread acquisition such as land seismic exploration unless the sophisticated technique is applied (Choi and Alkhalifah 2012; Routh *et al.* 2011), conventional individual-source method is employed for the real field data. In addition, the source signature is assumed to be already known when the simultaneous-source method is employed, whereas it is estimated by using the full Newton method (Song *et al.* 1995; Pratt 1999) for the real field data. Isotropic smoothing is employed for regularization.

## 4.2 Synthetic data examples

### 4.2.1 SEG/EAGE salt model

Two-stage hierarchical FWI is applied to the SEG/EAGE salt model. The detail descriptions of the model and FWI set-up are mentioned and identical to those given in the previous chapter. Figure 4.2.1 shows the reconstructed result for velocity obtained in the first stage. The pseudo-bulk modulus is inverted with fixing the pseudo-density at  $2 \text{ g cm}^{-3}$  for whole dimension of the model excluding the water layer; this result is the same with Figure 3.2.2b. In the first stage, velocity is reconstructed well with the pseudo-bulk modulus as it is expected. In Figure 4.2.2, the true value of bulk modulus and the pseudo-bulk modulus are compared. Note that, there are little deviations between true and pseudo bulk modulus when the density variation is not large, because the bulk modulus is proportional to the square of velocity. Now, FWI proceed to the second stage to invert the density. In the second stage, density is inverted with the velocity model obtained in the first stage and gradually increasing density model as initial guesses. Figure 4.2.3 shows the FWI results for velocity and density using impedance–velocity parameterization in the second stage. Compared with the previous results obtained by the conventional algorithms in Figures 3.1.6 and 3.1.7, it is noted that the hierarchical FWI reconstruct the velocity and density well with significant improvements. Although there are some poor parts in the deeper parts of the salt body, it arises from the poorly estimated velocity as well. It should be noted that the more accurate velocity we use, the more accurate density we can estimate. In

addition, there are oscillations that seem like high-frequency artifacts. Dividing the impedance by the velocity, deviations between short and long wavelength structures may cause these oscillations.

Now, the hierarchical strategy suggested in this thesis is compared with the recently-announced method, which is two-stage inversion strategy using the velocity–density parameterization for both stages. Prioux *et al.* (2013) successfully applied the hierarchical inversion to the Valhall model that has similar geological features for velocity and density. In this case, two-stage inversion can achieve a goal for velocity and density inversion. However, it is questionable whether a previous inversion strategy can provide a superior result for salt-dominant structures. Figure 4.2.4 shows inversion results for velocity and density of SEG/EAGE salt model. Comparing with Figure 4.2.3, it is noted that a hierarchical inversion strategy suggested in this thesis gives more accurate and stable results for the density model. Especially, in Figure 4.2.4, the density is overestimated for the salt body and some parts of the background not as in previous results in Figure 4.2.3. In addition, even velocity model is recovered well for previous results.

In summary, although the density obtained by a hierarchical inversion method suggested in this thesis does not exactly recover the true value of the density model, the inversion results are more consistent and accurate than conventional methods.

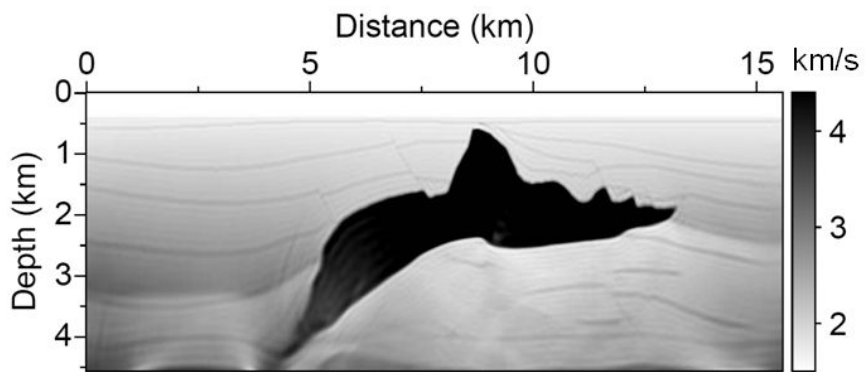


**Figure 4.2.1** Reconstructed velocity model for SEG/EAGE salt model inverted at the 1<sup>st</sup> stage of the hierarchical inversion by using bulk modulus–density parameterization with pseudo-bulk modulus and fixed density as  $2 \text{ g cm}^{-3}$ .

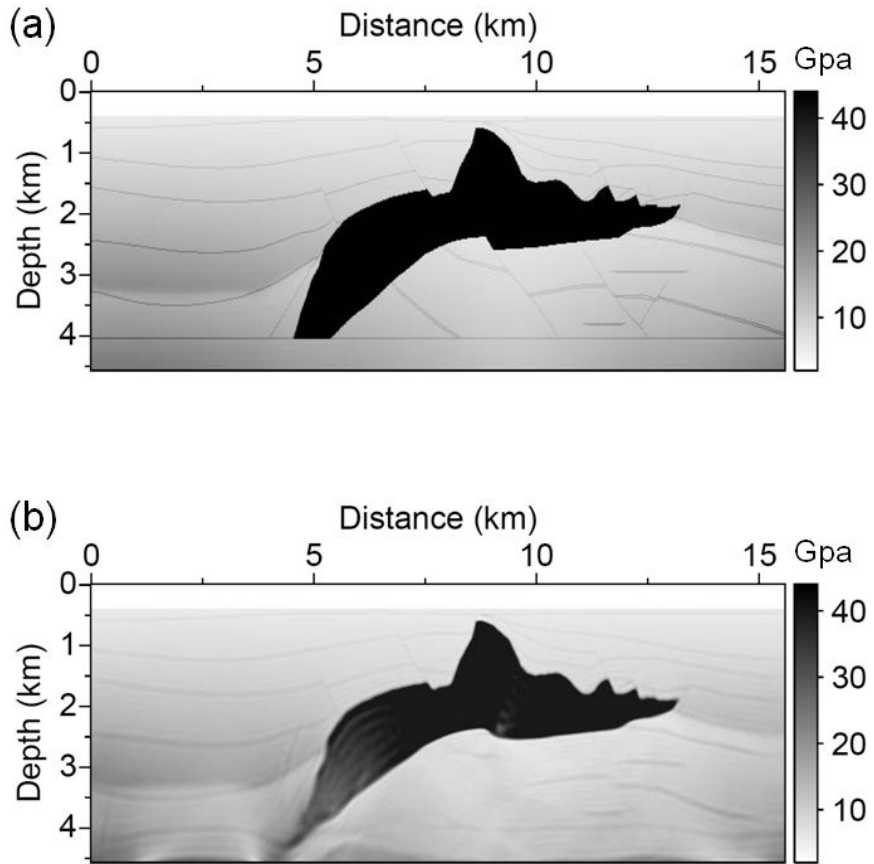


**Figure 4.2.2** (a) The true and (b) inverted pseudo bulk modulus for SEG/EAGE salt model. For an accurate comparison, the maximum and minimum values of the legend are fixed at the same level.

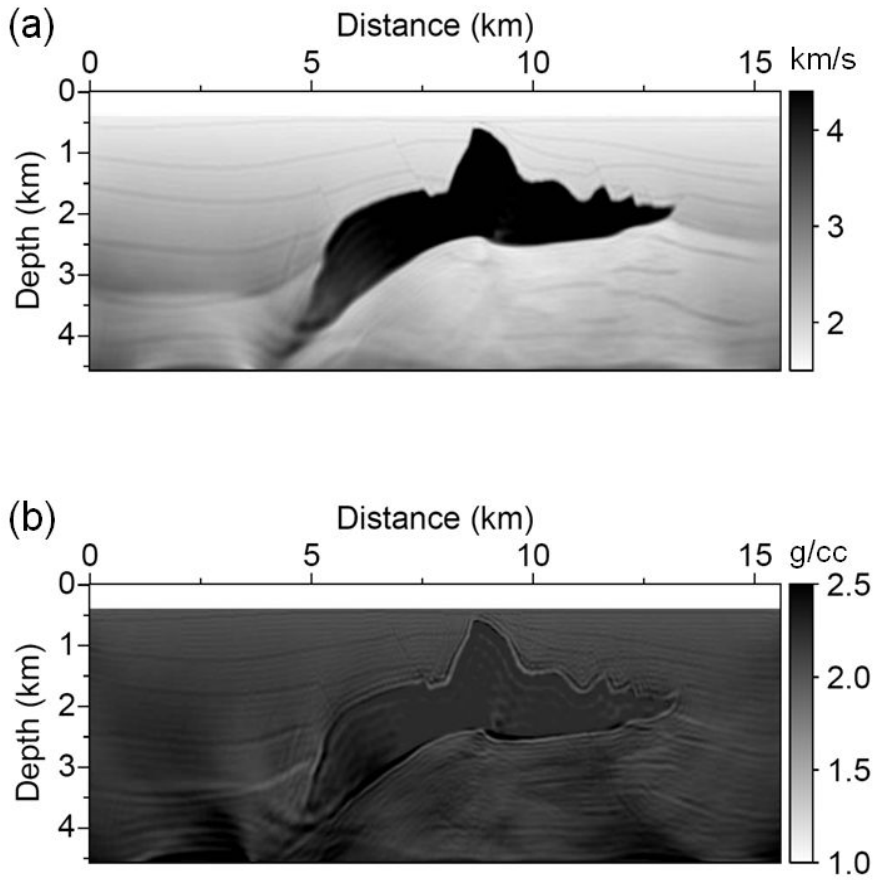


**Figure 4.2.3** Reconstructed models for (a) velocity and (b) density of SEG/EAGE salt model in the 2<sup>nd</sup> stage.

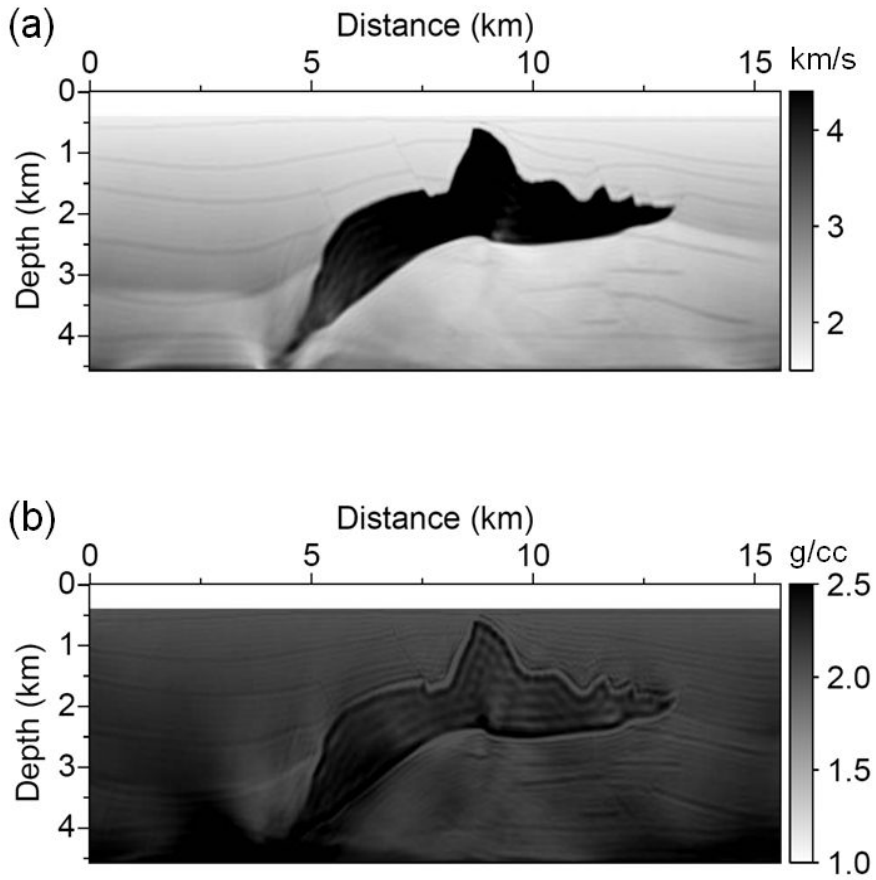


**Figure 4.2.4** Reconstructed models for (a) velocity and (b) density of SEG/EAGE salt model obtained by using the recently-announced hierarchical method (Prioux *et al.* 2013).

### 4.2.2 Marmousi-2 model

For an additional demonstration, velocity and density models of the Marmousi-2 model are used (Martin *et al.* 2006). Figure 4.2.5 shows the true models of velocity and density. The dimension of model is  $15.6 \text{ km} \times 4.2 \text{ km}$  with a grid interval of 20 m. To generate synthetically observed data, the first derivative of a Gaussian function with a maximum frequency of 15 Hz is used for a source signature; using 167 sources and recording over 6 seconds. Within the FWI process, the simultaneous-source that is phase-encoded randomly is employed for computational efficiency. All frequency bands are simultaneously used from 0.1667 to 15 Hz using an interval of 0.1667 Hz. The sources and receivers are located with an interval of 100 m and 20 m, respectively. Figure 4.2.6 shows initial models for velocity and density, respectively, which vary from 1.5 to 4.5  $\text{km s}^{-1}$  for velocity and from 2.0 to 2.4  $\text{g cm}^{-3}$  for density with depth. For the water layer, the depth and values are assumed to be already known.

First, the conventional FWI is applied to the Marmousi-2 model: velocity–density, bulk modulus–density, impedance–density and impedance–velocity parameterizations. Figure 4.2.7 shows the inversion results obtained by using conventional approaches. Velocities are reconstructed well for all parameterizations while the results of density show various aspects with poor outcomes. Hence, likewise, the hierarchical inversion strategy is applied. Figure 4.2.8 shows the inversion results obtained by the first stage of the hierarchical inversion with the pseudo-density of  $2 \text{ g cm}^{-3}$ . In here, the

velocity is well estimated with the pseudo-bulk modulus and pseudo-density and there is little deviation in the pseudo-bulk modulus from the true bulk modulus in Figure 4.2.9 because of the same reason as aforementioned. Figure 4.2.10 shows the FWI results for velocity and density after the two-stage hierarchical FWI. For a comparison, conventional hierarchical inversion results are generated as following the method by Prioux *et al.* (2013). Through this example, it can be noted that the conventional hierarchical inversion (by using the velocity–density parameterization for both stages) can give reasonable results for velocity and density when the geological features are similar for the both parameters. Figure 4.2.11 shows the conventional hierarchical inversion results for velocity and density. As it is expected, inverted density looks pretty good as the velocity does. Comparing with Figure 4.2.10 that are obtained by using the newer hierarchical inversion, the low value of density in salt structure at the bottom of left and right sides is not recovered in conventional approach. It is overestimated and only shows similar tendencies with the velocity model. However, in Figure 4.2.10, the hierarchical method suggested in this thesis gives very good agreements of density with the true one as well as accurate velocity model. Low value of the density at each side appears distinct from the previous results.

Consequently, although it seems like that the conventional hierarchical approach works well for multiparameter reconstruction, complex properties of the subsurface media may not be inverted accurately in fact. The method suggested in this study can be a solution of the multiparameter estimation that is in common use.

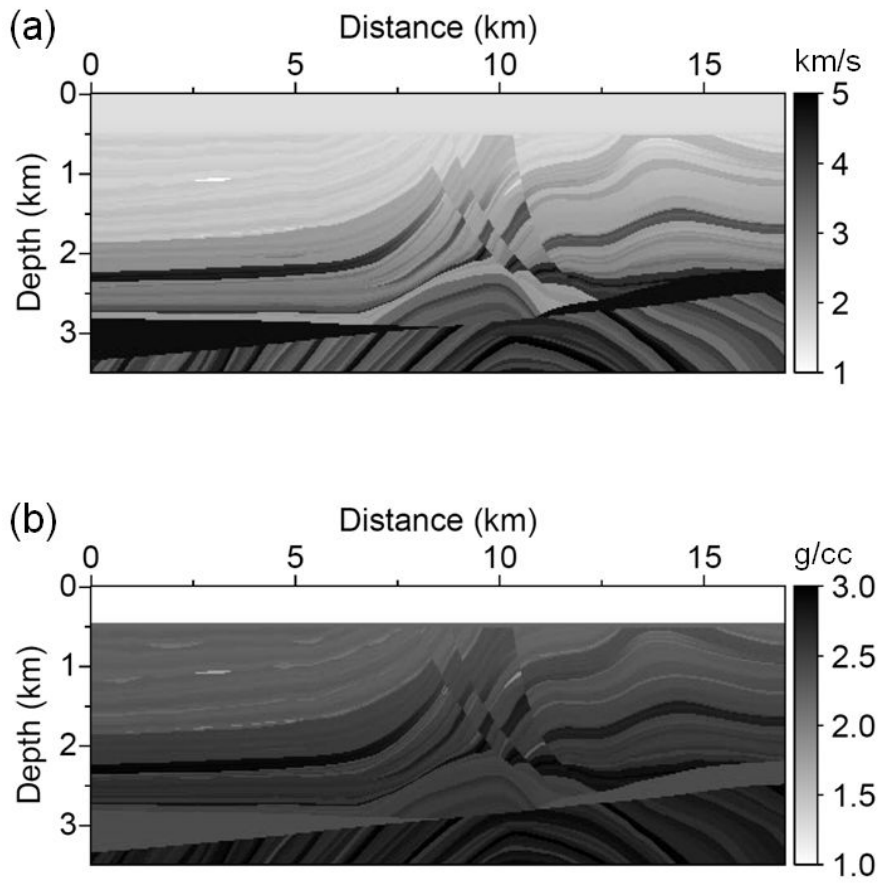


**Figure 4.2.5** True models for (a) velocity and (b) density of elastic Marmousi-2 model.

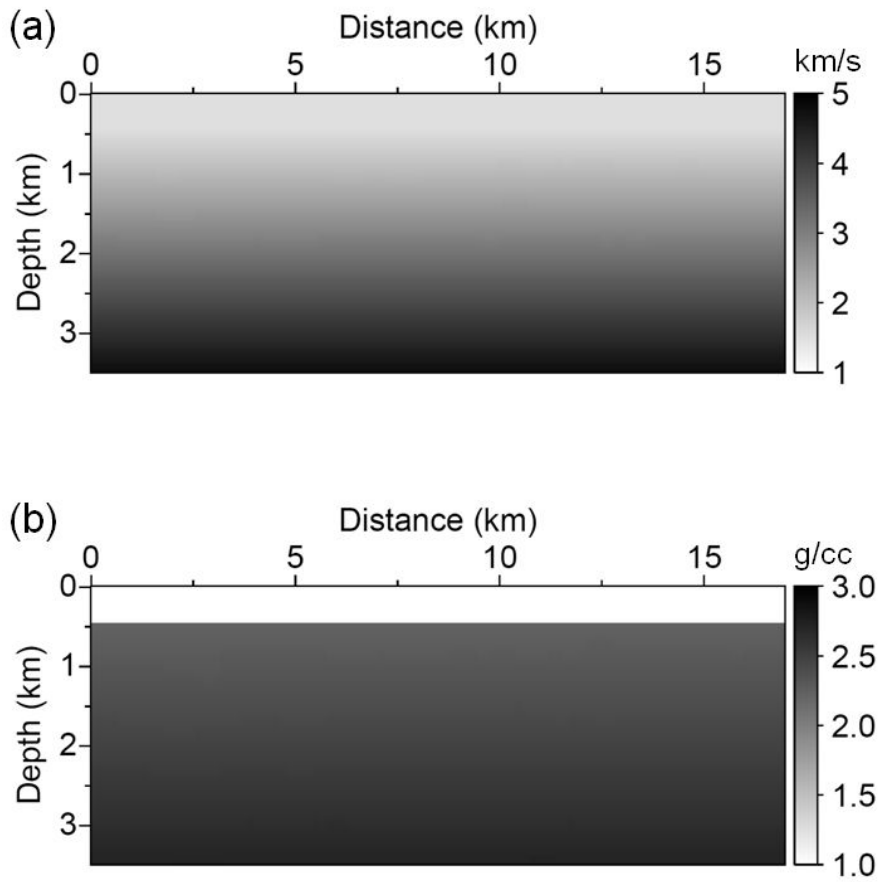


**Figure 4.2.6** Initial models for (a) velocity and (b) density of elastic Marmousi-2 model.

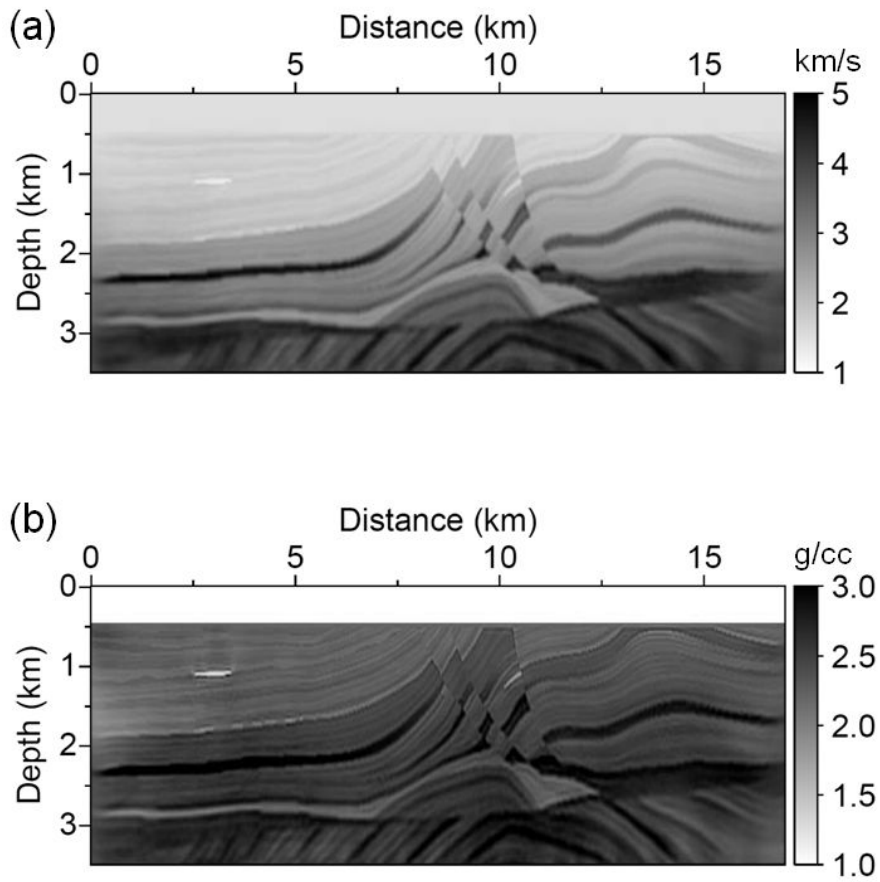


**Figure 4.2.7** Conventional FWI results for Initial models for velocity and density of elastic Marmousi-2 model obtained by using (a, b) velocity–density, (c, d) bulk modulus–density, (e, f) impedance–density and (g, h) impedance–velocity parameterizations, respectively. For each couple of figures, velocity is a figure expressed by unit of  $\text{km s}^{-1}$  (upper) and density is  $\text{g cm}^{-3}$  (lower).

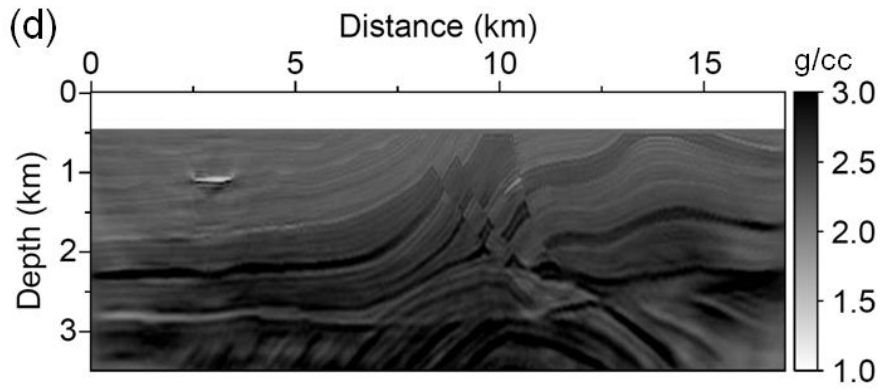
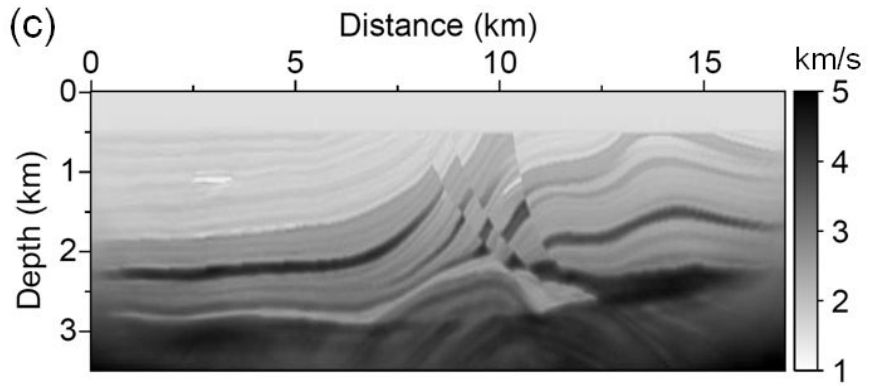


**Figure 4.2.7 (Continued)**

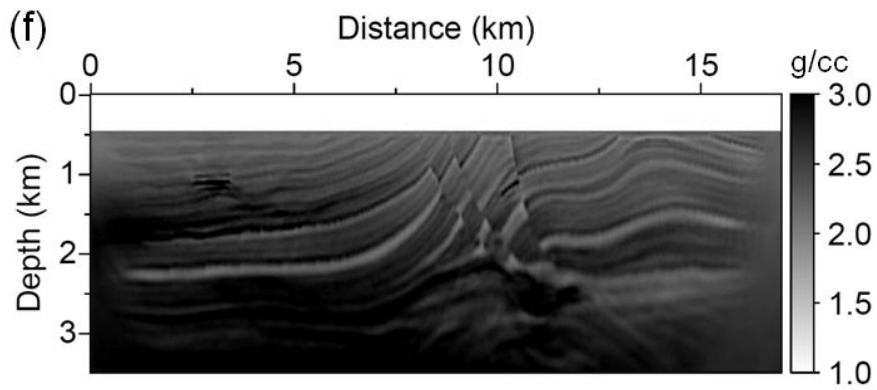
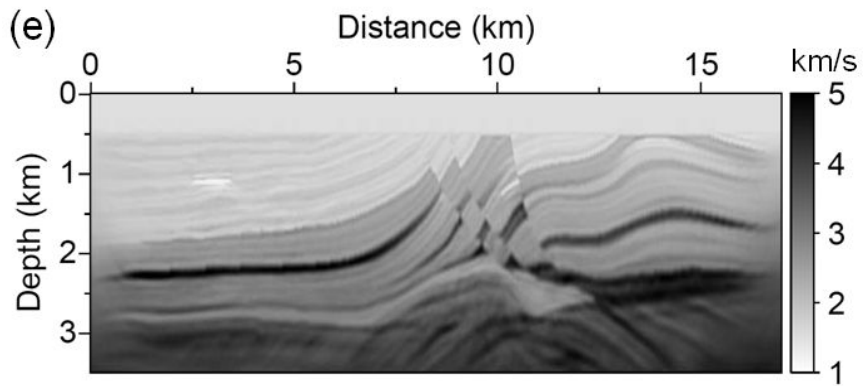


Figure 4.2.7 (Continued)

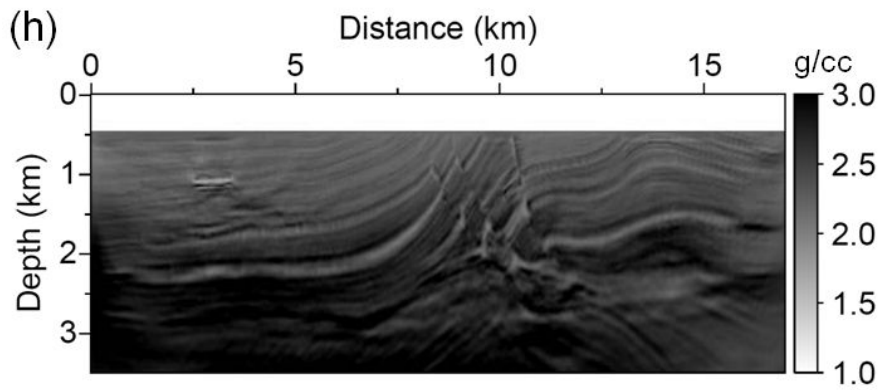
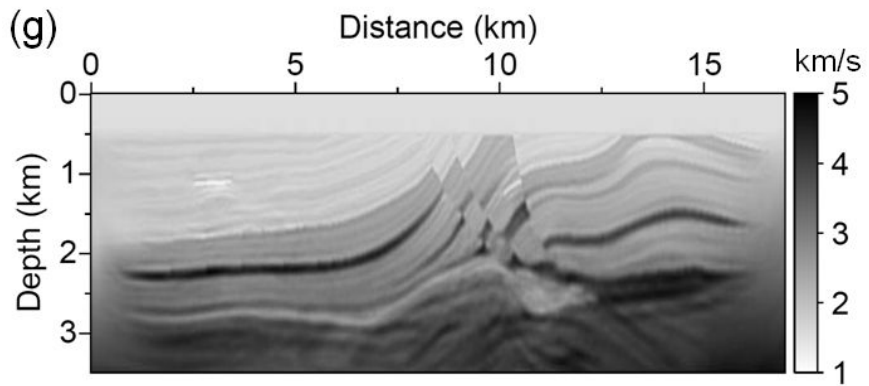
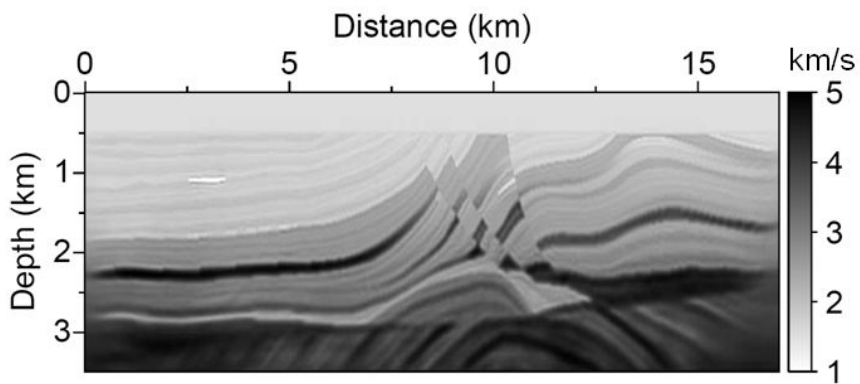
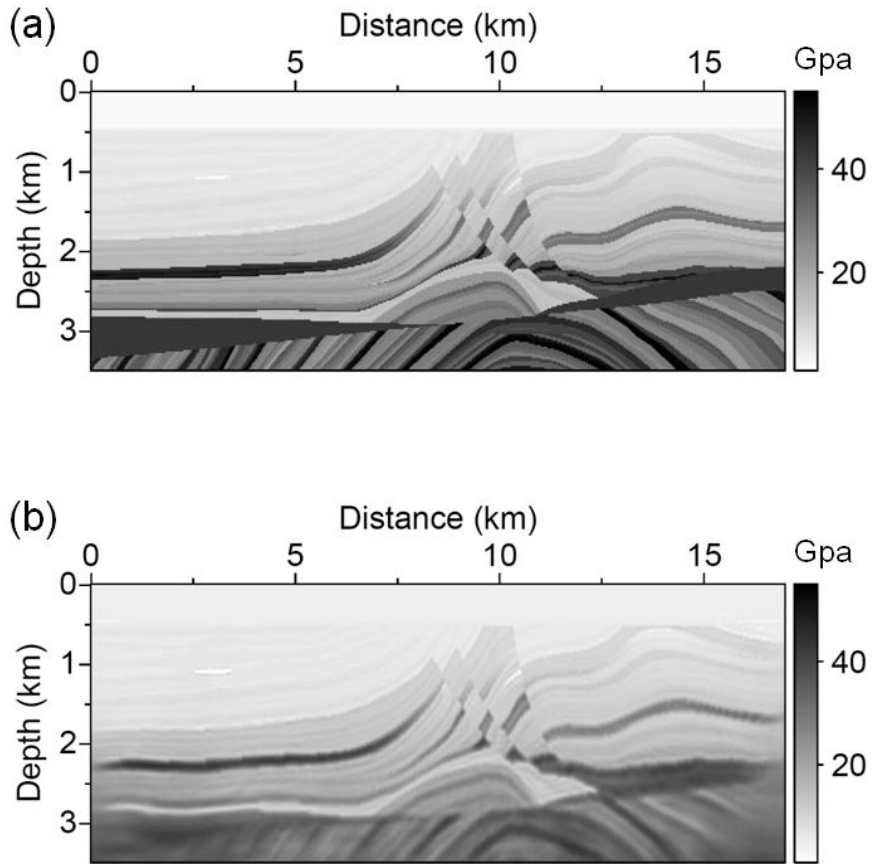


Figure 4.2.7 (Continued)



**Figure 4.2.8** Reconstructed velocity model for elastic Marmousi-2 model inverted at the 1<sup>st</sup> stage of the hierarchical inversion by using bulk modulus–density parameterization with pseudo-bulk modulus and fixed density as  $2 \text{ g cm}^{-3}$ .



**Figure 4.2.9** (a) The true and (b) inverted pseudo bulk modulus for elastic Marmousi-2 model. For an accurate comparison, the maximum and minimum values of the legend are fixed at the same level.

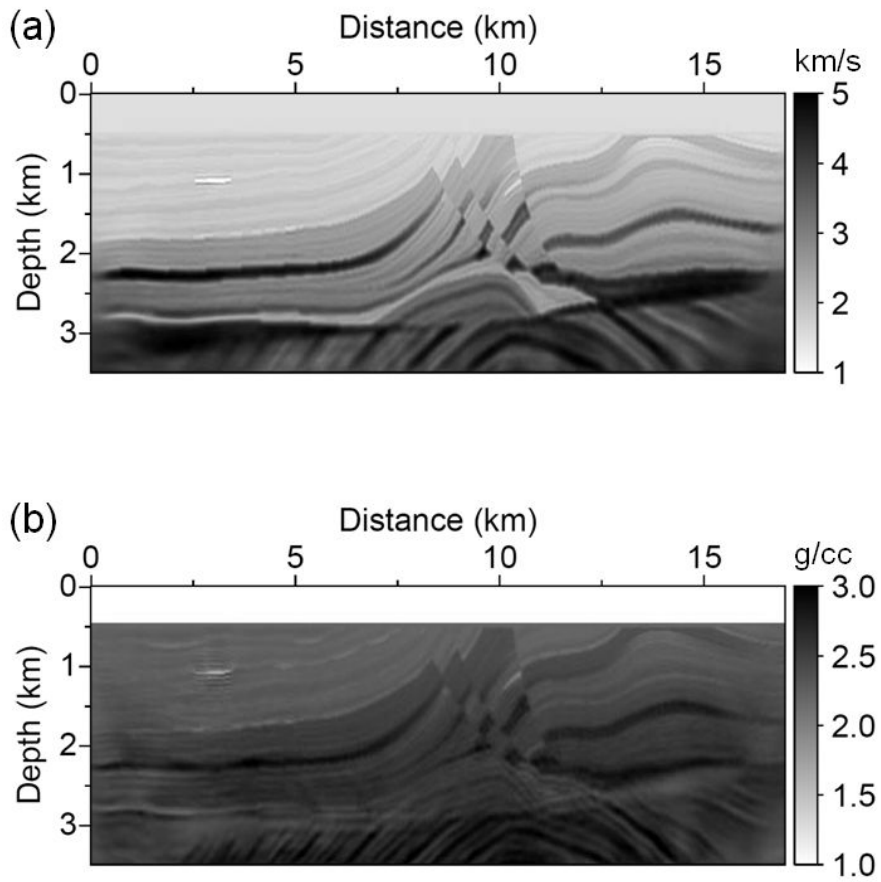


**Figure 4.2.10** Reconstructed models for (a) velocity and (b) density of elastic Marmousi-2 model in the 2<sup>nd</sup> stage.

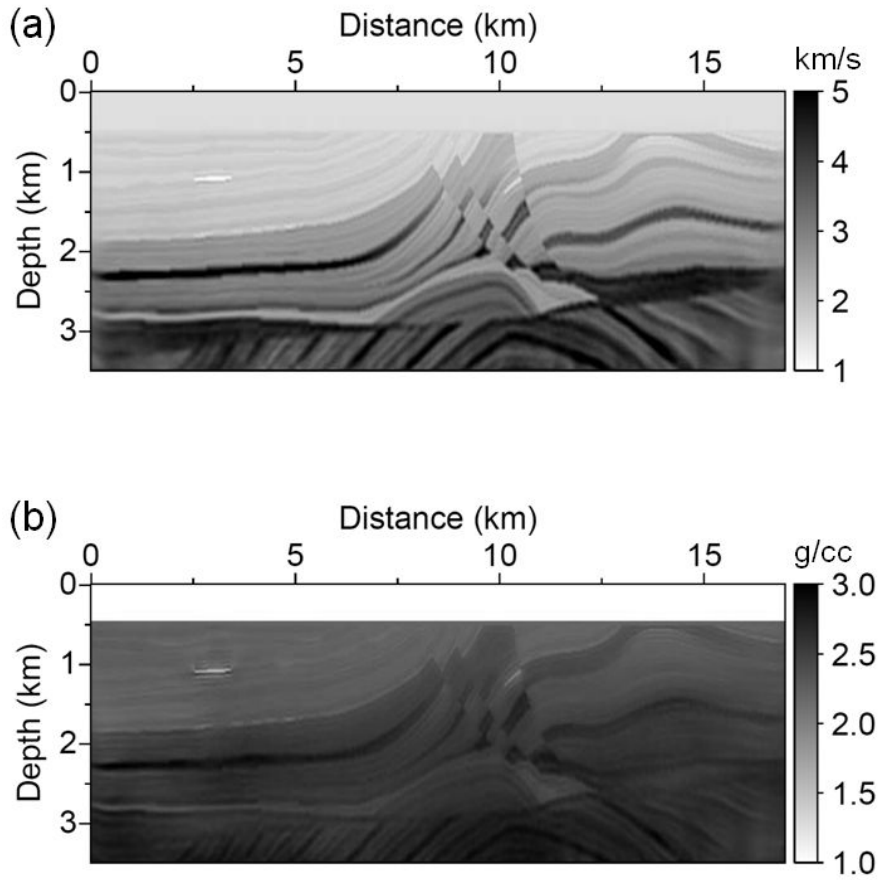


**Figure 4.2.11** Reconstructed models for (a) velocity and (b) density of elastic Marmousi-2 model obtained by using the recently-announced hierarchical method (Prioux *et al.* 2013).

## 4.3 Real data example

### 4.3.1 Gulf of Mexico data (ION/GXT)

To investigate the feasibility of the hierarchical FWI algorithm, real field data acquired in the Gulf of Mexico is applied. Only some parts of the original data are used. The numbers of shots and channels are 399 and 408, respectively; the intervals of the shots and channels are 50 m and 25 m, respectively. The maximum and minimum offsets are 0.137 km and 10.321 km, respectively. Total recording time is 12 s with a sampling interval of 4 ms. Figure 4.3.1 shows the representative shot gather and its frequency spectrum. As similar as a previous example Pluto 1.5 data set, because the real field data do not usually contain low-frequency information or only contain the noisy signals, it is difficult to reconstruct the subsurface structures without proper initial model and to avoid being trapped in local minima and cycle skipping. Thus, as in Figure 4.3.2, for the initial velocity model, Laplace-domain FWI result is provided from Ha *et al.* (2013). For an initial model of the density, the pseudo-density fixed at  $2 \text{ g cm}^{-3}$  is used for the first stage and the linearly increasing density ranging from  $1.92$  to  $2.46 \text{ g cm}^{-3}$  is employed.

Figure 4.3.3 shows the velocity model obtained at the first stage of the hierarchical inversion with the pseudo-density as  $2 \text{ g cm}^{-3}$  for whole model domain except for the water layer. Long wavelength structures have already been reconstructed by Laplace-domain FWI, so then the detailed structures are recovered by frequency-domain FWI with sharpening the smooth features. Now, FWI goes on next process of the multiparameter estimation that is the

main purpose of this study. By using the inverted velocity model at the first stage as an initial model for the second stage, impedance and velocity are inverted, and then the density is computed through dividing impedance by the velocity. Figure 4.3.4 shows the final results of multiparameter FWI. There are slight differences in the velocity model comparing with that at the first stage while the density model gives more detailed structures comparing with the initial model. Particularly, for the salt structure, it is observed that relatively low density compared to the surroundings. However, because of the narrow range of the radiation angle for the impedance, the density that is obtained by dividing impedance by the velocity reflects a short wavelength structures only. The salt structure is as not definitely reconstructed as the reconstructed velocity is. Nevertheless, it is carefully presented that the application of the inversion for the density to the real field data which have usually been applied to the synthetic example is comparably stable and successful. Figure 4.3.4c shows the total RMS error during the hierarchical inversion. RMS error decreases over two stages. Because the initial model has already been obtained by Laplace-domain FWI, error does not evidently decrease. Although the absolute numerical value compared to the first iteration, it is still questionable how much the decrease is confident.

Because the true velocity and density models are unknown in the case of real field data, there should be a criterion to verify whether the hierarchical FWI for multiparameter estimation is acceptable to the real field data or not. To do so, firstly, the observed and modeled wavefields are compared using the shot gathers. Figure 4.3.5 shows shot gathers obtained from the observed data

and modeling. The latter is generated by using the acoustic wave-propagation modeling based on the finite-element method. The velocity and density models, and the source wavelet obtained in the hierarchical FWI in this study is used for the modeling. Two shot gathers looks similar while the slight discrepancies are shown in some parts. For more detailed comparison, the time traces are extracted at an offset of 0.85 km. Figure 4.3.5c shows a comparison of the time traces obtained from original shot gather and the numerical modeling by using the velocity and pseudo-density at the first stage for the solid line and velocity and density at the second stage for the dashed line. Each trace shows good agreements in phase, because the FWI is generally able to retrieve the velocity information as well, which determine the travel time of the wave. However, there are some discrepancies among the amplitude of each signal. Considering the density affects to the amplitude of the wavefield, it is observed that the time trace at the second stage (dashed line) can compensate the amplitude well compared to the amplitude at the first stage (solid line).

To verify the amplitude compensation with another approach, the common midpoint (CMP) gather are generated and normal move out (NMO) correction is performed. Figure 4.3.6 show the number of the folds and the root-mean square (RMS) velocity, which is used for NMO correction. In general, when the intervals of the source and receiver are the same, the number of fold can be calculated by  $N_t/(2 \times \text{SPJ})$ ;  $N_t$  is the number of the traces and SPJ means shot point jump, which is the proportion of the interval of the source to that of receiver; In this case,  $N_t$  and SPJ are approximately 508 and

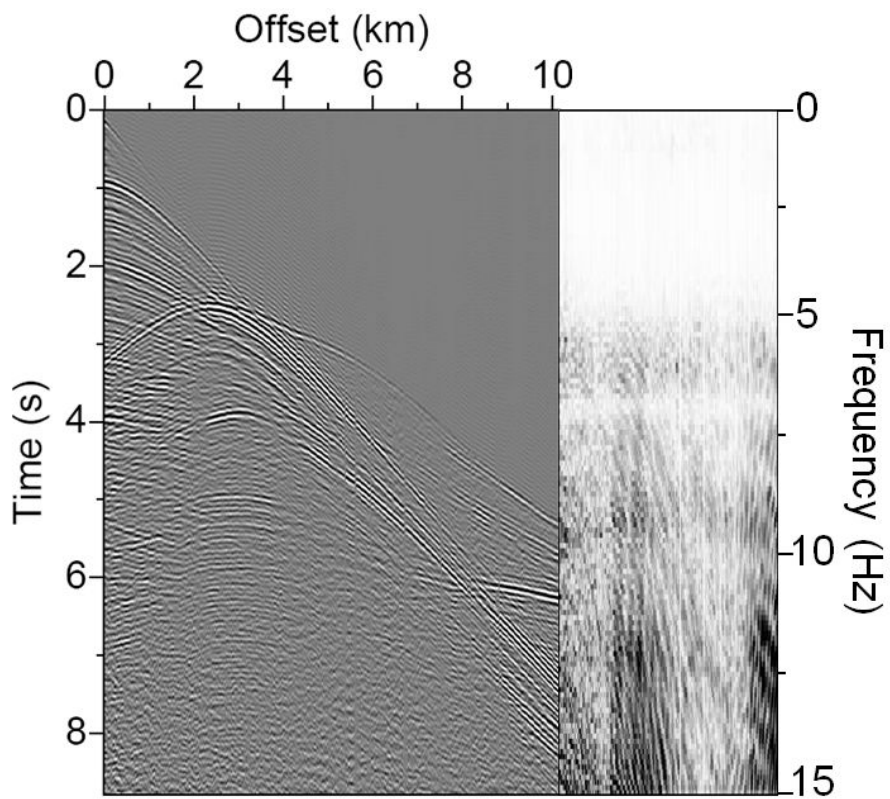
2.5. Although the intervals for the sources and receivers are changed for the case by cases in actual geometry, the maximum number of the fold is almost same as 100~101. RMS velocity is calculated by using the velocity model obtained in the second stage of the hierarchical FWI in Figure 4.3.4a. Figure 4.3.7 shows the example of the CMP gathers and its NMO corrected results. Curved events in the original CMP gathers are almost be flattened after the NMO correction. Now, stack section is generated and the dominant reflection events are observed in Figure 4.3.8; this indicates the top of the salt in this example. Using this dominant reflection, the amplitudes are compared for each case. Right panels in Figure 4.3.8a show the relative values of the stacked section for where the dominant reflection is located. Although the stacked sections deviate from the original one, because the CMP gathers obtained by using the modeling results for the first and second stage only reflect the characteristics of the acoustic wave equation, they show almost similar tendencies with the original one. Figure 4.3.8b shows the time traces for the stacked section for several CMPs. It is not as good as it is expected, but the tendencies of the amplitudes of the modeled data shows quite good agreements for the dominant reflection. In addition, it is noted that the stacked CMP obtained by using the results of the second stage can compensates the amplitudes better considering the density variation in the FWI.

Figure 4.3.9 shows the results of the reverse-time migration (RTM). Adopting the concept of the multiparameter, several choices occur to consider. In the conventional way, using the imaging condition suggested by Claebout (1985) that is zero-lag cross-correlation of the forwardly propagated waves

and backwardly propagated waves has provided the migration image. On the other hand, using the back-propagation technique, RTM can be performed with the back-propagation of the observed data rather than the residual in FWI algorithm (Shin et al. 2003; Chavent and Plessix, 1999). In this example, the latter method is employed to generate the RTM images to follow the purpose of multiparameter inversion, because the RTM results depend on which parameterization is used for computation of the virtual source. However, considering the four kinds of parameterizations aforementioned, there are some ambiguities which parameter would be imaged. Hence, to avoid this ambiguity, the velocity–density parameterization is used for RTM representatively. Figure 4.3.9 shows a RTM image obtained by using the inverted velocity and density in the second stage of the hierarchical FWI. Figures 4.3.9a and 4.3.9b are generated by using the virtual source of the velocity and density, respectively. In Figure 4.3.9a, most of the structures are shown along with the vertically rising salt due to its greater buoyancy compared to the surroundings. However, the continuity of the salt structure and the structures around the salt are distorted and it may drive wrong way to estimate the location of the targeted area. In Figure 4.3.9b, RTM image obtained by using the virtual source of density shows more clear image for the top and the inner side of the salt structure. Although it seems like that only the top of salt is emphasized in this case, this is because the radiation pattern of the density in this parameterization is concentrated on the narrow angle; this indicates that the migration reflects the information from the short offset and short wavelength structures. If the parameterization that considers the long

wavelength and far offset information can treat different aspect of the RTM. Figures 4.3.9c and 4.3.9d show the RTM images obtained by the impedance–density parameterization. As it is expected, because the radiation pattern of the velocity is concentrated on the far offset range and long wavelength structure, Figure 4.3.9c shows smooth and huge structures. The impedance shows the image as similar as it of density in Figure 4.3.9b, because of their radiation pattern, which are the same. Thus, using the multiparameter scheme in RTM, the comprehensive analyses would be possible and more accurate interpretation can be provided. Additionally, slightly irrelevant to the multiparameter estimation, angle domain common image gather (AGCIG) (Sava and Fomel, 2003) is computed to verify whether the velocity model is estimated well or not. Figure 4.3.10 shows the ADCIG extracted at offsets of 3, 5, 7, 9 and 11 km from the left side for Figures 4.3.9a and 4.3.9b. For each panel, flattened events indicate that the velocity and density models are estimated in right direction in our algorithm.

In conclusion, the hierarchical FWI for the estimation of the velocity and density can achieve its goal, and estimating the density as well as the velocity in acoustic FWI can help the interpretation of the seismic data processing in a various perspective.



**Figure 4.3.1** A representative shot gather at a distance of 10.45 km from the left side of the model and its frequency spectrum.

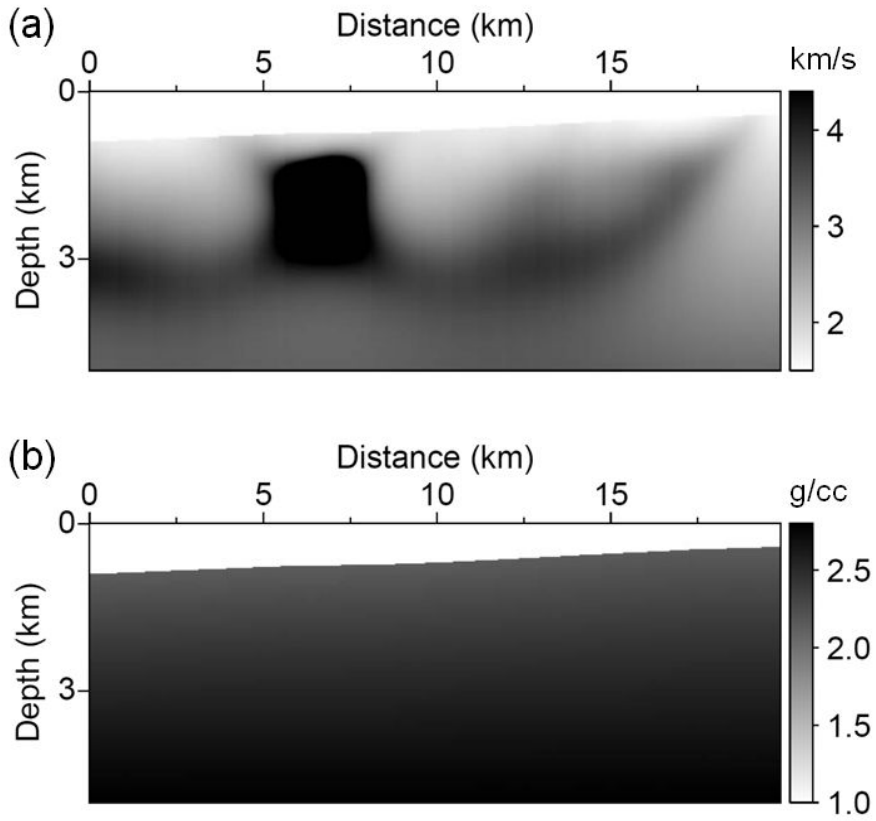


**Figure 4.3.2** Initial models for (a) P-wave velocity and (b) density of Gulf of Mexico data set.

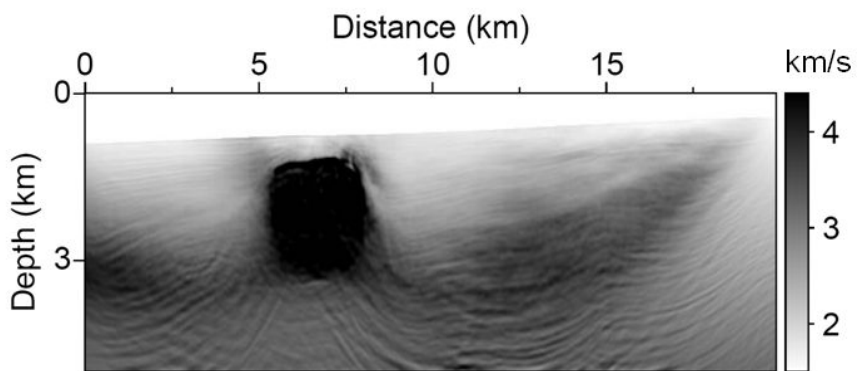


**Figure 4.3.3** Reconstructed model for P-wave velocity at the first stage of the hierarchical FWI for Gulf of Mexico data set. The pseudo-density is fixed at a constant as  $2 \text{ g cm}^{-3}$  except for the water layer.

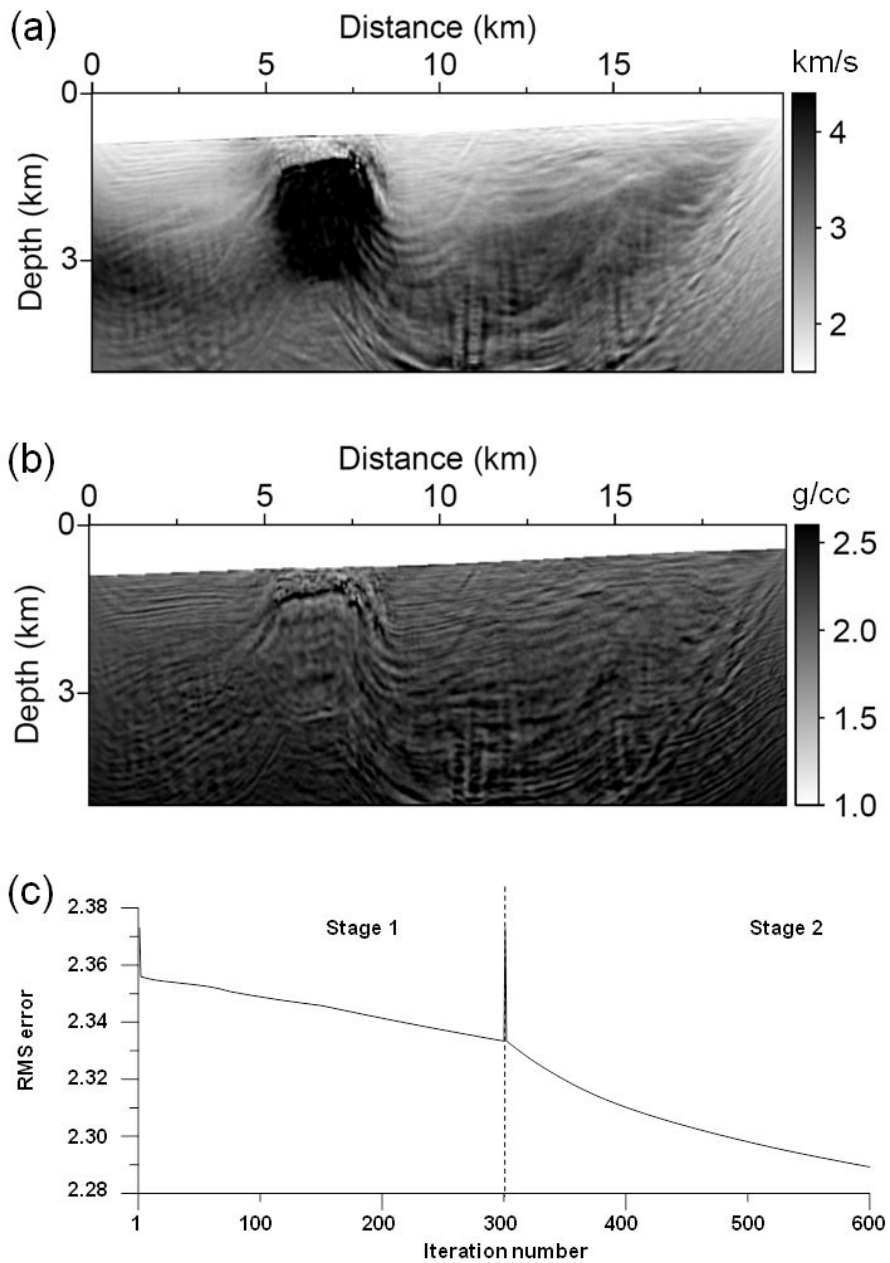


**Figure 4.3.4** Reconstructed models for (a)  $P$ -wave velocity and (b) density at the second stage of the hierarchical FWI for Gulf of Mexico data set. RMS errors for the 1<sup>st</sup> and 2<sup>nd</sup> stage are plotted in (c).

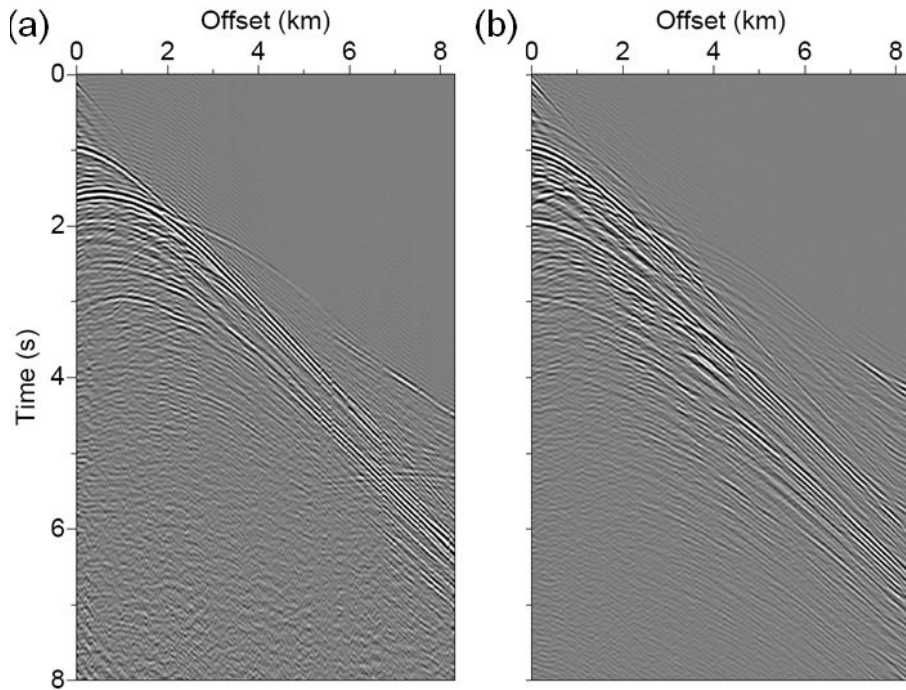


**Figure 4.3.5** Examples of the (a) original shot gather and (b) modeled shot gather obtained by using the inverted velocity and density at the second stage. Time traces extracted at an offset of (c) 0.5 km and (d) 1.18 km. The dashed grey line indicates the time trace extracted from the original shot gather. The light grey dashed line and black solid line represent the time traces extracted from the modeled shot gather obtained by using the inverted velocity and pseudo-density at the first stage and the inverted velocity and density at the second stage, respectively.

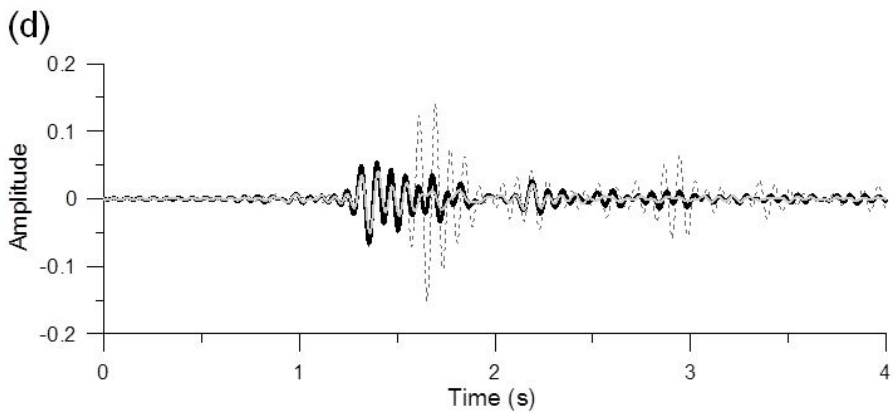
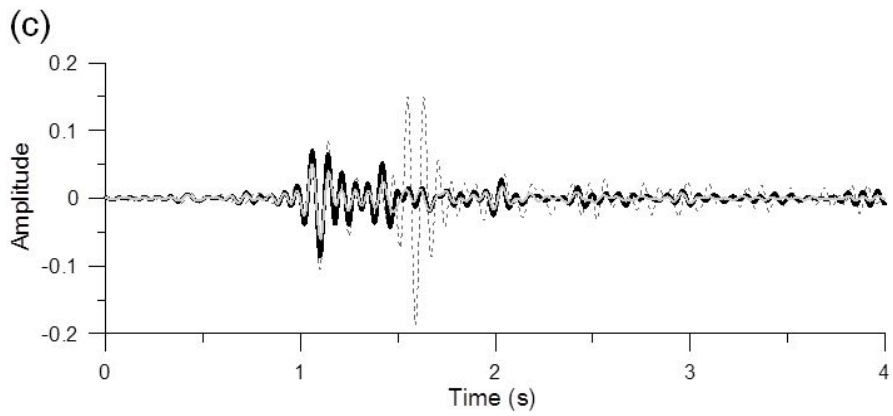
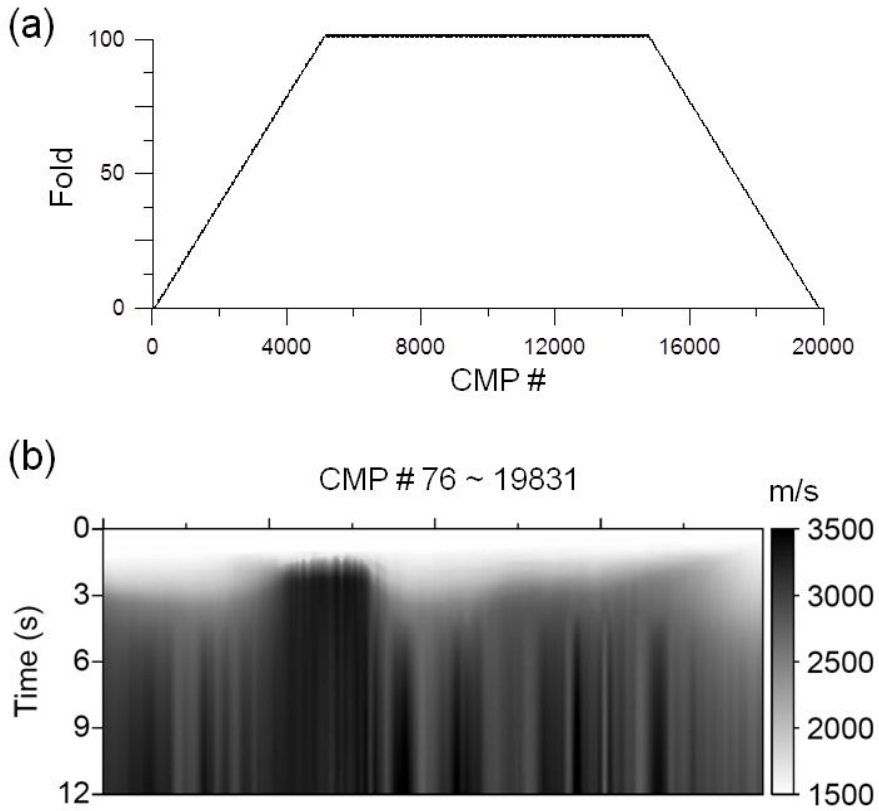
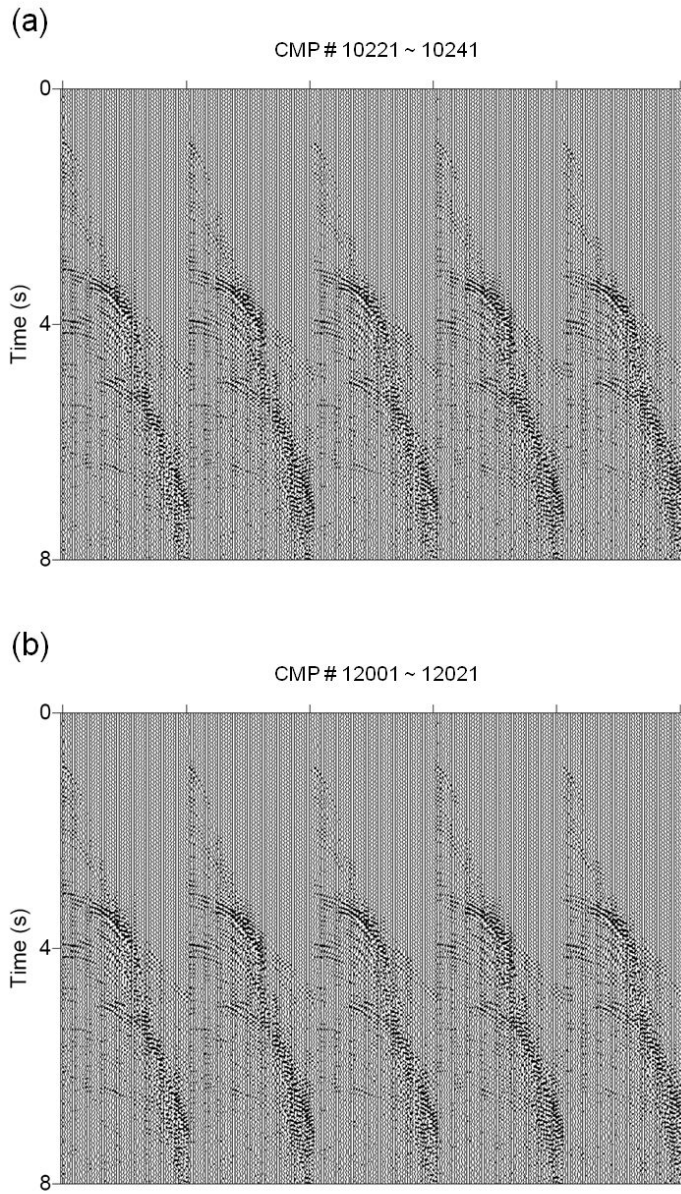


Figure 4.3.5 (continued)



**Figure 4.3.6** (a) The number of folds for each CMP. Maximum fold is 102. (b) RMS velocity model computed by the velocity model obtained in the second stage of the hierarchical FWI. SU command VELCONV is used for the conversion.



**Figure 4.3.7** Representative CMP gathers for the CMP number (a) from 10221 to 10241 and (b) from 12001 to 12021. And its NMO corrected CMP gathers are shown in (c) and (d).

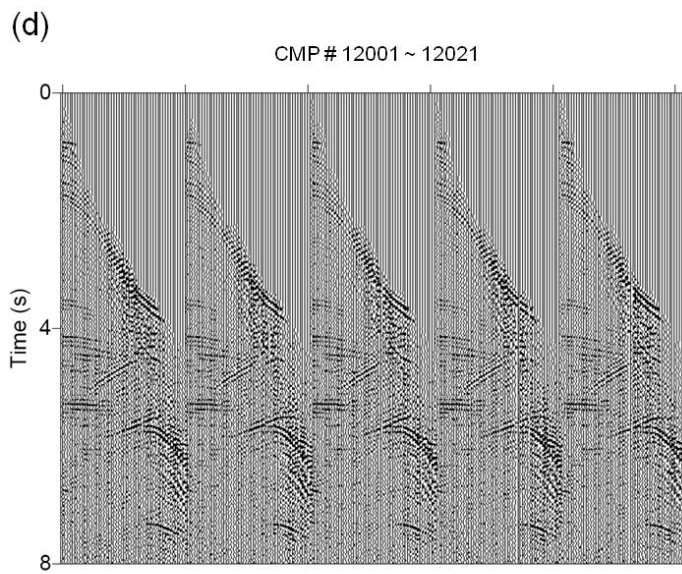
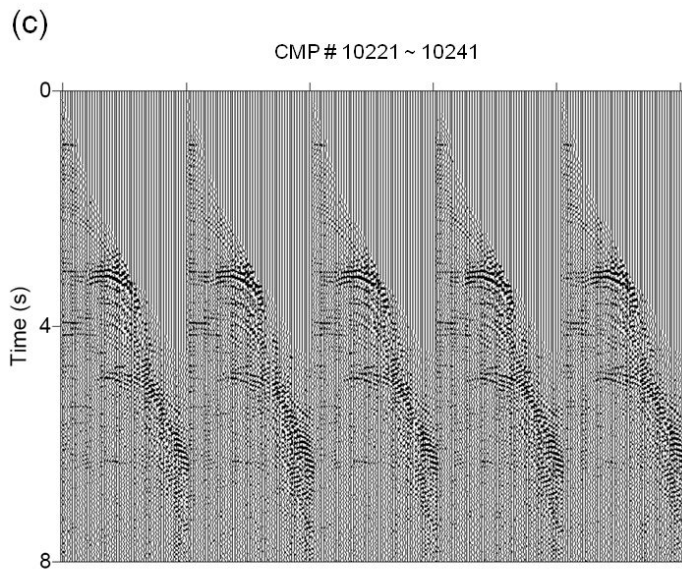
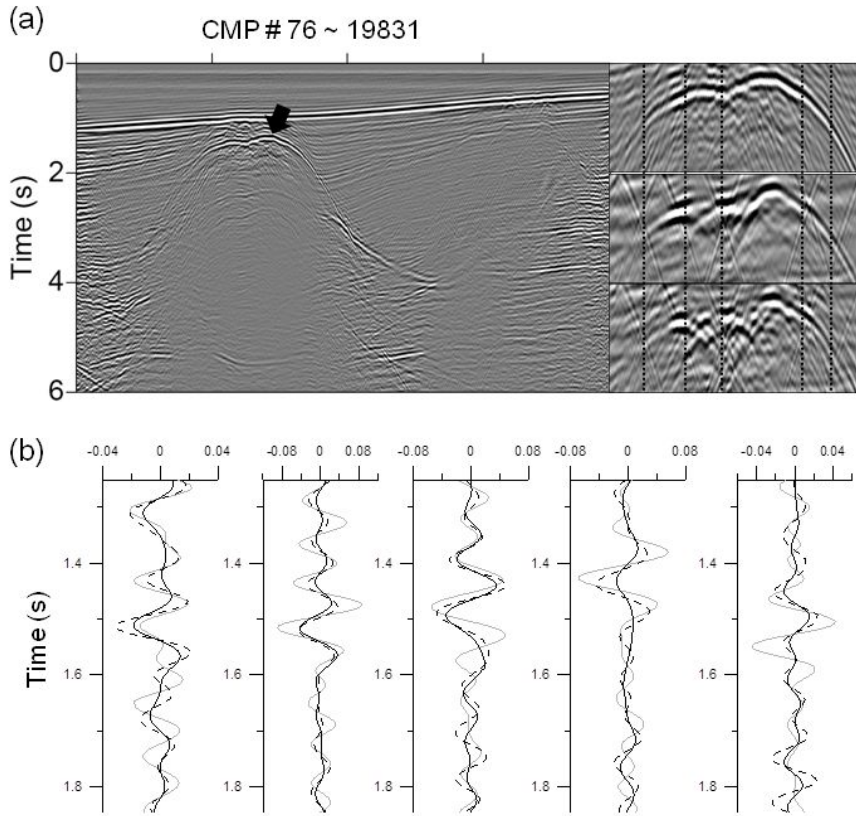
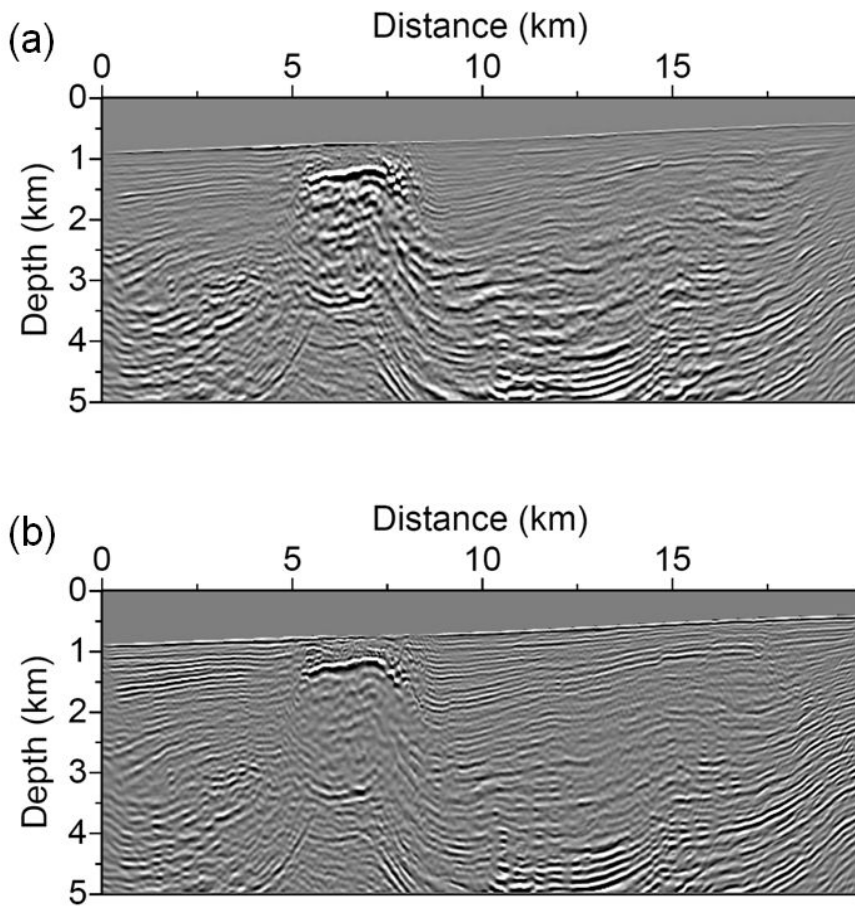


Figure 4.3.7 (Continued)



**Figure 4.3.8** (a) Stacked section of the CMP gathers for the original data set. The Black arrow indicates the dominant reflection chosen for the comparison. The three panels at the right-hand side are the comparison of the dominant reflection for the original data set (top), stacked sections using the modeled data obtained in the first stage (center) and the second stage (bottom) in the relative value. The black dotted lines indicate the location where the time traces are extracted. (b) Amplitudes for each stacked section in (a). The grey solid line represents the profile of the original data set, and black solid and dashed lines denote that of the first and the second stages, respectively.



**Figure 4.3.9** RTM images obtained by the back-propagation of the virtual source of (a) velocity and (b) density in velocity–density parameterization, respectively, and (c) velocity and (d) impedance in impedance–velocity parameterization, respectively..

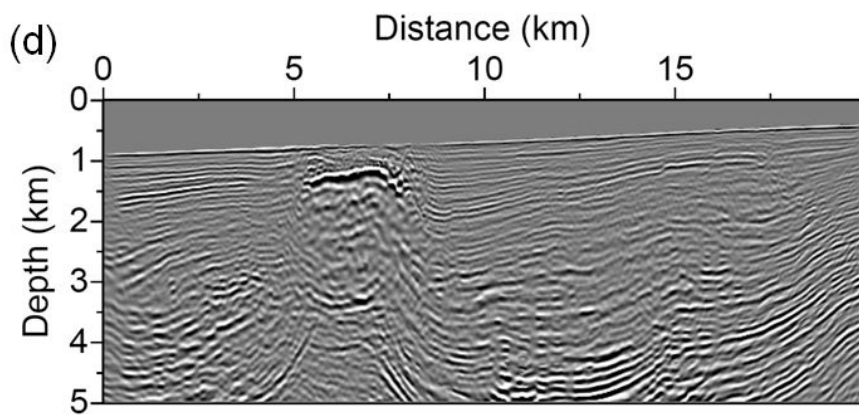
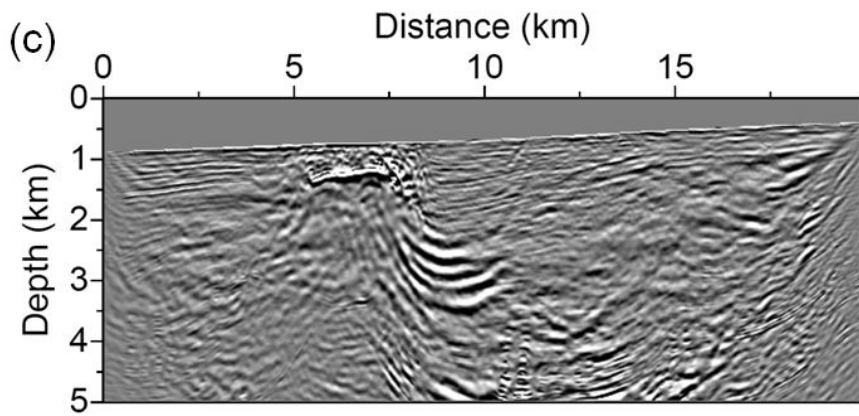
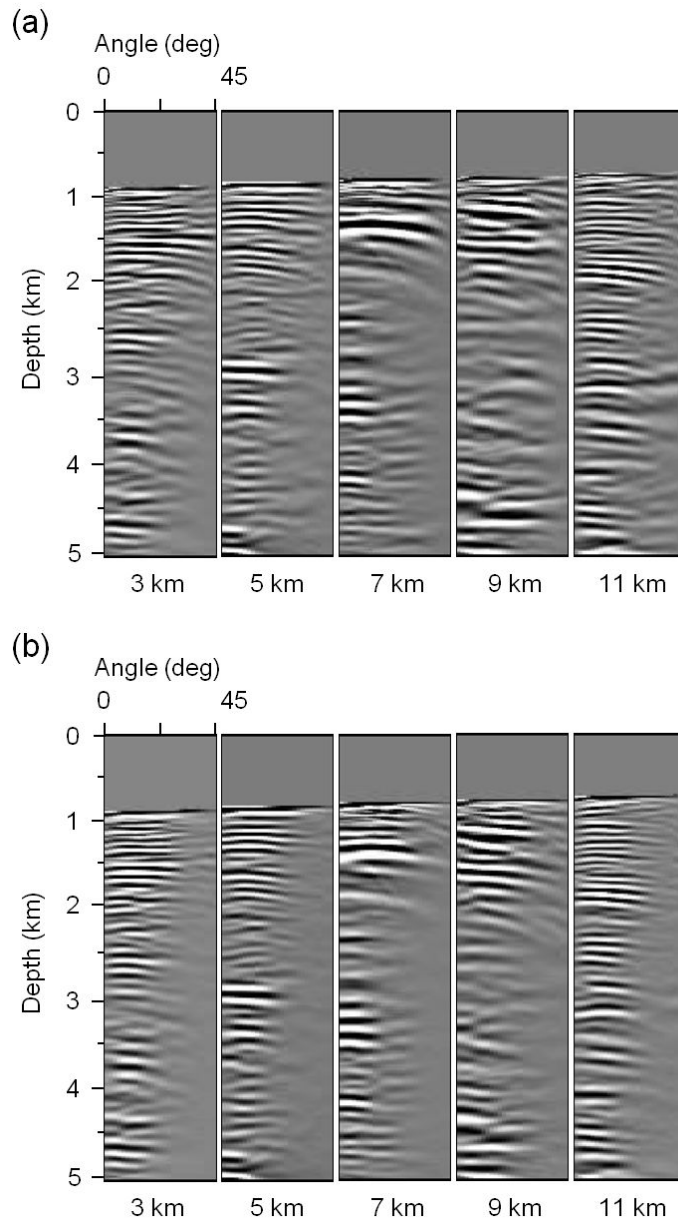


Figure 4.3.9 (Continued)



**Figure 4.3.10** ADCIGs for (a) velocity and (b) density at a distance of 3, 5, 7, 9 and 11 km from the left side of the model. The angle is ranging from  $0^\circ$  to  $45^\circ$  in each panel.

## Chapter 5. Conclusions

The early stage of acoustic FWI is used to retrieve only velocity based on the mono-parametric wave equation that is parameterized by the velocity. As the needs for more reliable information on subsurface structures has increased and the targeted structures become more complex, the paradigm of FWI has moved to multiparameter estimation. The attributes of various parameters are different to each other so that multiparameter inversion can give more precise and sufficient information of the subsurface properties and structure. Recently, there have been attempts to reconstruct the density, anisotropic parameters and attenuation through the acoustic FWI. To obtain reliable information for multiparameter, there have been numerous studies about parameterization, hierarchical approach and so on. Among them, in this thesis, various types of parameterization and the hierarchical approach for the multiparameter inversion is proposed.

In this study, a two-stage inversion strategy is suggested, which devote to improve the inversion results of the velocity and density by analyzing the characteristics of four parameterizations: velocity–density, bulk modulus–density, impedance–density and impedance–velocity. Investigating the radiation patterns and the mathematical formulae of virtual sources for the four parameterizations suggested the inter-dependency and trade-offs between individual parameters for each parameterization. Through these analyses, bulk modulus–density parameterization was chosen for the first stage of the

hierarchical inversion. In this stage, pseudo-bulk modulus was inverted rather than the original one with the pseudo-density which is fixed at an arbitrary constant. Comparing with the results obtained by the velocity–density and impedance–density by using the pseudo-density, it was noted that this concept is valid much more in the bulk modulus–density parameterization. Using the velocity model obtained by taking square root to the pseudo-bulk modulus dividing by the pseudo-density at the first stage, the density was considered in the second stage. In the second stage, impedance–velocity parameterization was used for density estimation. The impedance and velocity were inverted directly and the density was obtained from the relationship between velocity and impedance.

The algorithm was demonstrated to the synthetic and real field data; SEG/EAGE salt model, Marmouisi-2 model, Pluto 1.5 data set and the field data gathered from the Gulf of Mexico. Synthetic examples showed that the both velocity and density can be reconstructed through FWI using an adequate combination of two parameterizations. For the real field data, although it is difficult to evaluate the applicability and accuracy of the results, various proofs supported the rationale of the multiparameter estimation and the validity of the FWI results. Although the result of the density is not as good as in the case of the synthetic tests, the multiparameter estimation using hierarchical acoustic FWI can help the reasonable interpretation of the subsurface media and be a promising method in the FWI field.

Additionally, there are several issues which can be discussed and be a further study. The first one is, there is no clear criterion to assure the value of

the pseudo-density. As aforementioned, although the moderate value of a constant density can give a reasonable result for the reconstructed velocity, the value which is moderate is very ambiguous. Finding the pseudo-density not empirically but theoretically can help the improvement of the hierarchical FWI. The second one is the lack of low-frequency component. Considering the Pluto 1.5 data set and Gulf of Mexico dataset, FWI used the results obtained in the Laplace domain as initial models, because there are few or no information in the low-frequency component in the observed data. This is also the weakest point of the FWI. Local minima and cycle skipping problems have often happened and spoiled the FWI. Hence, the building appropriate initial model is a big issue to be solved. The third one is the use of impedance–velocity parameterization. In section 3.1.2, I mentioned how this parameterization behaves with respect to the offset. However, because it was based on not a few assumptions, it would be good for evaluation of the use for impedance–velocity parameterization in practice. The last one is the comprehensive interpretation with the elastic FWI. There have already been numerous studies about the FWI for the elastic and acoustic-elastic coupled media, which can consider the shear wave velocity in the subsurface media. It is not easy to apply the acoustic FWI to the elastic media due to the elastic waves such as the Rayleigh and mode-converted waves; however, it can be effectively applied to the marine data. Thus, FWI and RTM would be improved and provide well-estimated results when the multiplicative approaches are applied.

In summary, there may be topics to solve and adjust so far, the

hierarchical inversion for the multiparameter estimation suggested in this study provides very fruitful analyses and possibility of the FWI for the density.

## Bibliography

- Aki, K. and P. G. Richard, 1980, Quantitative seismology, University Science Books, Sausalito, California.
- Aminzadeh, F., N. Burkhard, L. Nicoletis, F. Rocca, and K. Wyatt, 1994, SEG/EAGE 3-D modeling project: 2<sup>nd</sup> update, *The Leading Edge*, **13**, 949-952.
- Ben-Hadj-Ali, H., S. Operto, and J. Virieux, 2011, An efficient frequency-domain full waveform inversion method using simultaneous encoded sources, *Geophysics*, **76**, R109-R124.
- Berenger, J. P., 1994, A perfectly matched layer for the absorption of electromagnetic waves, *Journal of computational physics*, **114**, 185-200.
- Brenders, A., R. Pratt, S. Charles, 2009, Waveform tomography of 2-d seismic data in the Canadian foothills-data preconditioning by exponential time-damping, 71<sup>st</sup> EAGE conference & exhibition, U041.
- Brossier, R., S. Operto, and J. Virieux, 2009, Seismic imaging of complex onshore structures by 2D elastic frequency-domain full-waveform inversion. *Geophysics*, **74**, WCC105-WCC118.
- Bunks, C., F. M. Saleck, S. Zaleski, and G. Chavent, 1995, Multiscale seismic waveform inversion. *Geophysics*, **60**, 1457-1473.
- Chavent, G. and R.-E. Plessix, 1999, An optimal true-amplitude least-squares prestack depth-migration operator, *Geophysics*, **64**, 508-515.
- Choi, Y., D.-J. Min, and C. Shin, 2008a, Two-dimensional waveform inversion of multi-component data in acoustic-elastic coupled media. *Geophysical Prospecting*, **56**, 863-881.
- Choi, Y., D.-J. Min and C. Shin, 2008b, Two-dimensional waveform inversion of multi-component data in acoustic-elastic coupled media, *Geophysical Prospecting*, **56**, 863-881.
- Choi, Y. and T. Alkhalifah, 2012, Application of multi-source waveform inversion to marine streamer data using the global correlation norm. *Geophysical Prospecting*, **60**, 748-758.

- Cohen, G., 2002, High-order numerical methods for transient wave equations. Springer.
- Clayton, R. and B. Engquist, 1977, Absorbing boundary conditions for acoustic and elastic wave equations, *Bulletin of the seismological society of America*, **67**, 1529-1540.
- Claebout, J. F., 1985, *Imaging the earth's interior*, Blackwell Scientific Publication.
- Forgues, E. and F. Lambaré, 1997, Parameterization study for acoustic and elastic ray+Born inversion, *Journal of seismic exploration*, **6**, 253-277.
- Gauthier, O., J. Virieux, and A. Tarantola, 1986, Two-dimensional nonlinear inversion of seismic waveforms. Numerical results: *Geophysics*, **51**, 1387-1403.
- Gardner, G. H. F., L. W. Gardner, and A. R. Gregory, 1974, Formation velocity and density - the diagnostic basis for stratigraphic traps. *Geophysics*, **39**, 770-780.
- Gholami, Y., R. Brossier, V. Prieux, S. Operto, A. Ribodetti, and J. Virieux, 2013a, Which parameterization is suitable for acoustic vertical transverse isotropic full waveform inversion? Part 1: Sensitivity and trade-off analysis. *Geophysics*, **78**, R81-R105.
- Gholami, Y., R. Brossier, S. Operto, V. Prieux, A. Ribodetti, and J. Virieux, 2013b, Which parameterization is suitable for acoustic vertical transverse isotropic full waveform inversion? Part 2: Synthetic and real data case studies from Valhall. *Geophysics*, **78**, R107-R124.
- Guittou, A., G. Ayeni, and E. Diaz, 2012, Constrained full-waveform inversion by model reparameterization, *Geophysics*, **77**, R117-R127.
- Ha, W., S. Pyun, J. Yoo and C. Shin, 2010, Acoustic full waveform inversion of synthetic land and marine data in the Laplace domain, *Geophysical prospecting*, **58**, 1033-1047.
- Ha, W. and C. Shin, 2012, Laplace-domain full waveform inversion of seismic data lacking low-frequency information, *Geophysics*, **77**, R199-R206.
- Higdon, R. L., 1986. Absorbing boundary conditions for difference approximations to the multidimensional wave equation, *Mathematics of computation*, **47**, 437-459.
- House, L., S. Larsen, and J. B. Bednar, 2000, 3-D elastic numerical modeling of a

- complex salt structure, 70<sup>th</sup> Annual International Meeting, SEG, Expanded abstracts, 2201-2204.
- Huang, Y. and G. T. Schuster, 2012, Multisource least-squares migration of marine streamer and land data with frequency-division encoding, *Geophysical prospecting*, **60**, 663-680.
- Ikelle, L. T., 1996, Linearized inversion of 3D multioffset data: Background reconstruction and AVO inversion, *Geophysical Journal International*, **123**, 507-528.
- Jeong, W., D.-J. Min, G. Lee, and H.-Y. Lee, 2011, 2D frequency-domain elastic full waveform inversion using finite-element method for VTI media. 81st Annual International Meeting, SEG, Expanded Abstracts, 2654-2658.
- Jeong, W., H.-Y. Lee, and D.-J. Min, 2012, Full waveform inversion strategy for density in the frequency domain. *Geophysical Journal International*, **188**, 1221-1242.
- Jeong, W. and D.-J. Min, 2012, Application of acoustic full waveform inversion for density estimation. 82nd Annual International Meeting, SEG, Expanded Abstracts, 1-5.
- Jeong, W., S. Pyun, W. Son, and D.-J. Min, 2013, A numerical study of simultaneous-source full waveform inversion with  $l_1$ -norm. *Geophysical Journal International*, **194**, 1727-1737.
- Kim, Y., H. Cho, D.-J. Min, and C. Shin, 2011, Comparison of frequency-selection strategies for 2D frequency-domain acoustic waveform inversion. *Pure and applied geophysics*, **168**, 1715-1727.
- Köhn, D., D. De Nil, A. Kurzman, A. Przebindowska and T. Bohlen, 2012, On the influence of model parameterization in elastic full waveform tomography. *Geophysical Journal International*, **191**, 325-345.
- Kolb, P., F. Collino, and P. Lailly, 1986, Prestack inversion of 1-D medium. *Proceedings of the IEEE*, 498-508.
- Krebs, J., J. Anderson, D. Hinkley, R. Neelamani, S. Lee, A. Baumstein, and M. D. Lacasse, 2009, Fast full-wavefield seismic inversion using encoded sources.

- Geophysics, **74**, WCC177-WCC188.
- Lailly, P., 1983, The seismic inverse problem as a sequence of before stack migrations. Conference on inverse scattering, Theory and application: Society for Industrial and Applied Mathematics, Expanded abstracts, 206-220.
- Lee, H.-Y., J.-M. Koo, D.-J. Min, B.-D. Kwon, and H.-S. Yoo, 2010, Frequency-domain elastic full waveform inversion for VTI media. *Geophysical Journal International*, **183**, 884-904.
- Marfurt, K. J., 1984, Accuracy of finite-difference and finite-element modeling of the scalar and elastic wave equations. *Geophysics*, **49**, 533-549.
- Martin, G. S., R. Wiley, and K. J. Marfurt, 2006, Marmousi-2: An elastic upgrade for Marmousi, *The leading edge*, **25**, 156-166.
- Mora, P., 1987, Nonlinear two-dimensional elastic inversion of multioffset seismic data. *Geophysics*, **52**, 1211-1228.
- Mulder, W. A., and R. -E. Plessix, 2008, Exploring some issues in acoustic full waveform inversion. *Geophysical Prospecting*, **56**, 827-841.
- Oh, Juwon, and D.-J. Min, 2013, Weighting technique using backpropagated wavefields incited by deconvolved residuals for frequency-domain elastic full waveform inversion, *Geophysical Journal International*, **194**, 322-347.
- Pica, A., J. P. Diet, and A. Tarantola, 1990, Nonlinear inversion of seismic reflection data in a laterally invariant medium. *Geophysics*, **55**, 284-292.
- Plessix, R. -E., 2006, A review of the adjoint-state method for computing the gradient of a functional with geophysical applications. *Geophysical Journal International*, **167**, 495-503.
- Plessix, R. -E., and W. A. Mulder, 2004, Frequency-domain finite-difference amplitude-preserving migration. *Geophysical Journal International*, **157**, 975-987.
- Plessix, R. -E., and Q. Cao, 2011, A parametrization study for surface seismic full waveform inversion in an acoustic vertical transversely isotropic medium. *Geophysical Journal International*, **185**, 539-556.
- Pratt, R. G., C. Shin, and G. J. Hicks, 1998, Gauss-Newton and full Newton methods

- in frequency-space seismic waveform inversion. *Geophysical Journal International*, **133**, 341-362.
- Pratt, R. G., 1999, Seismic waveform inversion in the frequency domain, part 1: Theory and verification in a physical scale model. *Geophysics*, **64**, 888-901.
- Prieux, V., R. Brossier, S. Operto, and J. Virieux, 2013, Multiparameter full waveform inversion of multicomponent ocean-bottom-cable data from the Valhall field. Part 1: imaging compressional wave speed, density and attenuation. *Geophysical Journal International*, **194**, 1640-1664.
- Przebindowska, A., A. Kurzman, D. Köhn, and T. Bohlen, 2012, The role of density in acoustic full waveform inversion of marine reflection seismic. 74<sup>th</sup> EAGE conference & exhibition.
- Rayleigh, J. W. S., 1945, *The theory of the sound*, volume 2, Dover publication, New York.
- Reynolds, A., 1978, Boundary conditions for the numerical solution of wave propagation problems, *Geophysics*, **43**, 1099–1110.
- Romero, L.A., Ghiglia, D.C., Ober, C.C. & Morton, S.A., 2000, Phase encoding of shot records in prestack migration. *Geophysics*, **65**, 426-436.
- Routh, P.S., Krebs, J.R., Lazaratos, S., Baumstein, A., Chikichev, I., Lee, S., Downey, N., Hinkley, D. & Anderson, J. E., 2011, Full-wavefield inversion of marine streamer data with the encoded simultaneous source method. 73rd EAGE Conference & Exhibition, Extended abstracts.
- Sava, P. C. and S. Fomel, 2003, Angle-domain common-image gathers by wavefield continuation method. *Geophysics*, **68**, 1065-1074.
- Schuster, G.T., X. Wang, Y. Huang, W. Dai, and C. Boonyasirawat, 2011, Theory of multisource crosstalk reduction by phase-encoded statics, *Geophysical Journal International*, **184**, 1289-1303.
- Shin, C., K. Yoon, K. J. Marfurt, K. Park, D. Yang, H. Y. Lim, S. Chung, and S. Shin, 2001, Efficient calculation of a partial-derivative wavefield using reciprocity for seismic imaging and inversion. *Geophysics*, **66**, 1856-1863.
- Shin, C., and Min, D.-J., 2006, Waveform inversion using a logarithmic wavefield.

- Geophysics, **71**, R31-R42.
- Shin, C., and Y. H. Cha, 2008, Waveform inversion in the Laplace-domain. Geophysical Journal International, **173**, 922-931.
- Shin, C., and Y. H. Cha, 2009, Waveform inversion in the Laplace-Fourier domain. Geophysical Journal International, **177**, 1067-1079.
- Sirgue, L., and Pratt, R. G., 2004, Efficient waveform inversion and imaging: A strategy for selecting temporal frequencies. Geophysics, **69**, 231-248.
- Song, Z. M., P. R. Williamson, and R. G. Pratt, 1995, Frequency-domain acoustic-wave modeling and inversion of crosshole data: Part II-inversion method, synthetic experiments and real-data results. Geophysics, **60**, 796-809.
- Tarantola, A., 1984, Inversion of seismic reflection data in the acoustic approximation. Geophysics, **49**, 1259-1266.
- Virieux, J. and S. Operto, 2009, An overview of full-waveform inversion in exploration geophysics. Geophysics, **74**, WCC127-WCC152.
- Wu, R. and K. Aki, 1985, Elastic wave scattering by a random medium and the small-scale inhomogeneities in the lithosphere, Journal of Geophysical Research, **90**, 10261-10273.
- Zienkiewicz, O. C., and R. L. Taylor, 2000, The finite element method, volume 1: The basis. Butterworth-Heinemann.

## 초 록

# 음향파 완전 파형 역산을 이용한 다변수 추출 기법

**주요어:** 음향파, 완전파형역산, 주파수영역, 단계적 파형역산, 다변수  
**학 번:** 2011-30996

탄성과 탐사 자료처리 기술의 발전을 토대로 완전파형역산 기술 또한 지속적인 성장을 이루고 있으며, 이와 동시에 새롭고 다양한 문제에 부딪히는 국면을 맞이하고 있다. 본 연구에서는 파형역산 분야에서 최근 집중하고 있는 주제 중 하나인 다변수 추출 기법에 대하여 연구하였으며, 이의 추출을 위한 단계별 음향파 완전파형역산 전략을 제안한다. 음향파 완전파형역산을 통한 다변수 추출 기술은 최근 들어 학회 및 저널에 활발하게 발표되고 있으며 그 효용성 또한 많은 연구를 통하여 검증되어 왔다. 본 연구에서는 현재 까지 발표된 기술들에 대한 문제점을 제기하며, 보다 일반적이고 적용성이 높은 음향파 완전파형역산을 통한 다변수 추출 기술을 개발하였다.

음향파 완전파형역산에서 다룰 수 있는 여러 가지 변수 중, 본 연구에서는 속도와 밀도 추출에 집중하여 총 4가지의 매개변수화를 제안하며 각각은 속도 밀도, 체적탄성률 밀도, 임피던스 밀도, 임피던스 속도이다. 첫 번째로 각 매개변수화가 파형역산 이론 자체에서 어떤 역할을 하는지 수식을 살펴보았으며, 이로부터 각 매개변수 간의 상호간섭이 존재한다는 것을 알 수 있었다. 두 번째로 각 매개변수화의 방사 패턴을 계산하여 도시해보고 이들이 파형역산에 어떤 영향을 미치는지 알아보았다. 이를 통하여 속도와 밀도

를 단계적으로 역산해내는데 있어 각 단계에서 어떠한 매개변수화가 적합한지에 대하여 살펴보았으며, 본문에서의 분석을 기반으로 수치예제를 통하여 이론을 검증하였다. 이론 검증에 있어 계산의 효율성을 위하여 동시송신원 방법을 도입하였으며, 동시송신원 알고리즘 또한 적용하기 전 우선적으로 검증되었다. 수치예제를 통하여, 음향파 완전파형역산을 통하여 다변수를 추출하는데 있어 지배적인 매개변수를 우선적으로 추출해내는 것이 파형역산 알고리즘 자체의 안정성 및 정확성에 큰 영향을 주는 것을 알 수 있었으며, 각 단계에 대하여 적합한 매개변수화를 도입하는 것으로서 속도와 밀도 정보가 적절하게 추출된다는 것을 알 수 있었다. 실제 탐사자료에의 적용 또한 본 연구에서 개발한 알고리즘의 적용성 및 우수성을 검증할 수 있는 예제가 되었다.

결론으로, 음향파 완전파형역산을 이용한 다변수 추출은 단계적인 전략을 통하여 성공적으로 수행될 수 있으며 각 단계에서는 적절한 매개변수화가 필요함을 주장한다. 또한 본 연구를 통하여 2차적으로 발생하는 의문점 등에 대한 후속 연구를 통하여 보다 발전적이고 진취적인 연구가 가능할 것으로 예상된다.